UNIVERSIDADE DE LISBOA
FACULDADE DE CIÊNCIAS
DEPARTAMENTO DE FÍSICA

Quantifying age-related differences in Diffusion Tensor Imaging biomarkers for the male urethral sphincter of prostate cancer patients

Ana Sofia de Castro Verde

Mestrado Integrado em Engenharia Biomédica e Biofísica
Perfil em Sinais e Imagens Médicas

Dissertação orientada por:
Prof. Dr. Alexandre Andrade
Prof. Dr. Nickolas Papanikolaou

2019

“It can be difficult to face the Unknown,
but good things happen only when you do it.”

Linda Bianchini

ACKNOWLEDGEMENTS

First of all I would like to thank Champalimaud Foundation for letting me be in this institution as a master thesis student for the past year, which has been both a great personal and professional experience. It was a privilege to be in such stimulating working environment, a place where everyday a little part of the unknown is unraveled.

I would like to thank my internal supervisor, Dr. Alexandre Andrade, for always having a reassuring word of advice since day one of the course. I would like to express my appreciation to my external supervisor, Dr. Nickolas Papanikolaou, for giving me the great opportunity of being a master student at his group, the Computational Clinical Imaging Group (CCIG), and for tutoring me along the way, always giving the encouragement that I was capable of doing my best: ευχαριστώ πολύ, Nickos!

I would like to thank the director of the CCU Urology Unit, Dr. Jorge Fonseca, for presenting me a relevant clinical question and for believing that advances in Biomedical Engineering can make a difference in clinical practice. Also, I want to thank the radiologist Drª. Ana Gaivão for always sparing a little time of her clinical practice to answer my questions and to the radiology technicians and Inês Sousa, who were available when needed.

A special thanks to my dearest colleagues at CCU, who became good friends during this past year. To Eunice Carrasquinha, Francisco Oliveira and Nuno Loução, for giving me good advices and sharing their experience in research. To João Santinha, for always being available to help and to discuss ideas. To Mónica, for being my "partner in crime" at CCU with whom I've shared many thoughts and fun. To Sarita, Sílvia and Cláudia, for being such amazing girls, who were always cheering up my days. To Ju and Maria Inês, for the spontaneous hugs and laughs that filled my heart with joy. To Zé and João, for being super fun guys to be with. And to Linda, for our deep conversations during coffee, that I will cherish. With you I've learned so much and we've made fantastic memories together!

This being said, I cannot forget to thank the teachers and the classmates who accompanied me during the course. To my sweet friends Laeticia and Neusa for adding a beautiful glow in my life, to Catarina for being my dearest everyday train companion during my college years, to Bia and João for being the best group mates, to Ana Raquel for the good moments in Nancy, and to Gui, Campagnolo, Catarina, Raquel and many others for being good friends. Also, I would like to thank my sweet Anas that are always in my heart since Cardiff, and remain good friends that I consider an inspiration to follow.

Finally, I would like to thank the people who made me the person I am today. Thank you so much mum and dad for being my best friends and my support. I know I can count with you forever. Thank you to my family and to my grandparents, Manuela, Esmeralda, Eduardo e Henrique for all the love and the courage you give me to continue my journey. And last but not least, thank you Tiago, for the love and the everyday support, "we're far from the shallow now".

ABSTRACT

For the past years, radical prostatectomy (RP) has been the treatment of choice for locally advanced prostate cancer (PC) because of its high accuracy in tumor removal. However, the surgical techniques performed tend to be invasive, with a complete removal of the proximal lisso-sphincter and partial removal of the distal rhabdosphincter. Whereas the former has been related with maintenance of continence at rest, the latter is related with active continence. Between 4 to 69 % [1] of patients undergoing RP develop urinary incontinence, with a reported decrease in quality of life. This can be a consequence, not only from the surgical technique used, but from other factors including the competence of the sphincter function, that it is expected to decrease with age [2]. It is important to find preoperative imaging biomarkers that can help predict the risk of the patient developing postoperative urinary incontinence. The TransDouglas project, approved by the Ethics Committee of Champalimaud Foundation since July 2018, aims at validating the implementation of a new surgical procedure for RP, which is an improved version of the robotic-assisted laparoscopic radical prostatectomy (RALRP) procedure. Preoperative anatomical parameters are extracted from the T2-weighted magnetic resonance imaging (MRI) that can be related with urinary incontinence after the new surgical technique, and to construct a model that can help predict the likely time until urinary continence recovery.

Diffusion tensor imaging (DTI) is a MRI-based technique that allows the quantification of anisotropic movement of water molecules. It has been proven [3] that this technique can be used to visualize the microarchitecture of the urethral sphincters, and to extract relevant diffusion metrics. DTI metrics can be incorporated in the model to predict urinary incontinence recovery after RP. Considering this, an addendum to the TransDouglas project that requests the acquisition of an additional DTI sequence to the standard multiparametric (mpMRI) of the prostate has been approved this January, enabling the use of DTI to study the microarchitecture of the urethral sphincters in vivo and non-invasively. However, since parameters of sphincter function significantly change with age [2], it is important to study the influence of patient age at scan on these parameters prior to predicting the likely chance of continence recovery after RP. Therefore, the main goal of this thesis was to investigate age-related differences in DTI metrics of the male urethral sphincter complex. Furthermore, the influence of a prostate condition, including PC and benign prostatic hyperplasia (BPH), was studied.

The proximal and distal sphincters, as well as the membranous urethra, were reconstructed for 95 subjects by using the deterministic tractography algorithm in DSIStudio software [4]. DTI metrics were extracted including tract length and density, fractional anisotropy (FA), mean diffusivity (MD), axial diffusivity (AD) and radial diffusivity (RD) and additional histogram parameters for each DTI metric, namely standard deviation, median, trimmed mean, median absolute deviation, minimum, maximum, range, skewness, kurtosis, standard error and the 5^{th}, 25^{th}, 75^{th} and 95^{th} percentiles. The influence of subject motion and eddy currents corrections on the extracted DTI metrics was investigated. Linear regressions and Pearson or Spearman correlations were performed between age and each of the DTI metrics. Additionally, analysis of variance (ANOVA), or the non-parametric Kruskal-Wallis test, were used to compare DTI metrics between four age groups (from 50 to 59, 60 to 69, 70 to 79 and 80 to 89 years old). For a subset of the 69 subjects with a confirmed diagnosis for PC, BPH and the absence of any of both, ANOVA testing was used to compare between disease groups, and t-tests, or the non-parametric Wilcoxon test, to compare between cancer status. For statistically significant ANOVA test results, post-hoc t-tests were used to investigate the groups between which the difference lied.

No statistically significant differences were found on DTI metrics with and without motion and eddy currents corrections, so the non-corrected DTI data was used for the subsequent analysis. In this study, it was found that MD and RD distributions statistical significantly changed with age. In particular, older subjects evidenced lower RD kurtosis in the proximal sphincter, lower MD maximum in the distal sphincter and higher MD median absolute deviation in the membranous urethra. On the other hand, further investigations are needed to understand if the presence of a prostate condition affects the DTI metrics of the sphincters and membranous urethra.

This project was the first to examine age related differences in the urethral sphincter complex using DTI, as well as, the first time a DTI sequence for the prostate was implemented at Champalimaud Centre for the Unknown (CCU). It was concluded that age should be used as a covariate in a model that makes use of DTI biomarkers representative of the male urethral complex microstructure to predict the likely time of post-surgical continence recovery. Ultimately, this investigation should be a starting point for helping clinicians in the prediction of the risk of complications for each patient before undergoing RP, and balance the advantages and disadvantages comparing with other available treatment options for PC.

Keywords: “Diffusion tensor imaging”, “tractography”, “urethral sphincter”, “age” and “prostate cancer”.

RESUMO

Segundo dados de 2016, no sexo masculino e em países desenvolvidos, o cancro da próstata foi o cancro que registou maior incidência [5]. Após uma deteção através do aumento da evolução dos níveis do antigénio específico da próstata (PSA) no sangue e/ou de realização do teste do toque retal, o método de diagnóstico mais comum é a biópsia, que pode ser auxiliada por ultrassons ou por ressonância magnética multiparamétrica. A escolha do tratamento adequado para cada paciente depende do estadio da doença e das suas preferências individuais, que geralmente pretendem equiponderar a esperança de vida para o paciente e a qualidade de vida após tratamento. Geralmente, as opções de tratamento mais adequadas para um paciente com PSA > 10 ng/mL e nódulos palpáveis são: acompanhamento e tratamento dos sintomas à medida que estes surgem, radioterapia ou braquiterapia, e cirurgia [6]. A última opção, em particular a prostatectomia radical, tem demonstrado maior precisão na remoção de tecido maligno e no aumento da esperança média de vida para os pacientes operados [7]. Mais recentemente, técnicas laparoscópicas convencionais têm vindo a ser substituídas por técnicas robóticas que oferecem maiores vantagens no pós-operatório. No entanto, a incontinência urinária e a disfunção erétil continuam a ser complicações reportadas por uma percentagem significativa de pacientes submetidos a cirurgia. Relativamente ao primeiro, afeta cerca de 4 a 69 % dos pacientes [1], e a sua ocorrência está intimamente ligada à remoção do esfíncter proximal ou liso, que ocorre aquando da remoção da próstata, e consequente dano no esfíncter distal ou rabdoesfíncter.

A construção de um modelo preditivo da recuperação da continência pós-cirúrgica com base na utilização de biomarcadores do esfíncter, pode permitir aos prospetivos pacientes uma escolha ponderada do tipo de tratamento. No entanto, é sabido que a microestrutura do esfíncter varia com a idade [2], logo é necessário conhecer o padrão de variação dos biomarcadores do esfíncter com a idade, no sentido de avaliar a recuperação pós-cirúrgica da continência.

Para estudar a microestrutura do esfíncter têm sido utilizadas diversas técnicas *in vivo* [8]–[13] que, no entanto, não fornecem informação tridimensional da estrutura e orientação das fibras que o compõem. Contrariamente, imagem por tensor de difusão (DTI) é uma técnica não invasiva baseada em ressonância magnética que permite quantificar o movimento das moléculas de água nos tecidos, através da aplicação de gradientes em várias direções não colineares [14]. Relacionando o gradiente aplicado com o sinal medido, obtém-se em cada voxel informação sobre a magnitude e direção da difusão. A partir da diagonalização do tensor de difusão é possível calcular *eigenvalues* e *eigenvectors*. Enquanto que os últimos refletem a direccionalidade, os primeiros quantificam a magnitude da difusão e combinados entre si permitem obter um conjunto de métricas – que inclui a anisotropia fracional (FA), difusibilidade axial (AD), difusibilidade média (MD) e difusibilidade radial (RD) – que permitem estudar a organização estrutural das fibras. Apesar das aplicações de DTI se focarem essencialmente em estudos de conectividade da substância branca do cérebro, têm progressivamente sido alargadas ao estudo de outros órgãos, como o rim [15], o coração [16] e a próstata. Relativamente ao uso de DTI para o estudo da próstata, esta técnica tem sido utilizada para estudar este órgão em condições normais [17] e para definir métricas que permitam distinguir tecido saudável de tumoral [18]. Ademais, estudos têm avaliado os feixes neuro-vasculares da próstata antes e após a cirurgia e correlacionado com a disfunção erétil pós-prostatectomia radical [7]. Para além de um estudo que investigou o esfíncter uretral feminino usando DTI [19], que se tenha conhecimento, existe apenas um estudo que conseguiu utilizar DTI para estudo da microarquitectura do esfíncter masculino em sujeitos jovens e sem patologia [3].

Assim, o principal objetivo da presente tese de mestrado é investigar variações derivadas da idade no complexo do esfíncter uretral, que compreende os esfíncteres proximais e distais e a uretra membranosa – correspondente ao segmento da uretra que se estende desde o ápice da próstata até ao bulbo peniano. No sentido de estudar o efeito da presença de uma condição da próstata, incluindo cancro da próstata e hiperplasia benigna da próstata (HBP), a variação das métricas de DTI do esfíncter para o grupo de pacientes diagnosticados foi também avaliada. Como objetivo secundário, que teve importância na etapa de processamento dos dados de DTI, foi investigado se a correção de movimento durante a aquisição e correção de correntes de Foucault afetava significativamente as métricas de DTI em estudo, para cada uma das estruturas.

Para tal, os esfíncteres proximal e distal, bem como a uretra membranosa, foram reconstruídos para 95 indivíduos usando o algoritmo determinístico de tractografia no software DSIStudio [4]. Previamente foram definidas manualmente um conjunto de regiões de interesse nos mapas coloridos de FA para os esfíncteres proximal e distal, e na imagem anatómica em T2 para a uretra membranosa. Para a tractografia, foram otimizados alguns parâmetros segundo uma abordagem de tentativa e erro, que acabou por estabelecer um valor limite de anisotropia fracional de 0.15, e um limite angular de 75º e 45º, respetivamente para os esfíncteres e para a uretra. As métricas de DTI foram extraídas para cada uma das estruturas reconstruídas, incluindo o comprimento e densidade das fibras, FA, AD, MD e RD e parâmetros adicionais do histograma para cada métrica de DTI, ou seja, desvio padrão, mediana, média aparada, desvio absoluto mediano, mínimo, máximo, amplitude, assimetria, curtose, erro padrão e os percentis 5, 25, 75 e 95. A influência do movimento e da presença de correntes de Foucault nas métricas de DTI extraídas foram investigadas. Regressões lineares e correlações de Pearson ou Spearman foram realizadas entre a idade e cada uma das métricas de DTI. Além disso, uma análise de variância (ANOVA) – ou o equivalente teste não paramétrico de Kruskal-Wallis –, foram realizados para comparar métricas de DTI entre quatro faixas etárias (de 50 a 59, 60 a 69, 70 a 79 e 80 a 89 anos). Para um subconjunto dos 69 indivíduos com diagnóstico confirmado de cancro de próstata, HBP ou da ausência de qualquer um dos dois, o teste ANOVA foi usado para comparar entre grupos de doença. Adicionalmente, testes *t-student* – ou o teste não paramétrico de Wilcoxon – foram utilizados para comparar a presença vs. ausência de cancro. Para resultados estatisticamente significativos do teste ANOVA, foram posteriormente empregues testes *t-student* para investigar entre que grupos se encontrava a diferença.

Não foram encontradas diferenças estatisticamente significativas nas métricas de DTI com e sem correção de movimento e correntes de Foucault, logo, os dados de DTI sem correção foram utilizados para a análise subsequente. Neste estudo, verificou-se que as distribuições de MD e RD variaram significativamente com a idade. Em particular, indivíduos mais velhos evidenciaram menor curtose da RD no esfíncter proximal, menor valor máximo de MD no esfíncter distal e maior desvio absoluto mediano de MD na uretra membranosa. Por outro lado, são necessárias investigações adicionais para entender se a presença de uma condição da próstata pode afetar as métricas de DTI dos esfíncteres e da uretra membranosa. Tal acontece, pois os resultados obtidos neste estudo para a presença de doença estão limitados pela heterogeneidade da amostra em termos das diferentes condições que cada indivíduo pode apresentar.

Julga-se que este estudo foi o primeiro a identificar variações com a idade nas métricas de DTI do esfíncter. Além disso, definiu a inclusão de uma sequência de DTI à ressonância magnética multiparamétrica da prática clínica da Fundação Champalimaud. Por se tratar de um estudo prospetivo, foi possível definir os parâmetros de aquisição – nomeadamente o valor de b (em s/mm^2), o número de direções da aplicação do gradiente, o número de cortes adquiridos e a extensão da aquisição - ótimos

para a visualização das estruturas do complexo uretral masculino, com o melhor compromisso entre duração da aquisição (em minutos) e a resolução espacial (em milímetros). Esta nova sequência só começou a ser incluída na clínica desde Janeiro 2019, o que representa cerca de 14 pacientes operados, dos 45 diagnosticados com cancro da próstata. Assim que for possível aumentar a amostra de pacientes operados com um intervalo de tempo pós-cirúrgico de 3 a 6 meses, será possível utilizar os resultados dos testes de incontinência, os dados de DTI do esfíncter corrigidos da idade e as medidas do comprimento da uretra em T2, para prever o tempo de recuperação de continência pós-cirúrgica. No futuro, esperamos poder extrair os biomarcadores de DTI para o complexo do esfíncter uretral de cada paciente e usá-los como um preditor da taxa de incontinência pós-cirúrgica. No entanto, é importante que este modelo tenha em conta alterações nas métricas de DTI do complexo uretral masculino que são influenciadas pelo envelhecimento. Esse modelo preditivo pode orientar os pacientes na escolha informada da melhor opção de tratamento personalizado para tratar o tumor da próstata e, simultaneamente, proporcionar uma qualidade de vida satisfatória.

Palavras-chave: “Imagem por tensor de difusão”, “tractografia”, “esfíncter uretral”, “idade” e “cancro da próstata”.

CONTENTS

LIST OF FIGURES

LIST OF TABLES

LIST OF ACRONYMS

AD	Axial diffusivity
ADC	Apparent diffusion coefficient
AFS	Anterior fibromuscular stroma
BPH	Benign prostatic hyperplasia
CG	Central gland
DCE	Dynamic contrast enhanced
DRE	Digital rectal exam
DTI	Diffusion tensor imaging
DWI	Diffusion weighted imaging
FA	Fractional anisotropy
FACT	Fiber assignment by continuous tracking
FOV	Field of view
HC	Healthy controls
ICIQ-SF	Incontinence questionnaire-short form
LUTS	Lower urinary tract symptoms
MD	Mean diffusivity
mpMRI	Multiparametric MRI
PC	Prostate cancer
PI-RADS	Prostate Imaging Reporting and Data System
PE	Phase-encoding
MRI	Magnetic resonance imaging
PNFs	Periprostatic neurovascular fibers
PSA	Prostate specific antigen
PZ	Peripheral zone
RALRP	Robotic assisted laparoscopic radical prostatectomy
RD	Radial diffusivity
ROI	Regions of interest
RP	Radical prostatectomy
SENSE	Sensitivity encoding
SP-EPI	Spin-echo planar imaging
SNR	Signal-to-noise ratio
TZ	Transition zone

1 INTRODUCTION

Urinary incontinence is a post-surgical complication that diminishes prostate cancer (PC) patients quality of life. The main focus should be, not on the treatment of urinary incontinence, but rather on its prediction before occurrence. Individual preoperative imaging parameters of the male urethral sphincter complex microstructure can potentially be used to predict the rate of post-surgical continence recovery. However, since its microstructure is thought to change with age, it is important to access age-related differences in the male urethral sphincter complex.

1.1 Objectives and hypothesis

To our knowledge, there is one published study that has successfully shown that diffusion tensor imaging (DTI) can be used to study the male urethral sphincter complex [3]. After feasibility of urethral sphincters' DTI has been proven for eleven healthy young subjects, we aim at addressing a gap in the literature with the investigation of age and disease related changes on DTI metrics of older male subjects with (suspected) PC, benign prostatic hyperplasia or without any prostate condition. Additionally, there is no stablished consensus on whether motion and eddy currents corrections should be performed on DTI of the male urethral complex and which is the recommended method, due to the limiting number of existing studies.

Hereupon, this thesis has the following objectives:

1) Studying the influence of motion and eddy currents correction on the analysis of DTI metrics of the male urethral sphincter complex;
2) Investigating whether DTI metrics significantly change in the presence of a prostate condition, namely PC and benign prostatic hyperplasia (BPH);
3) Investigating age-related differences in the male urethral sphincter microarchitecture, studying whether there is a linear relationship or correlation between age and DTI metrics of the sphincter complex, and by comparing DTI metrics by age decades – which is the current thesis main goal.

Regarding 3), since it is expected a decrease in fiber integrity with age, it is hypothesized a reduction in fractional anisotropy (FA) with increasing age. Also, it is hypothesized a reduced tract density and length in older subjects, reported by tractography findings. These findings may help understanding the effect of ageing in the male urethral sphincter microstructure, in order to be able to weight in the influence of age when predicting the rate of recovery from postoperative urinary incontinence.

The current master thesis has been structured to first cover the relevant theory on the anatomy of the prostate and adjacent structures of the male pelvic complex, prostate conditions focusing on PC, postoperative complications following radical prostatectomy (RP) centering on urinary incontinence, and several aspects related with diffusion tensor imaging (DTI) as a non-invasive technique to study the sphincters' microarchitecture. In chapter 3, the current state-of-the-art for DTI is addressed, from brain applications, passing through studies of DTI on pelvic organs, to applications on the prostate, periprostatic neurovascular fibers (PNFs) and the urethral sphincter complex. Afterward, in chapter 4, the materials and methods used for data acquisition, imaging processing, tractography and statistical analysis are presented. In the following chapter, the results are presented for addressing each one of the study goals, related with the effect of motion and eddy currents corrections, as well as the fiber tracking results analyzed both with age and disease. Lastly, the discussion and study conclusions, limitations, and future work are presented in chapter 6.

2 BACKGROUND

2.1 Normal prostate and its conditions

2.1.1 Prostate anatomy

The **prostate** is an accessory gland of the size and shape of a walnut, with about 4 cm long and 2 cm wide, that is part of the male reproductive system [20]. During ejaculation, this gland contracts to accomplish its main function of secreting a fluid to nourish and protect sperm, contributing to 30% of the semen. This gland is located inferior to the urinary bladder, superior to the penile bulb and anterior to the rectum. If one is to divide the prostate into three thirds in the superior-inferior direction, it is possible to consider, respectively, the base (right below the bladder), the midgland and the apex [21].

An extra prostatic capsule incompletely encircling the prostate, made of smooth muscle on the internal portion and fibrous connective tissue on the external portion, can be acknowledged. However, histological evaluation confirms the nonexistence of a real prostate capsule (in return one can designate it as a pseudo capsule), since this tissue is inseparable from prostatic stroma.

This gland is crossed by the prostatic segment of the urethra, that can be used as a central anatomical reference point to locate each one of the prostate regions [22]. Considering the zonal anatomy of the prostate, it is possible to divide it into four histologically and anatomically distinct zones: peripheral zone (PZ), transition zone (TZ), central zone (CZ) and anterior fibromuscular stroma (AFS). The peripheral zone constitutes 70% of glandular tissue and it is located on the posterior and lateral side of the prostate, radiating laterally to the urethra. The transition zone is crossed by the prostatic urethra and constitutes only 5% of the prostate glandular tissue. Posteriorly to the transition zone, is the central zone that follows left and right ejaculatory ducts, branching laterally into the prostate base. This region constitutes 25% of the glandular tissue. Finally, the non-glandular anterior fibromuscular stroma is the smaller area that occupies the totality of the anterior surface of the prostate. The prostate zonal anatomy can be depicted in Figure 2.1, that also shows how each third of the prostate can be subdivided into 6 sectors on each side.

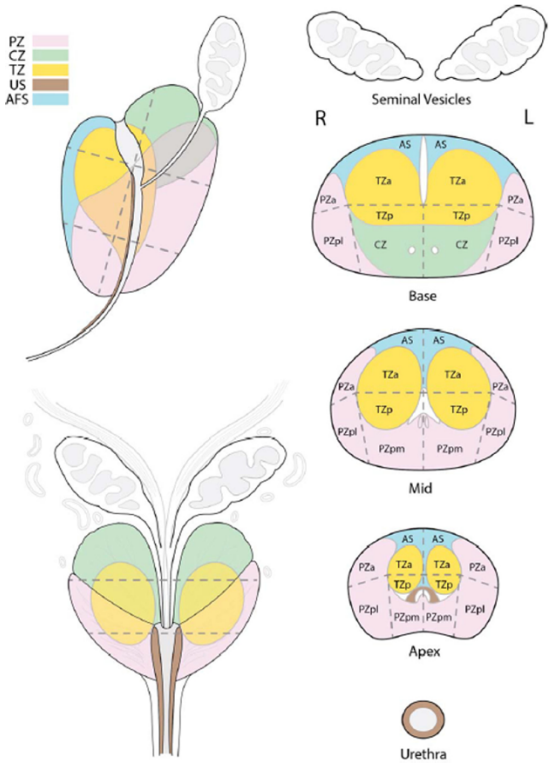

Figure 2.1 Zonal anatomy of the prostate gland, showing the peripheral zone (PZ) in pink, the central zone (CZ) in green, the transition zone (TZ) in yellow, the urethral sphincter (US) in brown and the anterior fibromuscular stroma (AFS) in blue. On the right side of the image, it is possible to see the seminal vesicles, the urethra and the subdivision of the prostate base, midgland and apex into 12 sectors described on Table 2.1. – adapted from [23].

Table 2.1 Acronyms for the 6 sectors repeated on both sides of base, midgland and apex.

Base	
AS	Anterior fibromuscular stroma
TZa; TZp	Anterior (a) and posterior (p) transition zone
PZa; PZpl	Anterior (a) and posterolateral (pl) peripheral zone
CZ	Central zone around the ejaculatory ducts
Midportion	
AS	Anterior fibromuscular stroma
TZa; TZp	Anterior (a) and posterior (p) transition zone
PZa; PZpm; PZpl	Anterior (a), posteromedial (pm) and posterolateral (pl) peripheral zone
Apex	
AS	Anterior fibromuscular stroma
TZa; TZp	Anterior (a) and posterior (p) transition zone
PZa; PZpm; PZpl	Anterior (a), posteromedial (pm) and posterolateral (pl) peripheral zone

2.1.2 Anatomy of other relevant structures of the male pelvic complex

The **seminal vesicles** are two sac-shaped glands, divided into left and right, with about 5 cm long. Each gland has a capsule of both fibrous connective tissue and smooth muscle. The seminal vesicles contribute with about 60% of fluids to the semen [20].

The **male urethral sphincter** is composed by a continuous muscle around the urethra with variable thickness in cranial to caudal extension [24]. However, it forms a functional subdivision into two muscles, the lisso-sphincter and the rhabdosphincter (Figures 2.2 and 2.3). Whereas the lisso-sphincter (also known as proximal sphincter) is composed of smooth muscle and forms a complete ring around the urethra, the rhabdosphincter (also known as distal sphincter) is composed of skeletal muscle and has a shape of a horseshoe, being thickest around the membranous urethra and less distinct near the bladder (in opposition to the proximal sphincter). The rhabdosphincter configuration may vary from an extended circular shape with over half circumferential orientation with limited proximal-distal length and thickness, to a restricted circular pattern such as a thin arc-like structure [25]. The primary function of the lisso-sphincter is maintaining continence at rest, whereas the rhabdosphincter has a dual genitourinary function, both related with erection and active continence - related with the forceful closure of the urethra in stress conditions [24].

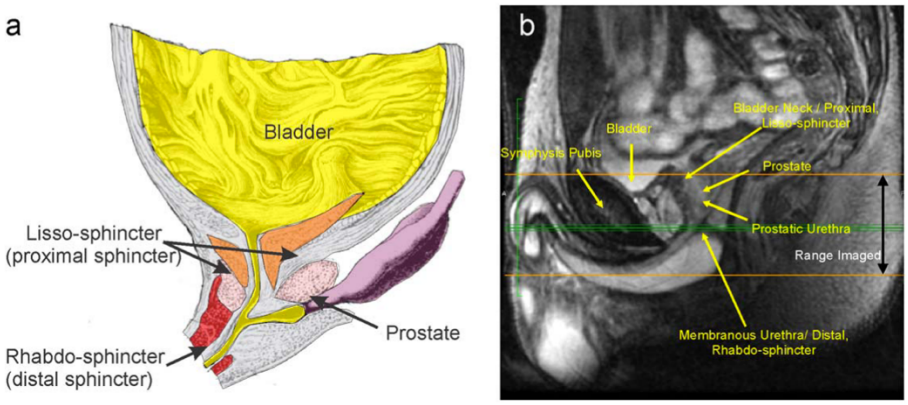

Figure 2.2 Mid-sagittal male anatomy near the bladder and urethra, including a schematic on that section (a) and a magnetic resonance imaging (MRI) high-resolution proton density image on an increased field of view (FOV) (b) - adapted from [3].

Figure 2.3 Schematic neuroanatomy of the male urethral sphincter complex, including the bladder musculature (1), the perineal membrane (6), the prostate (7), and with particular attention to the following: the proximal (2) and distal (3) parts of the lisso-sphincter, the rhabdosphincter (4) and the prostatic part of rhabdosphincter (5) - adapted from [24].

The **levator ani fascia** is composed of smooth muscle tissue, mostly with bulky and multilayered fibers [25]. In most men, it can be observed that the levator muscle is connected by a connective tissue mass with the urethral sphincter, the distal half portion of the prostate and the membranous urethra. Posteriorly to the membranous urethra, this muscle is also connected with the outer layer of the rectum (Figure 2.4).

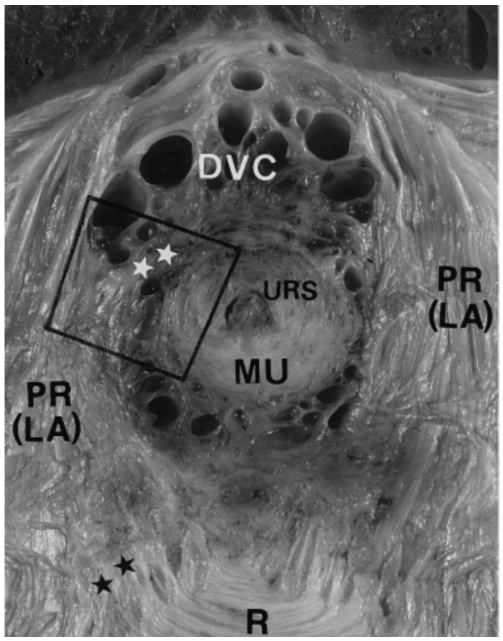

Figure 2.4 Gross slice of the pelvis showing the levator ani (LA) fascia and the urethral rhabdosphincter (URS). The URS and the puborectalis muscle (PR) are connected by a thick tissue mass (marked with white stars). The PR is also connected to the outer layer of the rectum (marked with black stars) In this figure it is also possible to observe the dorsal vein complex (DVC) and the MU (membranous urethra) – adapted from [25].

The **neurovascular bundles** comprise the association of nerves that supply the corpora cavernosa with arterial branches that come from the inferior vesicle artery and with veins [21]. This bundle appears bilaterally to the prostate and its function is intimately related with sexual function.

2.1.3 Prostate conditions

Most men during their lifetime, end up having some condition that affects the prostate. These can be benign, like prostatitis or BPH, or malignant, considering PC. The former is characterized as an inflammation of the prostate that can be caused by bacterial agents, and it is more easily treated through antibiotic administration. The other benign prostate condition, BPH, is mostly related with ageing, affecting more than 50 % of men over 60 years old and about 90% when they reach their eighties [26]. Not only ageing, but also infections and tumors can be a cause for this condition [20]. BPH is characterized by an enlargement of the prostate volume, where the majority of its growth occurs in the TZ. Looking from a molecular perspective, it was found that the prostate enlargement is related with higher concentrations of serum insulin-like growth factor 1.

Normally, BPH is diagnosed through patient history, physical and rectal examinations, investigations to exclude urinary tract infection and renal damage, and urinary flow measurement. Regarding treatment, active surveillance in combination with urodynamic pressure/flow studies are recommended priory to

any kind of invasive treatment that involves the removal of obstructing tissue, such as laser therapy or transurethral resection of the prostate. This procedure takes about 20-30 minutes, considering a gland of 30 g, and has a small mortality rate of around 0.2-0.4 % [26].

Apart from detrusor muscle and bladder overactivity, age-related smooth muscle dysfunction, and neurological factors, prostatitis and BPH are some of the main causes for lower urinary tract symptoms (LUTS) in men. LUTS are not defined as a disease, but rather as a symptom-complex that affects ageing women and men. Main symptoms, that are frequently accepted by the elderly as normal but significantly impact their quality of life, can be categorized into voiding symptoms - including hesitancy in urinating, poor urinary flow, sensation of incomplete bladder emptying, late urine dribbling and prolonged urination - and into storage symptoms - comprising frequent daytime voiding, nocturia, urgency in voiding and involuntary incontinence of urgency.

2.1.4 Prostate cancer

Epidemiology, Detection, Diagnosis and Staging

Prostate cancer is a clinically heterogeneous disease and the most diagnosed cancer in men in the world (Figure 2.5), with approximately 1.4 million incident cases and 381,000 deaths in 2016 [5]. The incidence of PC has been increasing by 40% since 2006, due to a change in the age structure and size of the population, and due to an alteration in the age-specific incident rates. Prostate cancer represents the fifth most common cause of cancer death worldwide, with higher incidence in developed countries [27]. Particularly, while the odds of developing PC are of 1 in 16 for low-middle sociodemographic index countries, these are of 1 in 7 for countries with a high index [5].

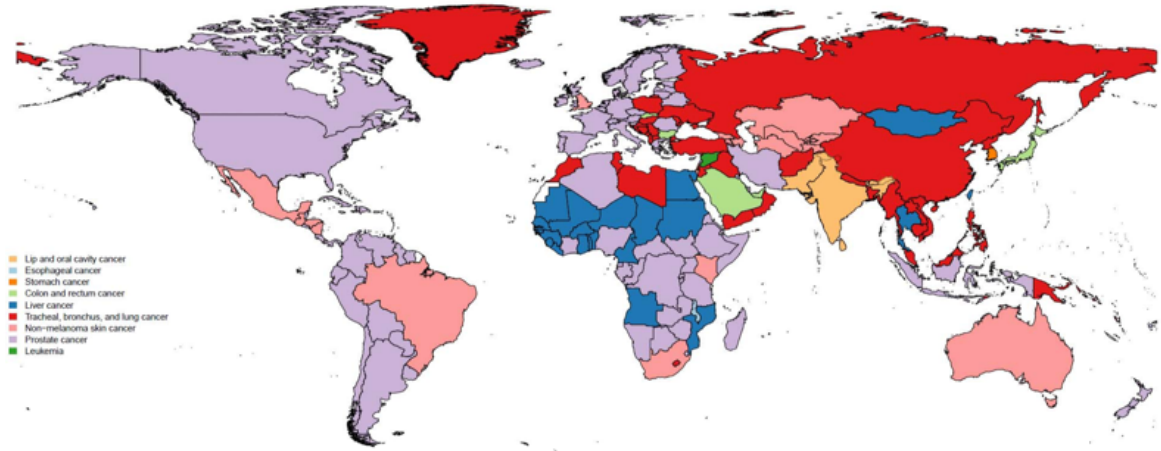

Figure 2.5 Absolute incident cases (in 2016) for male subjects, color encoded by cancer type. As we can see, PC (shown in purple) is the most incident cancer in men worldwide, and the one with a higher incidence in men in Portugal – adapted from [5].

Two risk factors clearly associated with PC are age, with 36.3 % of cancers being diagnosed between 60 to 69 years old [28], and heredity, being PC a polygenic disease. Apart from these, other risk factors may play a role in this condition [29], including race (African individuals are more prone on developing PC), inflammation (having some chronical inflammatory process that may affect the prostate), hormones (specifically, patients that undergo hormonotherapy for suppression of male sexual hormones after puberty have a higher risk of developing PC), metabolic syndrome, diets based on certain vitamins and antioxidants that may serve as a protection on the development of cancer, smoking (cadmium in

circulatory system may increase the change of cellular oxidation) and physical activity (that increases overall quality of life, helping to minimize the risk of PC). Although the prevention is key in decreasing the incidence of some cancers, like lung cancer (through the control of tobacco exposure) and skin cancer (through the reduction of exposure to ultra-violet radiation), in PC the prevention efforts can be less effective. Additionally, the early signs and symptoms of PC are very rare. So, prevention should be done in conjunction with the utilization of early detection methods and better access to treatment.

Detection of PC can be assessed by an increase in the prostate specific antigen (PSA) levels in the blood or by textural or consistency changes on the prostate's posterior aspect of the PZ detected by the digital rectal exam (DRE). Although a PSA threshold of higher than 4.0 ng/mL is commonly used as an indicator for performing a PC diagnosis, PSA values can change with different factors, and there is no such thing as a normal/abnormal PSA test result [30]. For each case, patient characteristics should be incorporated in the evaluation of PSA test results, and the evolution of PSA levels over time should be monitored.

The gold standard for diagnosis remains the biopsy, which consists on the analysis of prostate tissue samples from 10 to 12 different locations in a grid-like pattern, collected via transrectal ultrasound [6]. Then, the pathologist assigns a score, the Gleason grade, that reflects tumor aggressiveness by the sum of a primary score on the largest area of the tumor plus a score on the second largest area, each ranging from 1 (closer to healthy tissue) to 5 (closer to abnormal tissue). For instance, a Gleason score of 3 + 4 (grade 2) is different from a Gleason score of 4 + 3 (grade 3). However, even the ultrasound-guided biopsy has the limitations of undetecting 21-28% of prostate tumors, as well as, of assigning a lower Gleason grade to 14-17% of cases. Combination of biopsies with other techniques, such as, new molecular biomarkers, measurement of PSA levels and multiparametric MRI (mpMRI) – including high resolution T1 and T2 weighted imaging, diffusion weighted imaging (DWI) and dynamic contrast enhanced (DCE) imaging – for a targeted biopsy, can help identify false negative cases. A targeted biopsy, meaning MRI fused with ultrasound, increases the correct stratification of patients, compared with a systematic prostate biopsy. Prostate metastases and PC recurrence – defined as a PSA > 0.2 ng/mL after surgery – are usually diagnosed by cross-sectional body imaging with computed tomography, MRI or positron emission tomography with recently FDA approved radiotracers that have demonstrated activity on PC.

Based on the mpMRI acquisition, a more standardized classification system was introduced in 2012, called the Prostate Imaging Reporting and Data System (PI-RADS) [21]. This classification system provides a score from 1 (very low) to 5 (very high) to each prostate lesion, according to the likelihood of a clinically significant PC. Depending on the prostate region, the PI-RADS category is assigned based on the characteristics of the lesion in a specific MRI sequence (as observed in Figure 2.6), namely, for lesions in the PZ the primary sequence used are the diffusion weighted imaging (DWI) or the apparent diffusion coefficient (ADC), while for the TZ is the T2-weighted imaging. Most prostate tumors (75 to 85%) originate in the PZ [31], that appears as a thin layer of high signal intensity in the T2-weigthed imaging. It is less common (less than 25%) for cancer to be originated in the TZ – an heterogenous region of intermediate signal intensities –, and even less on the CZ or AFS (although tumors originated elsewhere can spread to these regions). The pseudo capsule, that appears as a hypointense line on the T2-weighted imaging, is considered to be useful as a reference to assess the extra prostatic extension of the tumor.

Regarding the interpretation of prostate tumors on the mpMRI, these appear to be hypointense (dark) on the T2-weighted imaging and on the ADC map, and hyperintense (bright) on the DWI. In fact,

malignant cells create a restriction to diffusion (low ADC), translating in a high DWI signal, that is evidenced when using a higher b-value (at least 1400 s/mm^2) that improves lesion conspicuity [21].

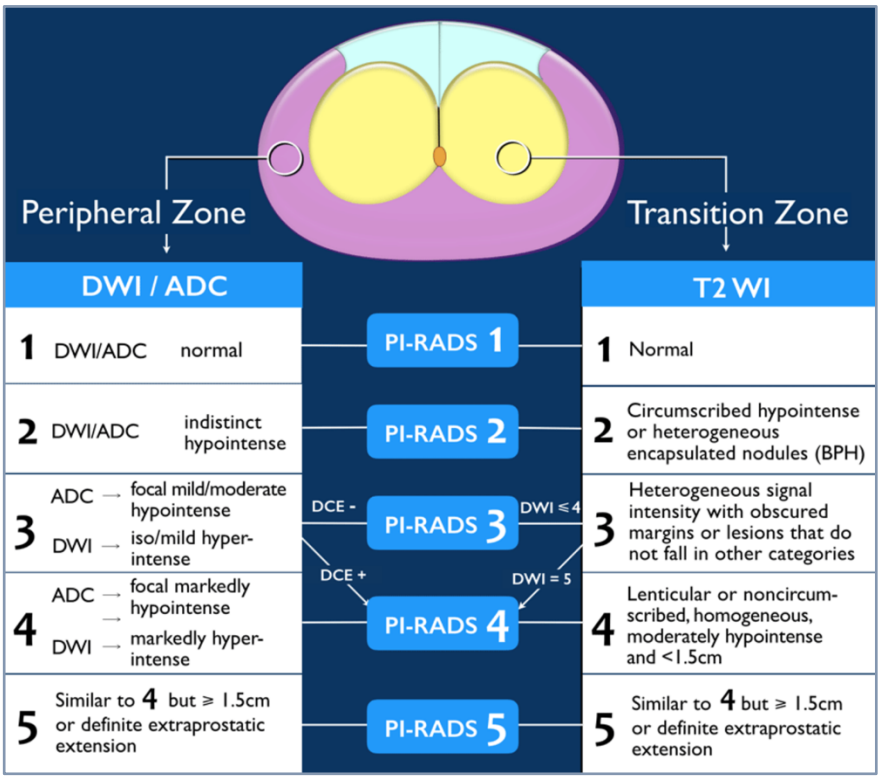

Figure 2.6 PI-RADS assessment categories for lesions on each prostate region, PZ and TZ, based on the DWI/ADC and the T2-weighted image, respectively. To distinguish between similar lesions, other mpMRI sequences can be used as reference, such as the DCE image – adapted from [32].

Recent advances on diagnosis techniques, have allowed a better stratification of PC patients by risk, which is key to make a balanced choice on disease treatment [6]. Prostate tumors can be stratified by risk into very low, low, intermediate, high or very high, as proposed by the National Comprehensive Cancer Network. This risk stratification is done by a combination of the biopsy Gleason score, the PSA and the TNM (Tumor, Node, Metastasis) clinical staging – the latter is based on clinical and pathological findings and it is mainly divided into T1 (inapparent tumor), T2 (tumor confined to the prostate), T3 (tumor extends through the prostate capsule), T4 (tumor invades other nearby structures), N0 (absence of regional lymph node metastasis), N1 (metastasis in regional lymph nodes), M0 (no distant metastasis) and M1 (distant metastasis). An accurate biopsy is of crucial importance for a correct risk stratification. Based on the risk stratification assigned to each patient, plus his individual preferences and values, clinicians can guide patients on the decision-making process regarding treatment type.

Treatment of Prostate Cancer

It is normally recommended that patients with a less aggressive prostate tumor, defined as a PSA < 10 ng/mL or a Gleason score of 3 + 3, choose to be in active surveillance for PC [6]. This consists of a combination of techniques to regularly monitor the disease evolution, including PSA testing, physical examinations and prostate biopsies.

On the opposite side, patients with metastatic PC (including regional lymph node or distant metastases) are usually recommended an initial treatment of chemotherapy (using drugs like abiraterone, enzalutamide or others), that is commonly preferred over traditional hormonal therapy, like androgen deprivation therapy.

On the intermediate side, patients with localized PC, with a PSA > 10 ng/mL and nodules palpable on DRE, mostly rely on expectant management, radiation and surgery as the available treatment options. Expectant management comprises both active surveillance and watchful waiting, that consists on treating disease symptoms with a palliative intent. Regarding curative approaches, radiation treatment can be done both by external radiotherapy or brachytherapy (through the implantation of radioactive seeds on the prostate), or through a procedure called RP. The latter has been considered the main choice for locally advanced PC, because of the accuracy in tumor excision [7].

Additionally, curative approaches generally offer a higher life expectancy, which is considered a predominant decision-making factor to patients [33]. Although in the past, RP was not recommended for older patients (>70 years old), this trend has been changing, mainly due to higher survival rates and better functional outcomes, related with increased life expectancy and advances in surgical techniques [34].

Postoperative complications following Radical Prostatectomy

Despite significant improvements in the last years, severe post-surgical complications may still arise from RP, namely urinary incontinence and erectile dysfunction [35], that can significantly reduce the patient's quality of life. While urinary incontinence is mostly related with the removal of the proximal lisso-urethral sphincter (even in the presence of an intact distal rhabdosphincter) [3], the recovery of erectile dysfunction after RP is mostly associated with the degree of PNFs sparing [36] - since periprostatic autonomic nerves are crucial for erectile function. Despite that, the mechanisms of post-surgical urinary incontinence are still to be stablished, since they are known to be a result of the combined integrity between the proximal and distal sphincters and of surrounding prostate structures, including muscles and fasciae [37]. Urinary incontinence has been reported in 4 to 69 % of patients that undergo RP [1]. This wide range of reported incidence may be due to the evaluation tool used, the length of the follow-up chosen, and mainly, to the definition used to classify incontinence [38]. There are different forms of quantifying the patient's continence, but traditionally, a definition of using zero pads per day is better correlated with the quality of life after RP [39]. This can be accessed among patients using the international consultation on incontinence questionnaire-short form (ICIQ-SF) score [40], that is presented to the patient at several time points after RP to evaluate the severity of urine leakage and impact on quality of life. Incontinence after RP is likely to emerge from multifactorial causes, including patient characteristics, preoperative continence status, urethral characteristics, detrusor function, and those related with the surgical technique [1]. Particularly, higher surgeon experience has been shown to reduce the rate of postoperative complications [35]. Regarding patient characteristics, the patient age at surgery has been considered a stablished predictor for urinary incontinence recovery. Although some studies have not found a statistically significant trend between post-surgical continence recovery rate and ageing [37], most studies have correlated increasing patient age at surgery with higher risk of urinary incontinence. It was found that while 3% of patients aged below 60 show complete incontinence after surgery, this percentage is more that 20% in patients older than 70 years old [2]. A recent study [34] has found that younger patients (age <= 70 years old) have a higher urinary continence recovery rate after 3 and 12 months, comparing with older patients (age > 70 years old), although the rate gap between age groups has decreased during the study period (2004 to 2015). This same study aimed at defining the

predictor factors of post-surgical urinary incontinence following RP for the two different age groups. They have found that, while different predictors can be used for younger patients, namely, age, robot-assisted RP, prostate volume, membranous urethral length (MUL) and neurovascular bundles' sparing, only the age and MUL were found to be predictors for continence recovery in older male.

Regarding urethral characteristics, they are the result of sphincter incompetence, changes in urethral length or preoperative strictures [41]. In fact, the proximal sphincter is completely removed during RP, which can explain the high risk of postoperative urinary incontinence. So, post-operative continence mostly relies on the rhabdosphincter [41].

Currently, the available treatment options for post-operative incontinence comprise conservative approaches - pelvic floor exercises or biofeedback -, pharmacotherapy, transurethral bulking agents or artificial urinary sphincter and male slings [1]. However, the goal of the urologic surgeon should be, not on the treatment of postoperative incontinence, but rather on the reduction of its rate, before occurrence [41]. Some studies [42] argue that the solution to reduce the complication should focus on the alteration of the technical aspects of the surgical procedure. For instance, this study [43] has introduced a method for reconstructing the rhabdosphincter during the RP performed with the robotic system. Traditional laparoscopic procedures have been replaced by RALRP, a robotic surgical system offering 7 degrees of freedom, tridimensional magnification and scaling of movements [39]. This technique has been gaining an increased acceptance for the treatment of localized PC - with less blood losses and transfusion rates, better perioperative outcomes and possible faster recovery of urinary continence and erectile function [39].

The TransDouglas project aims at validating the efficacy of a new surgical procedure for RP, which is the improved version of RALRP. This technique, called Retzius-sparing robotic assisted laparoscopic RP, proposed by Galfano [44], spares the retropubic space by passing through the Douglas pouch. By doing that, it is expected a faster postoperative recovery of urinary continence, since most anatomical structures involved in continence remain intact [45]. Particularly, the reduced damage of the PNFs and the preservation of the distal rhabdosphincter can lead to better post-operative outcomes regarding, respectively, erectile function and urinary incontinence.

2.2 Diffusion tensor imaging

Previously, a study [3] has shown the feasibility of visualizing muscle fibers of the prostate sphincters using diffusion tensor imaging (DTI), a useful technique to understand tissue microarchitecture, in terms of fibers integrity and directionality. In this section, a theoretical introduction to DTI is presented, followed by a brief introduction to tractography methods, a popular method used for fiber reconstruction and 3D visualization of fibers, and to different steps of the DTI processing and analysis workflow, including motion and eddy currents correction methods.

2.2.1 Theoretical background

Brownian motion

The terms "Brownian motion" or diffusion can be used to describe the random thermal movement of molecules [46]. Einstein has described mathematically this physical property at a given temperature by Equation 2.1.

$$\langle r^2 \rangle = 6\,D\,t \qquad (2.1)$$

where the first term represents the mean squared displacement of the molecules, D is the diffusion coefficient, a constant that relates diffusive flux to a concentration gradient, and t the diffusion time. The diffusion coefficient (D), accounting for several factors that influence diffusion in living systems, can be referred to as the ADC [47]. The ADC for water molecules at a body temperature of 37° C is $3 \times 10^{-3}\ \mathrm{mm^2/s}$ [48]. Considering a diffusion time in the order of milliseconds according to the typical MR measurement time (10–100 ms) [49], water molecules will travel a distance in the order of micrometers. This displacement is in the same order of magnitude as the cellular dimensions, which makes it possible to access the microstructural properties of biological tissues.

Diffusion weighted imaging

Diffusion weighted imaging (DWI) is sensitive to the Brownian motion of water molecules in biological tissues, and so, it can be used to explore tissues' microarchitecture [50]. The diffusion-weighted pulse sequence corresponds of two gradients, equal in magnitude, that are applied to the T2-weighed spin-echo sequence (Figure 2.7). These gradients are applied before and after the 180° refocusing radiofrequency pulse, symmetrically centered at it, which is known as the Stejskal-Tanner diffusion encoding [51].

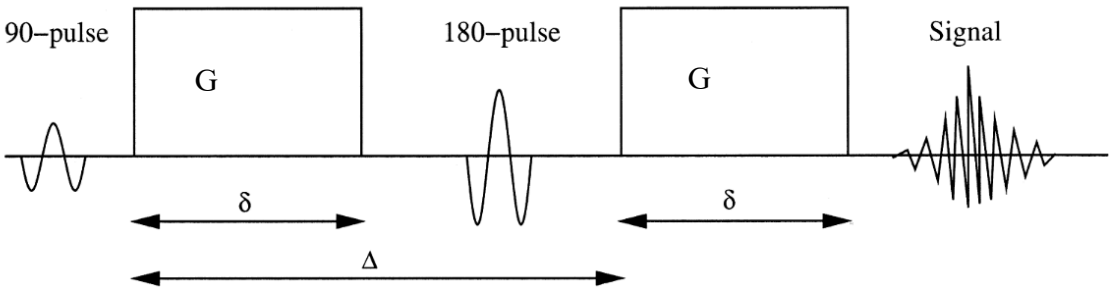

Figure 2.7 The Stejskal-Tanner imaging sequence, where G represents the magnitude of the applied gradient, δ the duration of each diffusion gradient and Δ the duration between the application of the two gradients - adapted from [52].

Whereas the first applied gradient is responsible for a phase shift in proton spins, the second one will be cancelling the gained phase shift for stationary molecules. However, diffusing molecules will not allow the rephasing by the second gradient, since they are changing position during its application [50]. Faster molecules travel a wider distance, which will translate in more signal loss which is represented by darker image voxels [53]. So, image contrast in DWI is based on the differences in diffusion magnitude. The diffusion-weighted contrast can be described by the Stejskal-Tanner equation (Equation 2.2) which explains the signal intensity decrease due to Gaussian diffusion.

$$S_i = S_0 \, e^{-\,b\, ADC_i} \qquad (2.2)$$

where S_i refers to the diffusion-weighted signal intensity at a given voxel with gradients applied along direction i, S_0 refers to the original signal or the diffusion-weighted signal intensity when no gradients are applied, the b-value refers to the LeBihan's factor [54] that describes the diffusion sequence, gradient strength and physical constant, and ADC_i is the ADC at direction i. For rectangular gradient pulses, the b-value can be obtained by Equation 2.3.

$$b = \gamma^2 \, G^2 \, \delta^2 \left(\Delta - \frac{\delta}{3}\right) \qquad (2.3)$$

where γ is the gyromagnetic ratio, G the gradient's amplitude, δ the duration of each diffusion gradient and Δ the duration between the application of the two gradients.

It is important to note, using Stejskal-Tanner equation, that an increase in the b-value increases the degree of diffusion weighting and it is related with a loss of signal intensity along the direction of the applied gradients.

Anisotropy vs isotropy

Depending on tissues' properties – type, integrity, architecture and presence of barriers – water molecules will present different diffusivity behaviors [14]. The water molecules in a wider space move randomly in all directions, known as isotropic diffusion. On the other hand, if the movement is confined along a particular direction and molecules will no longer move equally in all directions, it is called anisotropic diffusion. The example of the brain can be used for a better analogy, where the water molecules in the cerebrospinal fluid have an isotropic movement and in the white matter this movement is anisotropic. Whereas in the first case, the diffusion is similar in all directions, in the second, the diffusion is higher along the tract but reduced in the other directions. So, there is a need of applying gradients in more than one diffusion-encoding directions to characterize anisotropic diffusion. These directions should be noncollinear, that is, not applied on the same line.

Diffusion tensor

In order to understand the anisotropy profile in 3D, the acquisition of at least six image sets in noncollinear directions - and one baseline image for a null b-value - is needed. Having six different signal intensities for noncollinear gradient directions, allows the utilization of a multivariate linear regression to calculate the diffusion tensor (Figure 2.8). The diffusion tensor provides a rotationally invariant description of the shape of water diffusion and uses a Gaussian model [53].

Diffusion tensor imaging (DTI) [55] is a non-invasive MRI-based technique that models diffusion using the diffusion tensor, a 3 x 3 positive symmetric matrix of vectors. In each voxel we get the information

about direction and magnitude of diffusion, by relating the measured signal with the applied gradient. This technique is highly sensitive to changes in diffusion, which allows to indirectly infer about biological tissues' micro- and macro- structure and tissue orientation.

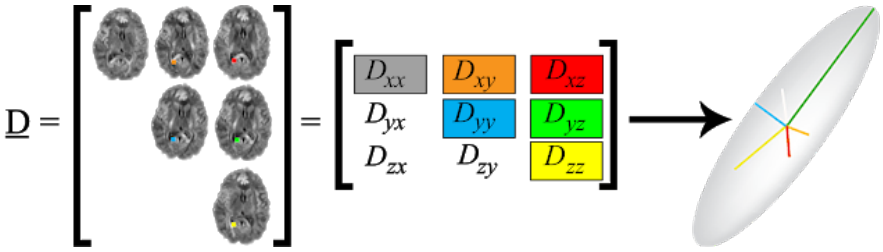

Figure 2.8 From diffusion image to tensor. Note that we only need to apply the gradient in six different directions to generate a 3 x 3 matrix, because $D_{xy} = D_{yx}$, $D_{xz} = D_{zx}$ and $D_{yz} = D_{zy}$ - adapted from [56].

Diffusion tensor metrics

From the diagonalization of the diffusion tensor, three orthogonal eigenvectors ($\overrightarrow{e_1}, \overrightarrow{e_2}, \overrightarrow{e_3}$) and three positive eigenvalues ($\lambda_1, \lambda_2, \lambda_3$) are obtained [53] (Figure 2.9). The eigenvectors reflect the diffusion direction (for instance, $\overrightarrow{e_1}$ is the major eigenvector which points in the direction of fastest diffusion), whereas the rotationally invariant eigenvalues reflect the length of diffusion. λ_1, also called the axial diffusivity (AD), is the principal eigenvalue since it reflects the magnitude of greatest diffusion (Equation 2.4). The second and third eigenvalues (λ_2 and λ_3, respectively) can be averaged to obtain the radial diffusivity (RD), the contribution of diffusion in the transverse plane (Equation 2.5). Other combinations of eigenvalues can be performed to calculate useful metrics of diffusion, including the mean diffusivity (MD) and fractional anisotropy (FA). MD can be calculated as the mean of the three eigenvalues, reflecting the total amount of diffusion for each voxel (Equation 2.6). The most widely used measure for quantifying the degree of anisotropy in each voxel, FA [57], is able to characterize the microstructural integrity of biological tissues (Equation 2.7). FA ranges from 0 and 1, meaning maximal isotropic diffusion and maximal anisotropic diffusion, respectively. In other words, FA gives how far the tensor is from a sphere. Color-coded FA maps [58] can be generated by assigning a color accordingly to the principal diffusion direction (red to left-right, green to anterior-posterior, and blue to superior-inferior). By combining the directional information of individual voxels main tracts are reconstructed.

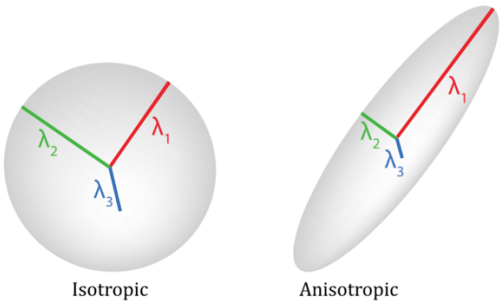

Figure 2.9 Different shapes of the diffusion tensor, and its relationship with diffusion eigenvalues - adapted from [56].

$$AD = \lambda_1 \quad (2.4)$$

$$RD = \frac{\lambda_2+\lambda_3}{2} \quad (2.5)$$

$$MD = \frac{\lambda_1+\lambda_2+\lambda_3}{3} \quad (2.6)$$

$$FA = \sqrt{\frac{1}{2}}\frac{\sqrt{(\lambda_1-\lambda_2)^2+(\lambda_1-\lambda_3)^2+(\lambda_2-\lambda_3)^2}}{\sqrt{\lambda_1{}^2+\lambda_2{}^2+\lambda_3{}^2}} \quad (2.7)$$

Other quantitative metrics can be explored [18] to obtain a novel biophysical characteristics of the tissue being studied, namely linear anisotropy (C_l), planar anisotropy (C_p), spherical anisotropy (C_s), attenuation coefficient (AC) map and relative anisotropy (RA). However, it is important to note that all DTI metrics consist of an indirect approximation of tissue microstructure and the investigator should have precaution regarding its interpretation [59].

One of the biggest challenges in DTI is to choose an intuitive way of representing the diffusion tensor [14]. One can either represent the tensor information using one or four scalars, respectively, if we are looking at a single metric or color-coded maps (three elements for RGB and one for brightness). A more visual way of representing the diffusion tensor information is through an ellipsoid [57], an iso-surface of Gaussian diffusion probability that is created based on the eigenvectors and eigenvalues of diffusion [60]. The ellipsoid reflects the ADC in each direction at a specific time. In isotropic movement, the ellipsoid is a sphere because the ADC has the same value in all directions. On the other hand, the ellipsoid in anisotropic movement has a prolate (elongated) shape, reflecting the increase ADC along the direction where there is no constraint for the movement (Figure 2.10). Ellipsoids are the most common example of various small 3D objects that portray the diffusion tensor, also called glyphs [53]. Glyphs describe the tensor by its size, shape, location, and color [14]. However, glyphs lack a global characterization of the tensor, which can be achieved using a method named tractography.

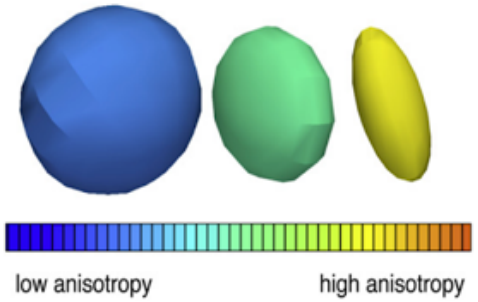

Figure 2.10 Diffusion ellipsoids - adapted from [53].

2.2.2 Tractography

Tractography is an advanced post-processing step that uses the diffusion tensor information to visualize streamlines in 3D, and consequently, extract some of its properties, namely number, density, thickness and directionality. Its main principle is based, firstly in the computation of the diffusion tensor at a particular voxel, and then, in following a streamline in 3D from voxel to voxel. The step of defining the initialization voxels from which the streamline will be propagated, is called seeding [14]. The initialization voxels can be defined manually by drawing a region of interest (ROI) in the DTI image. Since the diffusion image has limited spatial resolution [49], it can be useful to draw the ROIs in the anatomical or functional image to restrict the fiber tracking to a particular area of interest, which can be called the process of "virtual dissection". Also, ROIs can be defined based on automated methods [61]. The second step of tractography is propagation, which can be done using different types of algorithms, classified as deterministic or probabilistic [53] (Figure 2.11). Deterministic, or streamline tractography, uses computational methods to generate discrete curves or trajectories, such as Euler's method, second or fourth order Runge-Kutta, and fiber assignment by continuous tracking (FACT). In FACT [62], the user defines the initiation voxels and the termination based on well-defined stopping criteria, namely the maximum turning angle and the minimum FA. In this algorithm, at the edge of the voxel the tracking follows the direction of the main eigenvector of the next voxel, and so on, until the stopping criteria is reached. For determinist algorithms different interpolation methods exist, including tri-linear and Runge-Kutta of second or fourth order. In probabilistic algorithms, it is taken into account the expected uncertainty in the tracking, due to different factors (noise, patient movement distortions or uncertainty in the orientation of the diffusion ellipsoid). The choice of the method depends on the application [14]. If the goal is to define the most likely path of a fiber, one should use a determinist approach. On the other hand, if the goal is to observe all the possible paths and the likelihood of a voxel being part of a fiber, probabilistic tracking is the preferred choice. In order to evaluate tractography pipelines, an online system has been developed which tests the output effect of different components (acquisition parameters, modelling techniques, tractography parameters and algorithms) [63].

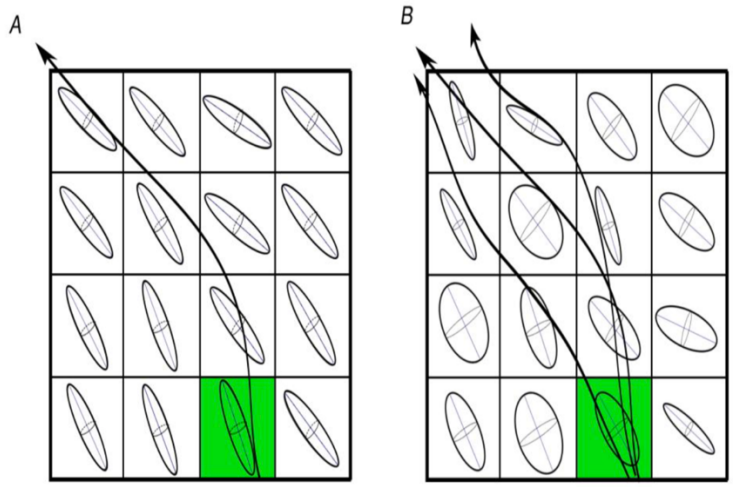

Figure 2.11 Schematic comparison between two tractography propagating methods, a deterministic (A) and a probabilistic (B) algorithms starting from the seed point (green) - adapted from [64].

A limitation of tractography can be the unfeasibility of defining if the movement along the fiber is in the antegrade or retrograde direction [47]. For probabilistic methods, its accuracy is still limited by the diffusion tensor information and the method of constructing the probability density function.

2.2.3 Diffusion tensor imaging workflow

Currently, there exist several software packages that are involved in different stages of DTI processing and analysis [14]. An adequate choice of software is mainly centered in the steps of the diffusion pipeline that one would like to follow, the study application (brain or other organs) and the tractography algorithm behind it. For instance, DSIStudio [4] is a tractography software that is applied on surgical planning and histology studies. It is used mainly for tensor estimation, ROI analysis and tractography. The tractography algorithm that it uses is FACT, a common DTI deterministic algorithm present in most DTI software packages. In software packages like MRtrix [65], Dipy [66] and DSIStudio, instead of using a voxel-based index - like FA or generalized fractional anisotropy (GFA) -, an orientation distribution function (ODF)-based index is used for defining fiber tracking termination. Particularly, it utilizes the ODF-based index quantitative anisotropy (QA) that allows a reduction of partial volume effects and noisy fibers, improving overall tracking accuracy [4]. In a 2015 international tractography challenge, this software has been shown as the most accurate in mapping the human connectome by diffusion tractography, comparing with other 96 submitted methods [67]. Tractometer was the tool used to quantitatively compare each method with the ground-truth bundles, created from multiple whole-brain global tractography maps.

The DTI pipeline can involve different steps, shown in Figure 2.12, such as the definition of an acquisition protocol taking into account the application field, artifact handling, data quality control, the choice of a reconstruction algorithm, visualization and quantitative analysis on the extracted metrics.

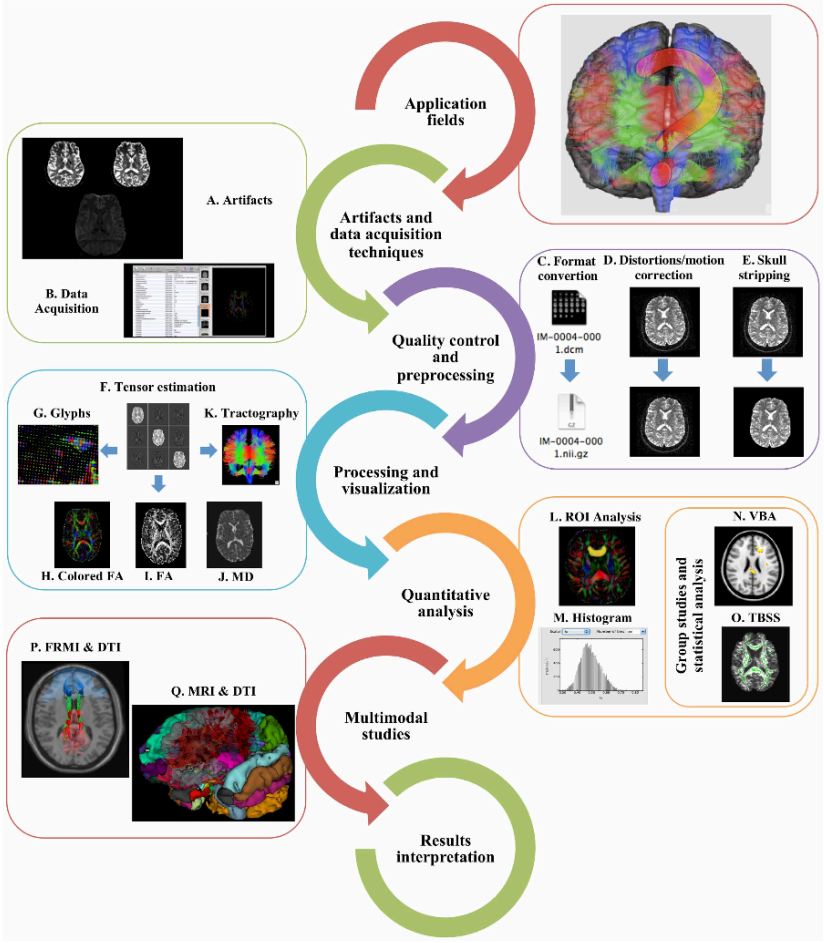

Figure 2.12 Main important steps of the DTI workflow - adapted from [14].

2.2.4 Motion distortion and eddy currents correction

DTI images suffer from artifacts, that can be originated by different sources, including the hardware of the system that applies the gradient, the sequence itself, the acquisition strategy and the subject motion during the MR acquisition [14]. Particularly, subject motion results in a spatial shift of the images. Additionally, since the gradients are applied on and off for a longer time in DTI acquisitions, eddy current distortions can arise due to perturbations in the local magnetic field. These perturbations originate inductions in the conducting surfaces of the MRI scanner, which results in geometric distortions – contraction and/or shift and shear of the image volumes. These artifacts can preclude a reliable tensor estimation, and consequently affect the information that is obtained from diffusion maps, resulting in the generation of erroneous fiber tracts.

In order to correct for artifacts caused by subject motion, it is possible to reduce the scan time by using an echo planar imaging (EPI) sequence, for instance. On the other hand, this sequence can be more sensitive to other artifacts [68], namely, eddy current distortions, field inhomogeneities at B0 (that are more pronounced at higher fields), image blurring and limited resolution from T2. For instance, B0 distortion originates both spatial shifts, geometrical distortions and intensity variation. In order to correct EPI distortions, when using a 3T field or higher, it is important to do parallel imaging with, for example, sensitivity encoding (SENSE). This is possible by the use of phase-array coils that decrease readout times by reducing echo train and increasing signal-to-noise ratio (SNR). Total readout time (in seconds) can be defined as the time taken to acquire all phase encode steps required to cover the k-space, that is calculated by Equation 2.8 for a Philips scanner [69]. Overall, shorter readout times make the sequence less sensitive to artifacts.

$$Total\ readout\ time\ (in\ s) = Number\ of\ echoes\ \times\ Effective\ echo\ spacing \quad (2.8)$$

where,

$$Effective\ echo\ spacing = \frac{Water\ fat\ shift\ (per\ pixel)}{Water\ fat\ shift\ (in\ Hz) \times Echo\ train\ length \times Acceleration\ factor\ (SENSE)} \quad (2.9)$$

When the acquisition strategies – also called prospective (real time) correction – are not enough to deal with artifacts, preprocessing – also called retrospective correction –, should be applied to DTI data. Essentially, the correction of motion and eddy current distortions can be done by using tools that do volume registrations, respectively, rigid body and affine registrations to the diffusion b0. Although its advantages, it is important to note that retrospective correction depends on the effects of subject motion and on the utilization of non-linear approaches, that can assume specific model assumptions, that can introduce non-physiologic factors into the images [68].

One of the most known tools for retrospective correction is the FMRIB's software library from FSL [70], that includes both "eddy" and "topup" packages. "eddy" from FSL is used to correct both for eddy current distortions and patient motion. So that "eddy" can distinguish individual variations that come from the diffusion signal, from those that come from eddy and motion distortions, the DTI data has to follow two main assumptions. Firstly, that there is a sufficient number of diffusion encoding directions that span the entire diffusion sphere (with a higher b-value needing of a larger number of diffusion directions), and secondly, that two acquisitions in opposing phase-encoding (PE) directions, such as AP/PA (anterior-posterior and vice-versa) or RL/LR (right-left and vice-versa), are obtained [71]. On the other hand, "topup" is used to estimate the susceptibility induced distortions, that causes geometrical

distortions, due to the existence of tissues with different magnetic susceptibilities. The susceptibility induced field can be calculated using the two acquisitions with opposing PE directions. The calculated field is the one that, when applied to the two volumes with opposing directions, maximizes the similarity between the unwarped images [72]. That way, “topup” results can be used as an input for “eddy”, to correct for susceptibility induced distortions priory to eddy currents and subject motion correction.

3 STATE-OF-THE-ART

Diffusion-weighted imaging (DWI) is a non-invasive MRI-based technique that was firstly introduced in 1985 [73]. It has been considered a promising *in vivo* tool for accessing the microstructure and pathophysiology of tissues. While DWI refers to the contrast of the acquired images, diffusion tensor imaging (DTI) is a type modeling of the DWI datasets [14]. DTI has been widely used in clinical practice, with acknowledged success mainly in brain studies. Among the most important applications of DTI are the study of white-matter abnormalities, namely in stroke and brain tumors, neurodegenerative disorders, neuropsychiatric disorders, mild cognitive impairment, development disorders, movement disorders and neurogenetic developmental disorders [14]. Also, a few studies have identified white-matter changes during neurodevelopment and ageing [74]. With a growing ageing population, also more brain age-related disorders arise, which makes the investigation of age-related differences in white matter a crucial task. In particular, a study [75] has shown that ageing affects the integrity of some white matter tracts. Other studies include the understanding of brain connectivity, where efforts have been made to map the human connectome in combination with other imaging modalities [76]. In addition, DTI has been in growing expansion in the field of imaging genetics [77] investigating the interplay between genes, brain and behavior. In the future of brain DTI, this technique is expected to be valuable in disease treatment planning, detection of preclinical markers, and microstructural abnormalities [14].

Diffusion tensor imaging beyond the brain

DTI applications also extend to other tissues and organs beyond the brain, namely the spinal cord [78], [79], peripheral nerves [80], [81], heart [16], breast [82], [83] and skeletal muscle [81], [84]. Despite the feasibility has been proven for DTI in a growing amount of applications, its impact in radiological practice is still limited. Particularly, a study regarding DTI of the skeletal muscle has investigated age-related changes in the medial and lateral gastrocnemius, muscles of the lower leg [85]. They have found an increase in FA with age, although not statistically significant, and a significant fiber length decrease. The former can be explained by a decrease in fiber diameter with a consequent decrease in the tertiary eigenvalue (λ_3), that characterizes muscular atrophy with ageing.

Technical advances have enabled the extension of DTI applications to the abdominal and pelvic organs [86] including the liver [87], pancreas [88], kidneys [15], [89] (Figure 3.1), uterus [90] and prostate [17], [91], [92]. DTI of these organs has been particularly useful in the evaluation of disease states in organs with highly directionally arranged structures and in the diagnosis of focal lesions. Although further investigations are needed to improve some technical aspects, DTI should be integrated in the multimodal clinical practice for these organs.

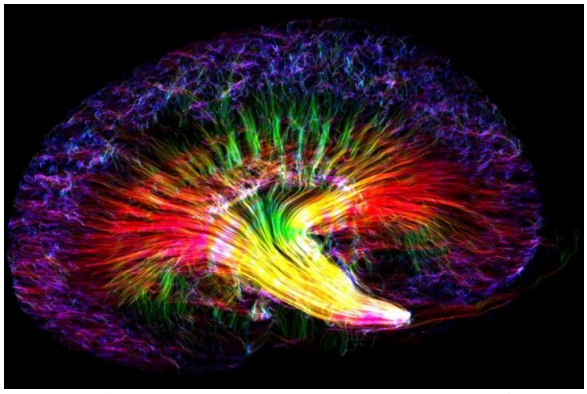

Figure 3.1 DTI of a mouse kidney, created using DSI Studio by Nian Wang, Center for In Vivo Microscopy (Directed by Dr. G. Allan Johnson), Duke University, U.S – adapted from the BMC 'Research in progress' 2018 competition results [93].

Normal prostate diffusion tensor imaging

Although previous studies [94], [95] have thoroughly investigated the diffusion of the prostate using DWI, a quantitative study of diffusion anisotropy was not possible to be performed, since it could only be achieved by measuring the diffusion tensor. The first study to prove the feasibility of *in vivo* prostate DTI was published in 2004 [17]. DTI images of six healthy subjects (mean age of 29 years old) were acquired on a 1.5 T system using a single-shot diffusion-weighted echo-planar imaging sequence applied in 7 directions. This sequence allowed to overcome aspects that were limiting its use in the abdomen, including poor SNR and movement artifacts [96]. This study was useful to establish the best acquisition and processing techniques for prostate DTI data, including evaluation of two acquisition modes - low-bandwidth with the receiver coil in phased-array mode comparing with high-bandwidth with the receiver coil converted to linear mode -, the choice of the number of diffusion-encoding directions, the use of a linear array surface coil comparing with a rectal coil, and the optimization steps to minimize distortions caused by eddy currents. Regarding the acquisition mode, the low-bandwidth mode presented a higher SNR, but also more geometrical image distortions. These distortions could potentially be reduced by the use of postprocessing methods of correction that require an increased acquisition time for its implementation. Since this increased acquisition time is incompatible with the absence of increased patient's motion, the choice of the high-bandwidth with the receiver phased-array coil converted to linear mode turned out to be the best option. In addition, the lower SNR of this mode can be compensated by the acquisition of multiple averages. Using a surface coil as receiver was a better option than the endorectal coil, that originated field inhomogeneities artifacts despite its higher SNR. Regarding the choice of the number of diffusion-encoding directions, in this study [17] they have used 7 directions, using a combination of tetrahedral/orthogonal sensitization. Although the acquisition of a large number of gradient directions has shown to yield good results for the brain DTI - for instance, 61 directions originated more fibers than 6 directions [97] -, it is related with a longer imaging time, which is incompatible with the most of body organs due to subjects' motion. In order to establish a consensus on the number of diffusion-encoding directions for prostate DTI, Kim et al. 2012 [91] have prospectively analyzed DTI images at 3T from twelve healthy subjects subdivided into three groups with a different number of non-collinear directions – 6, 15 and 32 (with the respective acquisition times of 2 min 54 s, 6 min 51 s and 7 min 17 s). They have shown that, although the mean FA in the PZ was statistically significant different among the three groups, significant differences were not found in the SNR of these groups. So, they have concluded that the number of diffusion-encoding directions tested had no significant effect on overall imaging quality.

The study from Sinha and Sinha 2004 [17] was also useful in establishing normative diffusion tensor values for the PZ and the central gland (CG) of the prostate, including the eigenvalues, mean eigenvalue, MD, FA and anisotropy measure (A_σ), for each patient. The latter does not require diagonalization, which could result in a higher accuracy in measuring diffusion. However, the use of A_σ in this study had no particular advantage comparing with FA. The MD found for the PZ ($1.95 \pm 0.08 \times 10^{-3}$ mm^2/s) was higher than the MD for the CG ($1.53 \pm 0.34 \times 10^{-3}$ mm^2/s), which can be explained due to tissues' microstructure. Whereas, the former is composed mostly by loosely fibers, the latter is comprised by compact and well-oriented fibers. The PZ and CG presented similar values of FA (0.46 ± 0.04 and 0.40 ± 0.08, respectively), but these were slightly higher for PZ, which is non-compliant to CG's greater structural organization. Also, they have obtained several diffusivity maps, including the tensor images in each direction, eigenvalues' maps, FA maps, color anisotropy maps and color maps of the fibers' directions. The diffusion in the prostate was found to be described by a prolate model ($\lambda_1 > \lambda_2 = \lambda_3$) being characterized as anisotropic diffusion, that occurs mostly in the superior-inferior direction.

Overall, this study was an indicator of the possibility of using the diffusion tensor information and derived parameters to identify microstructural changes of the prostate, before its occurrence could be detected in larger scale.

More recently, a study [92] has focused on establishing normative acquisition parameters (including b-value, slice thickness, matrix and FOV values) for prostate DTI on a 3T MRI system, so that there is a consensus on normative FA and MD values for the PZ and the CG of the prostate in healthy subjects. The MD in the two regions confirmed the pattern identified by Sinha and Sinha 2004 [17]. However, the FA found followed an opposite pattern comparing with that study, meaning that, the FA on the CG (0.26 ± 0.06) was higher than the FA on the PZ (0.16 ± 0.03), which is concomitant with the microstructural organization of these two regions. Additionally, tractography findings were mostly color-coded in blue (Figure 3.2), which has confirmed the expected superior-inferior orientation of the prostate gland fibers. Also, darker blue on the CG has shown an increased anisotropic diffusion in this region, which is compatible with the increased FA.

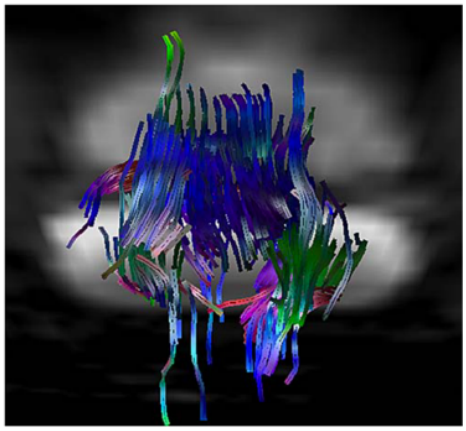

Figure 3.2 Tractography of the prostate gland, with a dominancy of blue tracts (superior-inferior orientation), especially in the CG – adapted from [92].

Prostate diffusion tensor imaging both in cancer and benign prostatic hyperplasia, and characterization of age-related changes

Many studies [95], [98]–[100] have extended the use of prostate DTI to report the results on PC, in order to evaluate if it was possible to use diffusion parameters to differentiate between benign prostate tissue and cancer. In a recent paper by [18], they have found that eighteen DTI metrics varied considerably between normal and cancer patients and even found a higher fiber tract density in cancer patients. This study has proven that prostate DTI can provide valuable quantitative metrics in the identification and characterization of PC.

Since the age differences may affect DTI parameters, the age effect should be taken into account to allow an early diagnosis of PC using these DTI metrics. A few studies have focused on using DTI for evaluating age-related changes in normal prostate. Whereas in [101] they have found lower FA and higher MD with increased age in the PZ, in [102] they reported higher MD with increased age, in both regions (PZ and CZ). Overall, a decreased fiber integrity in the prostate was related with increasing age.

Furthermore, it is possible to use DTI to differentiate between malignant and benign prostate conditions, as proven by [103]. They have discovered that patients with BPH present significantly higher MD and lower FA, comparing with central gland cancers, suggesting that central gland tumors are more organized and oriented microstructures than hyperplasia foci.

Diffusion tensor imaging of the periprostatic neurovascular fibers

Several studies using DTI of the prostate gland, have focused on PNFs mapping by tractography [104] [105] or PNFs' changes visualization before and after RP [106]. The latter has observed a statistically significant decrease in the number of fibers using non-nerve sparing techniques. A recent study [7] even found a statistically significant positive correlation in the ratio between the number of PNFs, before and after RP, and the ratio between the questionnaire scores for erectile function, also between these two time points. On the other hand, no correlations were found between the degree of PNFs sparing and postoperative urinary incontinence, possibly due to the influence of other factors (including the urethral sphincter damage). Another study [107] has supported the previous findings, with no significant correlations between PNFs' DTI metrics (tract number, length and FA) and the ICIQ-SF test scores on urinary incontinence 6-months pos-surgically. In Paola et al. 2018 [7] the authors found that, after RP, there was a decrease in FA for PNFs at prostate mid gland, which suggests a loss of orientation and arrangement of the fibers. Also, this decrease in FA was accompanied by an increase in MD values, meaning higher water molecules diffusion.

In addition, a few studies have investigated technical aspects of image acquisition and processing on PNFs tractography. A study [108] has evaluated the influence of different FA threshold values (0.20, 0.05 and 0.01) on PNFs fiber tracking, regarding the tract number and length. They have observed that measured parameters significantly depended on FA thresholds, more specifically, for the lower FA threshold analyzed an increase in DTI tract number was observed. However, they have shown that it should be taken into consideration that DTI tracts may not really represent nerve tracts. So, although PNFs tractography has been successfully demonstrated in many studies, its use is still not widely accepted, and caution must be taken when making conclusions. Moreover, a study [109] has compared two methods, DTI using local look technique and DTI using single-shot spin-echo EPI with SENSE, in terms of number of fibers, FA and distortion evaluation by the dice similarity coefficient calculation. They have found that, although no significant differences were found regarding image distortions, the

local look technique has shown to originate an increase in the number of fibers detected and an absence of imaging artifacts on FA maps. Overall, this technique represented an increase in visualization performance, allowing a more accurate depiction of the PNFs, which may help guide nerve-sparing RALRP in order to improve potency outcomes.

Diffusion tensor imaging of the urethral sphincter complex

Whereas studying the PNFs can open a window into the understanding of postoperative erectile dysfunction, studying the urethral sphincter is of major importance to learn the causes of urinary incontinence following RP. For more than 150 years, the preferred method to understand the sphincter complex structure has been the cadaveric dissection of normal adult pelvis [24], which has limitations because of the inaccessibility of the sphincters in the deep pelvis, connective tissue infiltration and structure's small size [110]. Since its precise anatomy has not yet been established, other techniques have been employed, including, sphincter electromyography [8], micro computed tomography [9], evacuation proctography [10], elastography using ultrasound [11], transurethral ultrasound [12] or magnetic resonance imaging (MRI) [13]. In respect to ultrasound to study skeletal muscle, it has some limitations [85], like the fact that it only studies the muscle architecture two-dimensionally, it is applicable to a small area of the organ of interest, and not completely accurate to study muscles that are located deeper in the body, which is the case of the male urethral sphincters. These techniques have allowed a better understanding of the sphincters' anatomy and its correlation with dysfunction and ageing. Regarding the latter, morphological and functional studies have already shown that ageing induces degenerative changes in the urethral rhabdosphincter. A functional study [2] has evaluated several parameters of the function to study how this structure behaves with age and has found that most of the rhabdosphincter parameters - sphincter length, maximum urethral closure pressure and urethral closure pressure during voluntary contraction - significantly decreased with age. Since the age degeneration mechanism occurs mainly due to apoptosis of striated muscle fibers [111] - with a progressively decrease of striated muscle cell density (Figure 3.3), concomitant with a replacement by fat cells and connective tissue -, it is expected a macroscopically alteration of the rhabdosphincter with increasing age, that may explain the higher incidence of urinary incontinence with age. In order to investigate individual morphological variations in the distal sphincter with ageing, a histological study on 25 elderly Japanese men [25], has found that with ageing the sphincteric action is rather weak or incomplete. This probably suggests that the elderly men maintain continence by a different mechanism than the younger men, that involves the backward and upward retraction of the urethra.

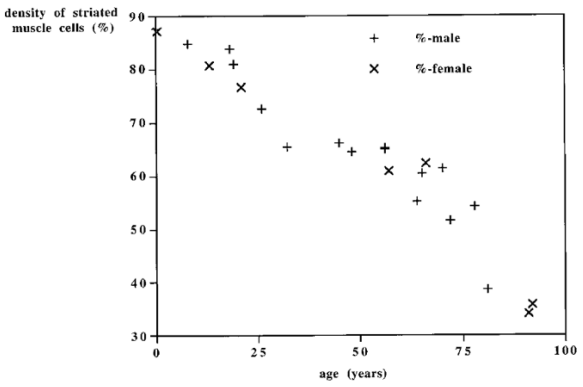

Figure 3.3 Evolution on the density of striated muscle cells of rhabdosphincter with age, both in males and females – adapted from [111].

More recently, in order to study *in vivo* and non-invasively the directionality of the internal microstructure of the sphincters, DTI has emerged as a promising tool that can bring new insights into the urethral sphincter anatomy and function with gender, disease and ageing.

One study [19] has been able to use DTI to understand the anatomy of the normal pelvic floor in five female nulliparous subjects (mean age of 28 ± 3 years old), in order to study pelvic floor dysfunction. In this, they have performed a diffusion-weighted spin-echo planar imaging (SP-EPI) sequence for DTI and a T2-TSE multiplanar sequence to use as anatomical reference. The three eigenvalues (λ_1, λ_2, λ_3), FA and MD, obtained for each one of the subjects, were significantly different between structures of the pelvis, and tractography resulted in a satisfactory representation of these structures including the urethral sphincter complex (Figure 3.4).

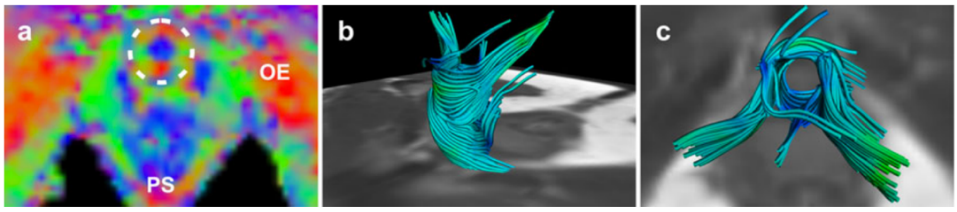

Figure 3.4 Transverse FA map on the inferior pelvic floor of a 31 year female subject (a) – depicting the external obturator muscle (OE) and the puborectal sling (PS)-, and tractography of the female urethral sphincter fibers in an antero-lateral (b) and cranial view (c) – adapted from [19].

However, they have not been able to differentiate between the proximal and distal sphincters. Other limitations of this study were the small sample size and the homogeneity of the patients' dataset in terms of age and gender, which hinders the establishment of objective reference values for the diffusion in pelvic floor structures. Furthermore, this technique can be user-dependent and time-consuming - because a manual selection of ROIs has to be performed for the seeding of fibers. In future studies, using a larger and more heterogeneous cohort, assessing reproducibility of the technique (inter- or intra-observer variability) and using automated methods for tractography might overcome the reported limitations.

Although this study proves the feasibility of DTI with tractography of the pelvic floor in women, the first one [3] to prove it for the male urethral sphincter complex has only been published in 2018 by two of the same authors who firstly showed the feasibility of prostate DTI [17]. They have analyzed eleven healthy young subjects (mean age of 25.4 years old) that were scanned at a 3T MRI system from General Electrics with high-resolution proton-density scans for accurate localization of middle slices and with an additional diffusion-weighted SP-EPI sequence for DTI (32 gradient directions and b-value of 400 s/mm^2). After data processing, diffusion metrics have been extracted using DTIStudio for each one of these participants - including FA, the three eigenvalues (λ_1, λ_2, λ_3), MD and RD. Reproducibility indices, including the coefficient of variation and the repeatability coefficient, were calculated for obtained DTI metrics. In addition, fiber tracking was performed using DTITools with the FACT algorithm. They have been able to clearly differentiate between the two sphincters, namely the proximal or lisso-sphincter and the distal or rhabdosphincter, as well as the longitudinal fiber in a superior-inferior direction (Figure 3.5). The proximal sphincter was the region that reported the higher FA and lower λ_3, significantly different from the metrics extracted for the other muscles. The repeatability coefficient values obtained represent a 15-20 % change from the mean values, allowing the detection of regional differences in that range which is sufficient to distinguish between normal and damaged muscle tissue. The findings for FA and λ_3 suggest a tight packing of fibers in the proximal sphincter, which is required for the more demanding task of maintaining continence at rest. Differences in diffusion metrics between

regions are thought to be correlated with differences in the microarchitecture of the sphincters' tissue, in terms of fibers' density and length. This is a starting point to study its correlation with function, namely with the urethral closure function and urinary incontinence following RP or other prostate surgical procedures. In particular, this technique can be applied to monitor PC patients after lisso-sphincter removal. Also, future studies can use this work as a reference to investigate gender-, disease- and age-related differences in the sphincters. The current study still has its limitations that should be taken into account in future investigations, including the small sample size, the low SNR of muscle because of the large radio-frequency coil used and the corruption by partial volume effects due to the small size of the sphincters.

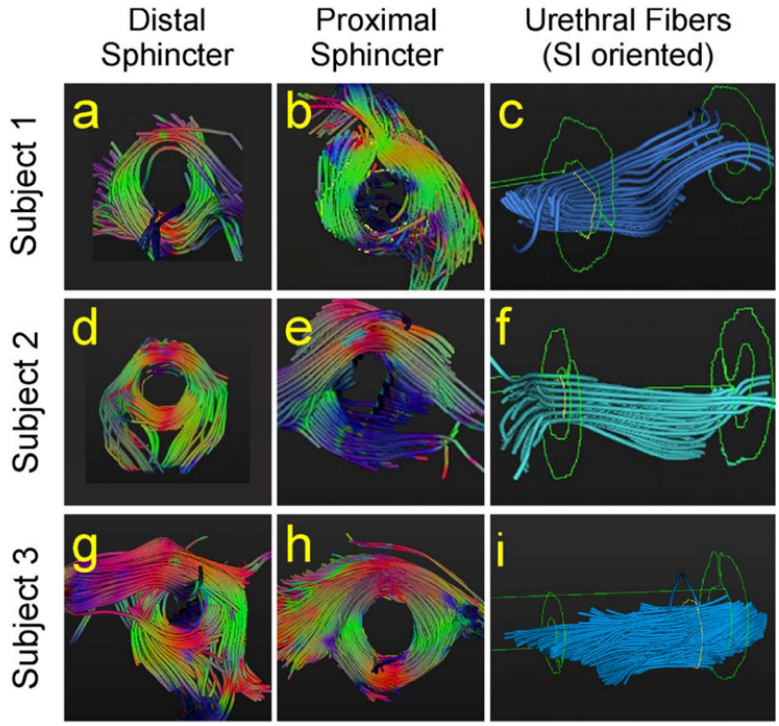

Figure 3.5 Tractography of the male urethral proximal and distal sphincters, as well as the membranous urethra (in green are depicted the ROIs drawn for the tracking, positioned at the level of the sphincters), for three healthy subjects – adapted from [3].

4 MATERIALS AND METHODS

4.1 Ethics Committee approval

This study was carried out under the approval of the CCU's Ethics Committee, involving the acquisition of a DTI sequence in addition to the standard mpMRI already performed at this institution. Participants were told that this additional sequence would not translate in different preparation or risks comparing to the standard MRI protocol, and will increase the scanning time by no more than 5 minutes.

4.2 Study dataset

All male subjects that came to the Radiology Department at CCU, between January 2019 and July 2019, to perform a prostatic, abdominal-pelvic or pelvic MRI were included in this prospective study.

For the exclusion criteria, apart from those typical of MRI scans, such as claustrophobia, implanted medical devices and severe imaging artifacts, being a PC patient previously submitted to any type of treatment for this condition – including radiotherapy, brachytherapy (Figure 4.1) and surgery (Figure 4.2) – was considered as an exclusion criteria.

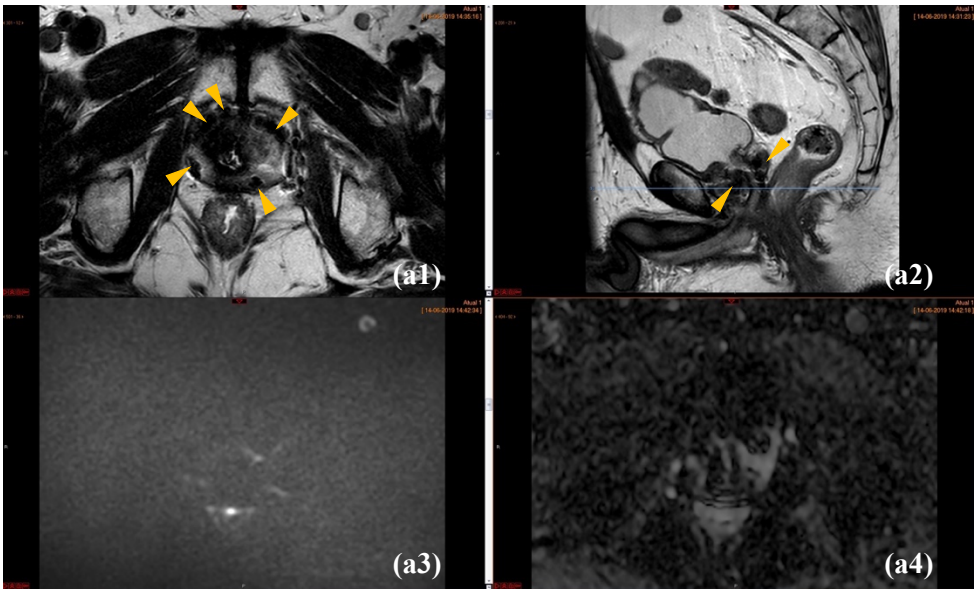

Figure 4.1 Representation of a 70 years old subject submitted to brachytherapy to treat PC, reason to be excluded from the study. The radioactive seeds implanted on the prostate can be seen on the anatomical T2-weighted image (marked by yellow arrows), both an axial (a1) and sagittal views (a2). The presence of these seeds causes imaging artifacts on the DWI with a b-value of a 1500 s/mm^2 (a3) and on the ADC map (a4).

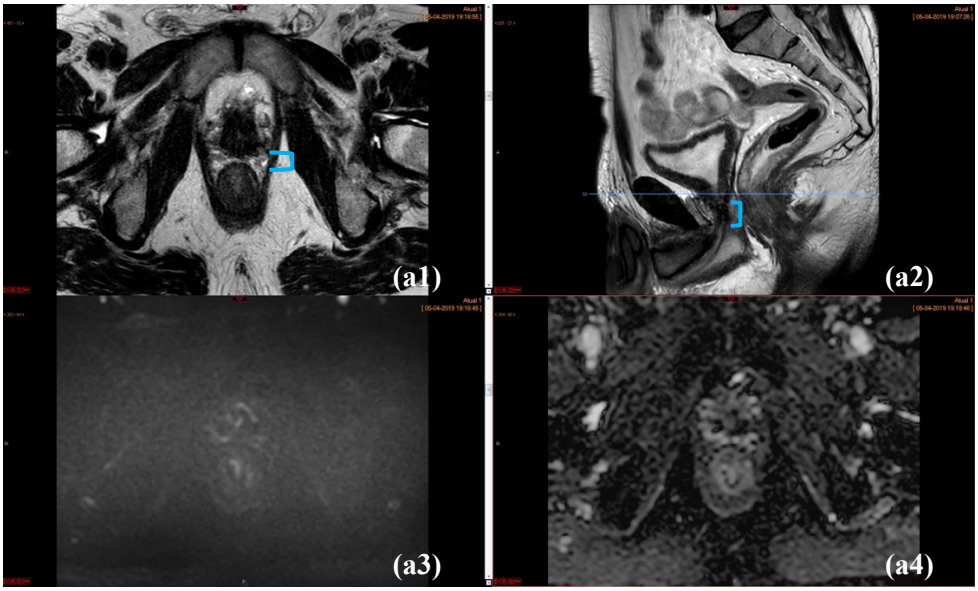

Figure 4.2 Representation of a 70 years old subject submitted to a RP to treat PC, reason to be excluded from the study. The absence of the prostate can be identified on the anatomical T2-weighted image, both an axial (a1) and sagittal views (a2), a DWI with a b-value of a 1500 s/mm^2 (a3), and an ADC (a4). The level at which the prostate is missing is marked in blue.

A total of 118 subjects were scanned during this time period. However, 23 subjects had to be excluded from the subsequent analysis because of the stablished exclusion criteria: 9 of them had no prostate due to surgery, 1 was a cancer patient treated with brachytherapy, 8 were cancer patients treated with external radiotherapy, and 1 was eliminated due to poor image quality - this patient had a hip prothesis which originated severe imaging artifacts. Also, data from 4 of the 5 subjects used for sequence parameters optimization proposes were considered as unsuited for the subsequent analysis, because of poor image resolution.

In the end, a dataset of 95 male subjects was used for data processing and analysis. For the subgroup of the 69 subjects who presented a biopsy-proven diagnosis, these were divided into 3 main groups: 45 patients diagnosed with PC, 14 patients diagnosed with BPH and 10 subjects without any diagnosed prostate condition, considered as the healthy controls (HC). From the PC group, 14 subjects were labelled as TransDouglas, representing a specific population that performed prostate DTI prior to being submitted to a new surgical technique of RALRP in the Da Vinci Xi Robotic System at the CCU, for treatment of diagnosed locally advanced PC.

4.3 Clinical variables

For each subject scanned in this study, a set of clinical variables were collected using the Glintt medical records' system installed on a dedicated workstation at the CCU Radiology Department. These variables included age, body mass index (BMI), latest PSA levels in ng/mL – representing the PSA before the MR exam –, prostate volume (PV) in cm^3, and the clinical diagnosis and treatment (if applicable).

In particular, for the patients in the PC group, Gleason score from biopsy, tumor location, index lesion (in mm) and PI-RADS score were also collected. Also, for TransDouglas patients' additional parameters were collected, including the following preoperative parameters: membranous urethral length (MUL), urethral wall thickness (UWT), levator ani muscle (LAM) thickness, all measured in mm. These measurements were obtained from the T2 weighted MRI images for each patient, using the locations proposed by Robles et al. [112], using the 2D Viewer in Horos v3.3.5. It is important to note that these

measurements were validated by a radiologist with experience in prostatic MRI. The urethral volume (UV) was calculated by Equation 2.10, using the measured MUL and UWT.

$$UV = 10^{-3}\pi\, MUL \left(\frac{UWT}{2}\right)^2 \; in\; cm^3 \quad (2.10)$$

For TransDouglas patients, surgical variables were also collected, including the surgery duration in minutes, the type of nerve sparing technique – left, right or bilaterally - and if a lymphadenectomy was performed. Also, a set of questionnaire scores - EPIC (Expanded Prostate Cancer Index Composite), IIEF-5 (International Index of Erectile Function), ICIQ-SF (International Consultation on Incontinence Questionnaire - Short Form) and IPSS (International Prostate Symptom Score) - were obtained in different time points - preoperatively and 24h, 1 week, 2 weeks, 1 month and 2 months after surgery - to quantify the PC patients' quality of life, and the degree of complications both for erectile dysfunction and urinary incontinence.

4.4 Data acquisition

A standard mpMRI was acquired on a 3T MRI scanner (Ingenia, Philips Healthcare, The Netherlands), equipped with a 32-channel phased array coil, parallel imaging and multi transmission radio-frequency capabilities. This included high resolution T1 and T2 weighted imaging sequences, a diffusion weighted imaging (DWI) sequence with b-values of 0 and 1500 s/mm^2, and a dynamic contrast enhanced (DCE) imaging sequence.

In addition to the standard protocol, a diffusion tensor imaging (DTI) sequence was acquired using single-shot diffusion-weighted echo-planar imaging with parallel SENSE technique, using a reduction factor of 2. This sequence was acquired in the Anterior-Posterior (AP) phase encoding direction using the following parameters: 16 diffusion-encoding directions, b-value of 0 (b0) and 600 s/mm^2, echo time of 68 ms, repetition time of 6600 ms, voxel size of 1.39 × 1.39 × 3 mm^3, matrix size = 68 × 65 × 40 mm^3, FOV = 200 × 200 × 120 mm^3, number of averages = 1, in-plane resolution = 1.39 mm, slice number = 40, slice thickness = 3 mm, gap = 0.3 mm, representing a sequence time of 4 min. Moreover, the spin-echo T2-weighted imaging sequence was acquired using a echo time of 125 ms, repetition time of 4900 ms, matrix size = 288 × 230 × 30 mm^3, FOV = 200 × 200 × 90 mm^3, number of averages = 2, in-plane resolution = 0.31 mm, slice number = 30, slice thickness = 3 mm. The total MRI acquisition time was about 30 min. Figure 4.3 represents the DTI acquisition extent, from a few slices below the beginning of the bladder to the entry of the penile bulb.

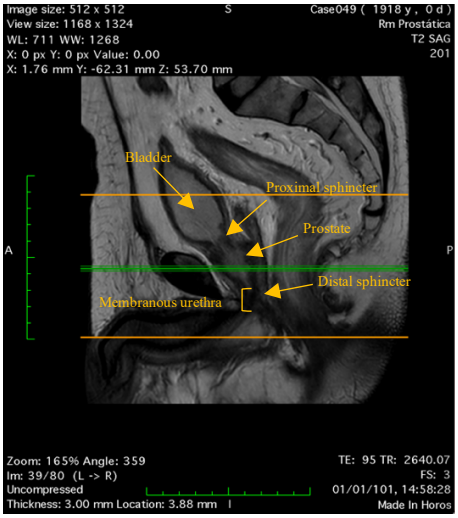

Figure 4.3 MRI T2-weighted image of the mid-sagittal slice, labelled with the relevant anatomy, where the orange lines define the proximo-distal extent imaged in the DTI acquisition.

Each DTI set was corrected for subject motion using the Philips software, by registering each image volume to the b = 0 s/mm^2 (b0) using an affine transform.

Moreover, for 17 subjects there has been acquired an additional DTI sequence in the Posterior-Anterior (PA) phase-encoding direction using the same parameters, but only for a b-value of 0 s/mm^2 (b0). This sequence has the propose to be used in the post-processing steps for susceptibility induced distortions' correction.

Regarding subject's preparation, they need to be fasting for 4 hours before the examination, and to have taken a microlax to clean the bowel. However, no empty bladder requirements are imposed. For DCE imaging, the technicians have injected gadolinium contrast agent through an intravenous catheter inserted in the left arm, using a dedicated system that allows to control the concentration and flux of the contrast agent. A receiver abdominal coil is placed on the subject to amplify the signal.

The first 5 subjects of these study were used for optimization of the DTI sequence, including the choice of the number of gradient directions, the number of slices and an adequate b-value to allow urethral sphincters visualization. The extension of the slices was also changed in order to include the complete distal sphincter. Table 4.1 represents the combinations of parameters that were acquired in order to set the optimal acquisition that represented the best compromise between image resolution and scanning duration.

*Table 4.1 Optimization of DTI acquisition parameters for the first 5 study subjects. The * indicates that this subject had an acquisition extension displaced to a more distal region.*

Case number	b-value (s/mm^2)	Number of directions	Number of slices	Acquisition duration (min)	In-plane resolution (mm)
001'	800	33	25	7.77	1.56
002'	800	33	20	6.44	1.56
001	600	33	30	6.65	1.39
002	600	33	30 *	6.58	1.39
003	600	16	40	4.15	1.39

4.5 Data De-identification

Data acquired was searched on OsiriX Data DB medical imaging library and downloaded into Horos Data DB medical image viewer. All the tags that reflected information that can either identify the patient or the institution and its workers were anonymized, in order to ensure participants' anonymity and protection. Relevant data tags were anonymized using a Python script that uses the de-identification (deid) module from pydicom [113]. In total, 27 DICOM tags (Table 4.2) were chosen, most of them based on the international standard for de-identification provided by DICOM Supplement 142 Annex A1 at [114]. Variables were replaced by strings that take into account its value representation (VR). For instance, those represented by a VR called unique identifier (UI), were replaced by a UID, a series of numeric components separated by '.' that had to be generated for a variable in order to preserve imaging information.

It was created a file that relates information before (Name, ID, patientDir) and after (caseID) the de-identification, in order to trace back each patient. Regarding clinical variables collected from the Glintt medical records' system, those were saved on a excel file that identifies each patient by its unique identifier without any association to subjects' personal information.

Table 4.2 Description on the anonymized DICOM variables, based on its value representation (VR)

DICOM tag	Variable name	Value representation (VR)	Rule for anonymization
8,0012	InstanceCreationDate	DA	1010101
8,0014	InstanceCreatorUID	UI	0.0.00.000000.00.00.0
8,0018	SOPInstanceUID	UI	Generated UID
8,002	StudyDate	DA	1010101
8,0021	SeriesDate	DA	1010101
8,0022	AcquisitionDate	DA	1010101
8,0023	ContentDate	DA	1010101
8,005	AccessionNumber	SH	101010
8,008	InstitutionName	LO	institutionx
8,0081	InstitutionAddress	ST	addressx
8,009	ReferringPhysicianName	PN	FAMILYNAME^GIVENNAME
8,101	StationName	SH	STATION-0101010101
8,104	InstitutionalDepartmentName	LO	deptx
8,105	PerformingPhysicianName	PN	FAMILYNAME^GIVENNAME
8,107	OperatorsName	PN	FAMILYNAME^GIVENNAME
10,001	PatientName	PN	Replaced by “Casexx”, where xx stands for the case number.
10,002	PatientID	LO	Replaced by “Casexx”, where xx stands for the case number.
10,003	PatientBirthDate	DA	1010101
0020,000d	StudyInstanceUID	UI	0.0.000.000000.00.0.000000000000.00000.000000000000000.000.0
0020,000e	SeriesInstanceUID	UI	0.0.00.000000.00.00000.0.0.0000.0000000000000000000
20,001	StudyID	SH	1010101
20,0052	FrameOfReferenceUID	UI	0.0.00.000000.00.00000.0.0.0000.0000000000000000000
32,1032	RequestingPhysician	PN	FAMILYNAME^GIVENNAME
40,0244	PerformedProcedureStepStartDate	DA	1010101
40,2004	IssueDateOfImagingServiceRequest	DA	1010101

PN - person name: character string composed of 5 components (family name complex, given name complex, middle name, name prefix, name suffix)
LO – long string: string of 64 characters max
DA – date (format YYYYMMDD)
SH – short string: string of 16 characters max
ST – short text: text that may contain 1 or more paragraphs of 1024 characters max
AE – application entity: string of characters with 16 bytes max
UI – unique identifier: character string containing a unique UID (a series of numeric components)

4.6 Diffusion tensor imaging processing and Tractography

After data de-identification, some steps were performed prior the fitting of a tensor. A schematic representation of the diffusion processing pipeline for each subject is represented on Figure 4.4.

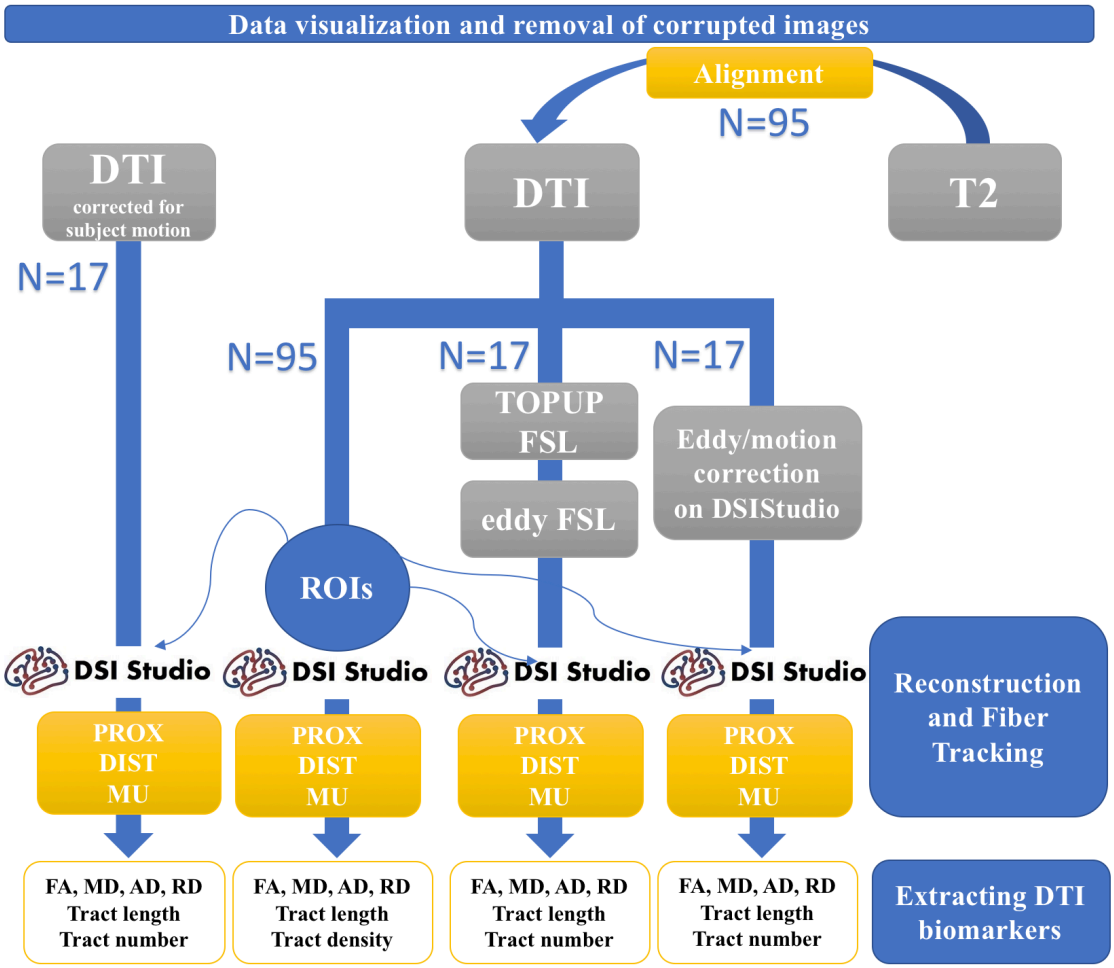

Figure 4.4 Schematic representation of the DTI processing and analysis pipeline.

Firstly, the data was visualized in Horos for individual image quality inspection, and corrupted images were eliminated from the analysis. Then, for the subset of 17 subjects with the b0 acquisition on a PA phase-encoding direction, the susceptibility-induced off-resonance field was calculated using "topup" that follows the method described in [72] as implemented in FSL [70]. The total readout time needed for "topup", calculated using Equation 2.8 described in the Introduction, was 0.02 s. The schematic representations of "topup" and "eddy" input and output are shown in Figures 4.5 and 4.6, respectively. Data corrected for susceptibility-induced distortions was then used as input for eddy currents correction using "eddy" from FSL [71].

For subsequent comparison of eddy currents correction methods, the same subjects were used also for motion/eddy currents correction on DSIStudio [4], the software used on the subsequent steps of the DTI analysis. The principle behind the correction in DSIStudio is based on the application of an affine transform between the diffusion b0 and each diffusion-weighted volume, using image correction as the cost function. If similar results are found using the "topup" with "eddy" correction on FSL and the motion/eddy currents correction on DSIStudio, the latter has the advantages of involving less post-

processing steps and do not requiring an additional DTI sequence acquired on an opposite PE direction, translating in shorter acquisition times.

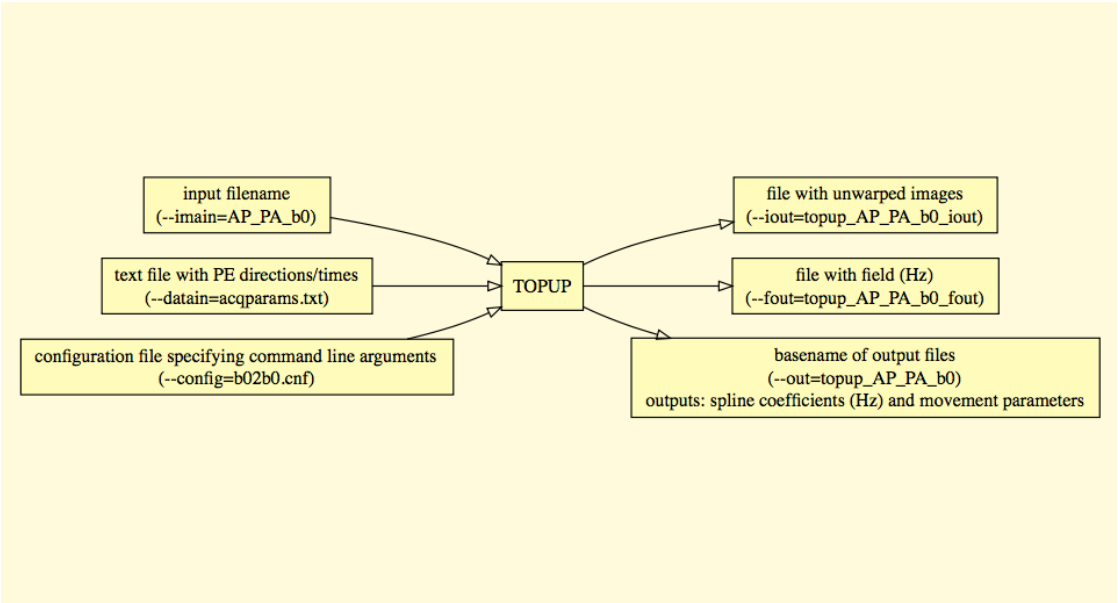

Figure 4.5 FSL's "topup" schematic representation.

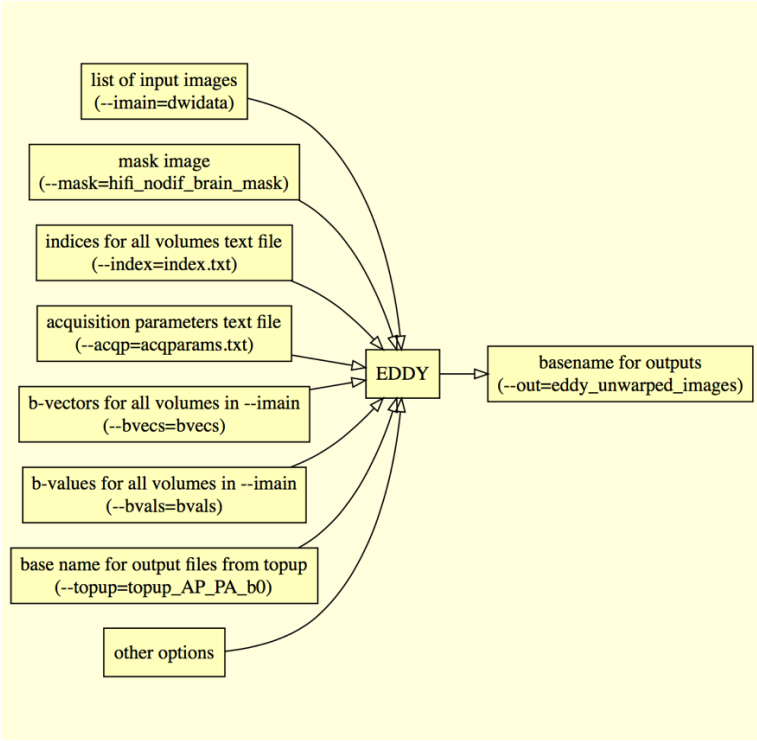

Figure 4.6 FSL's "eddy" schematic representation.

For each subject, a Python script using the SimpleITK package [115] was built to align the T2 images with the b = 0 s/mm^2 (b0) of the original DTI. For that, a rigid transform followed by an affine transform were applied to the T2 image - set as the moving image -, so that the anatomical location could match

the diffusion b0 volume - set as the fixed image, since the diffusion information could not be changed - to future guidance of ROI placement.

The subsequent steps were repeated for each subject using the original DTI data, the DTI data corrected for subject motion during acquisition and, for those subjects with a PA acquisition, also for the eddy current corrected data, both using FSL and DSIStudio motion/eddy currents correction.

DSI Studio was the software used for DTI reconstruction and fiber tracking. Firstly, the source (.src) file was created from each set of DICOM source images by using batch processing. For the eddy current corrected files, the resultant 4D NIFTI file was used as source images to create the .src file, and the adequate bvecs file with the rotated vectors was loaded. The .src quality control file was produced for image quality inspection. Then, a binary mask was setup to filter background outside the prostate and nearby structures (urethra, bladder and rectum) using thresholding, dilation and defragment options on DSIStudio. Under this region, DTI reconstruction was made, performing an eigenanalysis on the calculated diffusion tensor. From this, a fiber tracking (.fib) file was created that was used for fiber tracking.

The deterministic FACT algorithm [4] was used for fiber propagation. For each subject, 3 ROIs were drawn to track the proximal sphincter, 3 other ROIs to the distal sphincter and 2 ROIs to the membranous urethra. Reconstructions of the tracts were obtained by applying ROI gates following Boolean logic. For instance, for both sphincters the first 2 ROIs were AND gates placed symmetrically on both sides of the ring, and the third ROI was a Terminative (NOT gate) in a cylindrical shape, made from the subtraction of two ROIs that surround the sphincter. On the other hand, for the membranous urethra we have placed two AND gates, more specifically, a proximal region near the prostate apex and a more distal one near the penile bulb. Whereas the ROIs for the sphincters were drawn on the color-coded maps based on the lead eigenvector of the original DTI data, the ROIs for the urethra were drawn on the T2 weighted images aligned with the diffusion b0 of the original DTI data. Figure 4.7 shows the ROI placement for the proximal and distal sphincter and for the membranous urethra, respectively, the apex and the bulb.

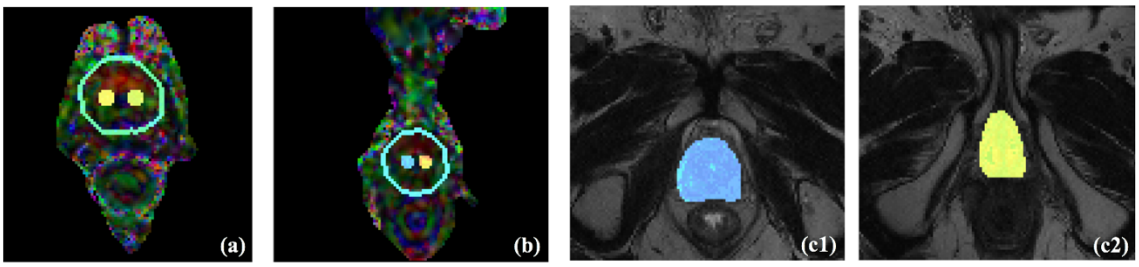

Figure 4.7 Axial views obtained from DSIStudio showing the ROI placement on the color-coded FA maps for the proximal sphincter (a) and distal sphincter (b), and on the T2-weighted image for the apex (c1) and bulb (c2) to track the membranous urethra.

For the proximal and distal sphincters, it was used as termination criteria a threshold of 0.15 for FA and an angular threshold of 75 degrees. For the membranous urethra, the termination criteria used were the same as for the sphincters, except for the angular threshold that was set to 45 degrees. In particular cases, where the number of streamlines produced was very low, the FA threshold was decreased to 0.10 or 0.05 (the latter threshold in fewer cases). Streamlines that had angles above the angular threshold and FA values below the FA threshold were excluded from the tracking. In addition, a step size of 0.69 mm was chosen, and the fiber trajectories were smoothed by averaging the propagation direction with 9%

of the previous direction. Tracts with length shorter than 50 or longer than 200 mm were discarded. A total of 30000000 seeds were placed. Table 4.3 shows the fiber tracking parameters set on DSI Studio that are common to all structures tracked.

Table 4.3 Fixed fiber tracking parameters for the studied structures of the male urethral complex.

Parameter name	Parameter value
Step size (mm)	0.69
Smoothing	0.09
Min length (mm)	50.0
Max length (mm)	200.0
Topology-informed pruning	0
Seed orientation	All
Seed position	Subvoxel
Randomize seeding	Off
Check ending	Off
Direction interpolation	Trilinear
Tracking algorithm	Streamline (Euler)
Terminate if	30000000 Seeds
Thread count	4
Output format	trk.gz

After tracking, the streamlines that passed through the ROIs due to the "brute-force" nature of the algorithm, but are considered to be spurious and outside of the structure of interest, were eliminated manually. For the urethra, the tracts were cut at the levels of the apex and bulb so that it is obtained only the membranous portion of the urethra.

Diffusion metrics, namely FA, MD, RD and AD were computed from these tracts for each patient on DSI Studio - FA is dimensionless, except for the other metrics that are represented in 10^{-3} mm^2/s. Additional metrics, including fiber's length (in mm), number, volume occupied (in cm^3) were collected from the tract statistics file. Fiber's density was calculated for each case, dividing fiber number by volume occupied.

4.7 Statistical analysis

Statistical analysis was performed in RStudio [116] using R v3.5.0. p-values were reported as statistically significant if $p < 0.05$. The main goal of this analysis was to investigate age-related differences on DTI metrics of the urethral sphincters and the membranous urethra. For that, the continuous variables patient age and the DTI metrics tract density, tract length, FA, AD, MD and RD, for each structure (proximal and distal sphincters, and membranous urethra) were analyzed.

Moreover, for each DTI index (FA, AD, MD and RD) not only the mean value within the structure of interest, but also different summary statistics of histogram analysis were extracted and analyzed to investigate the distribution of each DTI metric along the tract. Hence, for each patient it was saved a text file for each metric along every tract analyzed, using DSIStudio on the command line. Then, the function describe from R package 'psych' [117] was used to get the following 14 metrics: standard deviation (sd), median, trimmed mean, median absolute deviation (mad), minimum (min), maximum (max), range, skewness, kurtosis, standard error (se) and the 5^{th}, 25^{th}, 75^{th} and 95^{th} percentiles. In the end, 21 continuous variables were analyzed for each structure.

These variables were subjected to a logarithmic transformation to help data meet the parametric test assumptions and were reported as mean ± standard deviation (SD). Additionally, 3 categorical variables were included in this study, comprising age group (a factor of 4 levels: 5 for subjects aged 50-59, 6 for subjects aged 60-69, 7 for subjects aged 70-79 and 8 for subjects aged 80-89) disease group (a factor of 3 levels: 0 for HC, 1 for PC patient and 2 for subject with BPH) and cancer status (a factor of 2 levels: 0 for non-cancer patients, meaning both HC and BPH, and 1 for PC patients).

Motion and Eddy currents corrections on diffusion tensor imaging biomarkers

It was firstly studied whether any of the DTI metrics varied with statistically significance when obtained from data with and without both motion and eddy currents corrections. This analysis was performed on 17 subjects with the PA acquisition, and the DTI metrics evaluated were the ones mentioned above, apart from tract number replacing tract density. For that, it was used a t-test to compare each metric between the original DTI data and the DTI data corrected for subject motion using the Philips software. Normality of each of the groups and homoscedasticity of the pairs that came from normal populations were tested using Shapiro-Wilk and F tests, respectively. If these assumptions were not met, the non-parametric Mann-Whitney test was used. Additionally, a one-way analysis of variance (ANOVA) was used to do a comparison between the original DTI data and two different methods of eddy currents correction, specifically, FSL “eddy” combined with FSL “topup” and eddy currents correction option on DSIStudio. To investigate whether normality and homoscedasticity assumptions were met, Shapiro-Wilk and Levene’s tests were used, respectively, and residuals were plotted. Otherwise, the equivalent non-parametric Kruskal-Wallis test was used.

Relationship between diffusion tensor imaging metrics and age

In order to investigate the hypothesized age influence in each DTI metric, correlations and linear regressions were performed between age and the variables of the 95 subjects suited for the analysis. Firstly, Pearson and Spearman correlations were calculated between each DTI metric and age. Shapiro-Wilk tests were performed formerly in order to check the normality of each variable, and if this requirement was met, the Pearson correlation was calculated (otherwise, Spearman correlations were used).

Then, linear regressions were performed, using age as the independent variable (X) and each of the DTI metrics as the dependent variable (Y). Assumptions for linear regression were confirmed beforehand, namely independence of Y values (known from the design and data collection), linearity of Y with X, homogeneity of variances of Y (homoscedasticity) and normality of Y values for each value of X. Whereas meeting the first assumption was known from the design and data collection, the last three assumptions were confirmed by plotting the residuals of Y.

Moreover, ANOVA tests (or the equivalent non-parametric Kruskal-Wallis tests, for the cases when the ANOVA assumptions were not met) were used to investigate whether the DTI metrics varied significantly between the four age groups – subjects aged 50-59, 60-69, 70-79 or 80-89. Then, a post-hoc t-test (or the equivalent non-parametric Mann-Whitney test) was used to identify significant differences between age decades.

The effect of a prostate condition in the diffusion tensor imaging metrics

In order to check whether having a PC condition, namely cancer or benign hyperplasia, could influence the DTI metrics, the subset of 69 patients with a diagnosis – negative or positive for one of the conditions – was studied. ANOVA tests (or the non-parametric Kruskal-Wallis test) were used to investigate whether the DTI metrics varied significantly between the three disease groups – HC, PC and BPH. Then, a post-hoc t-test (or the equivalent non-parametric Mann-Whitney test) was used to identify significant differences between each pair of disease groups. Subsequently, for the 45 patients in the PC group, linear regressions were performed between age and each of the DTI metrics.

Then, t-tests were used to compare differences in DTI metrics with cancer status, meaning PC patients against non-PC patients (the latter includes both HC and BPH groups described above). For the cases where the criteria of normality and homoscedasticity were not met, the equivalent non-parametric Mann-Whitney test was used.

5 RESULTS

5.1 Study dataset descriptive statistics

Subjects' age distribution

In this section, the main findings of the analysis on the male subjects scanned at CCU, included in the study, are described. The total dataset of 95 male subjects analyzed presented a median age of 66 years old, ranging from 45 to 89. The age distribution of the total dataset is shown by a density histogram divided into bins with a binwidth of 5. (Figure 5.1). One can see that the distribution is almost perfectly symmetrical, but slightly negatively skewed. Also, the histogram shows that most subjects of this study lie around 65 years old.

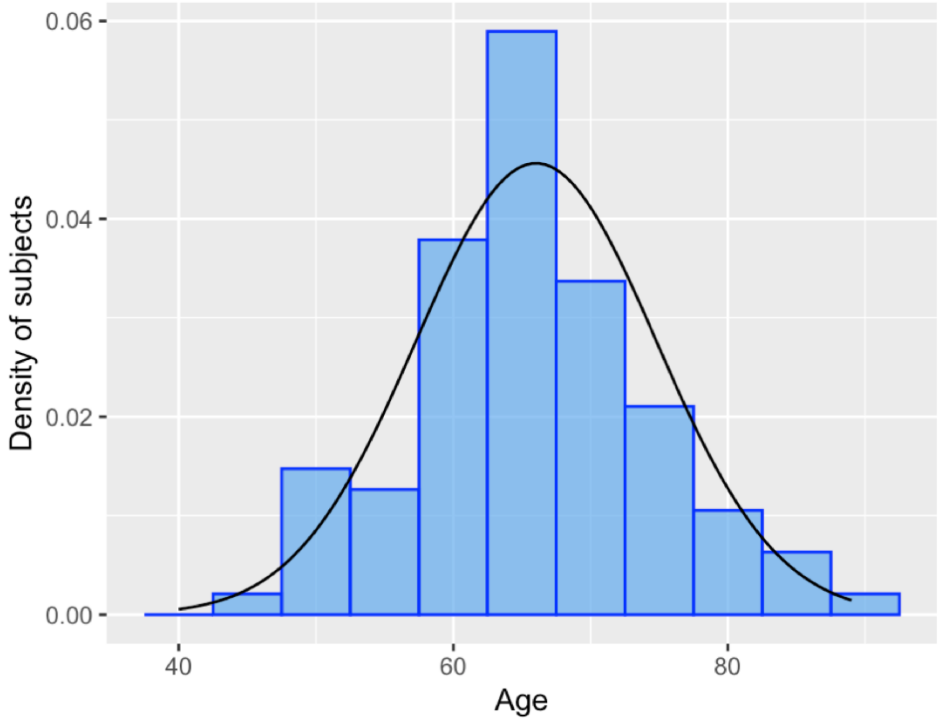

Figure 5.1 Age distribution of the 95 male study subjects. The normal distribution curve that better fits the data is plotted on top of the histogram (in black).

For the subsequent analysis, the total dataset was subdivided by age decades into 4 groups: subjects aged 50-59, 60-69, 70-79 and 80-89, respectively with 20, 42, 23 and 9 subjects. No age group between 40-49 years old was created, since it was only formed by one subject. The subjects' distribution within each age group is depicted in Figure 5.2.

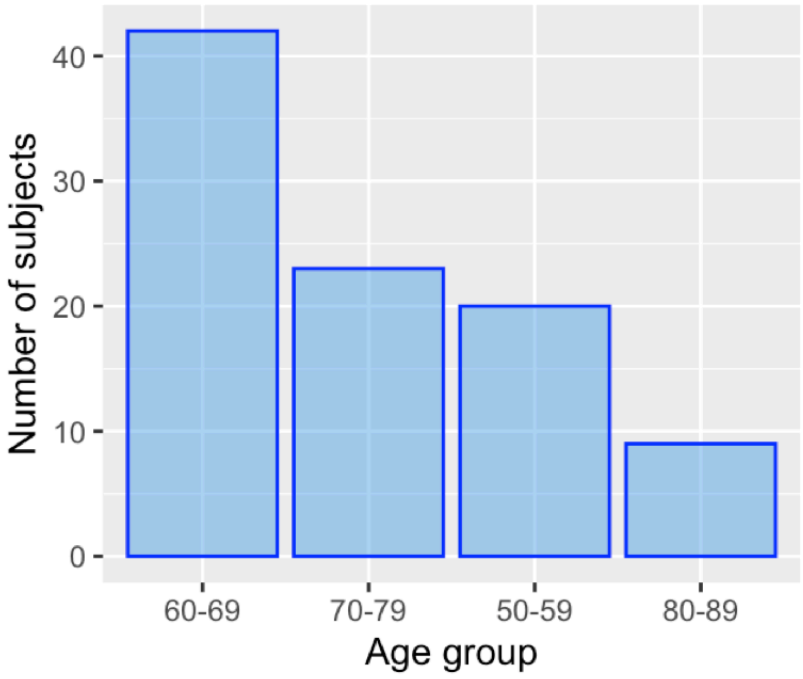

Figure 5.2 Subjects' distribution by age group. The majority of subjects lie in the age group between 60 to 69 years old.

Subjects' distribution by Disease group and Cancer status

For analyzing subjects by the type of prostate condition they presented, 69 of the total 95 subjects with a biopsy confirmed diagnosis were considered. The mean age of the 69 subjects was of 67 years old, ranging between 51 to 89. This smaller dataset was subdivided into 3 main groups –PC subjects and BPH subjects and HC, respectively with, 45, 13 and 11 subjects each– as described in the Methods. A representative subject from each of the disease groups HC and BPH is depicted in Figure 5.3, by means of its T2-weighted MRI (axial and sagittal views), DWI with b-value = 1500 s/mm^2 and an ADC map. The same can be observed for PC subjects, from each one of the tumor location categories – tumor located of the PZ, TZ or both (PZ + TZ) – in Figure 5.4. The represented patient with BPH shows an enlarged prostate, as clearly seen on the sagittal view of the T2 (Figure 5.3 (b2)). Whereas tumors (demarked by yellow arrows in Figure 5.4) appear hyperintense on the DWI b-value = 1500 s/mm^2 (the sequence where they can be easily detected), they appear hypointense on the T2 and on the ADC map. Patient with tumor on the TZ (Figure 5.4 (d)) has a cyst, that appears hyperintense on the T2 (marked by an orange arrow).

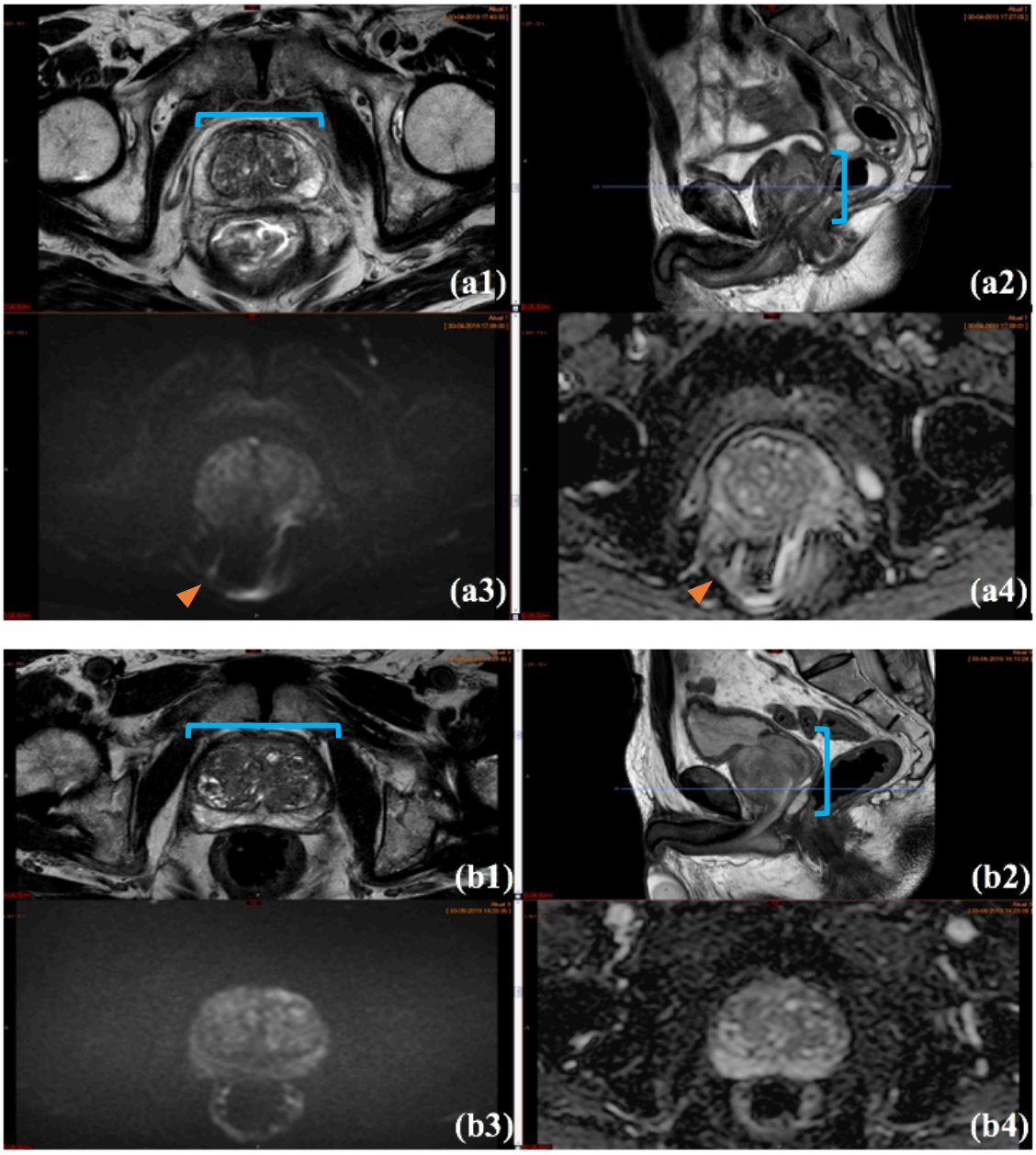

Figure 5.3 Representative 70 years old HC subject with a normal prostate with a volume of 50 cm^3 (a) and a 80 years old BPH subject with a clearly enlarged prostate volume of 110 cm^3 (b). The prostate extension is highlighted in blue. For each subject is shown an anatomical T2-weighted image, both on axial (1) and sagittal views (2), a DWI with a b-value of 1500 s/mm^2 (3), and an ADC (4). Images for the HC subject (a) presented some geometrical distortions caused by air in the rectum, as marked by orange arrows.

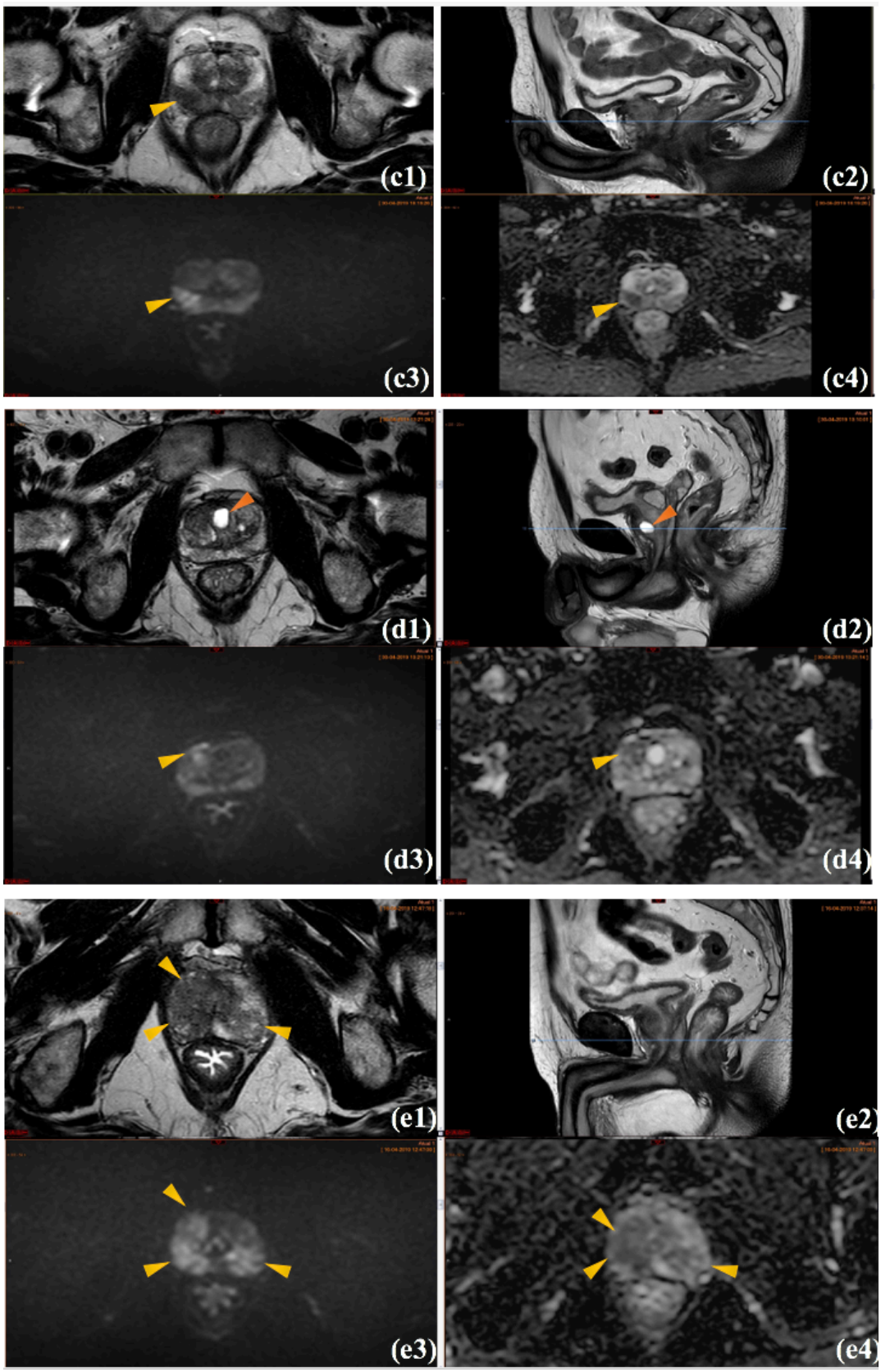

Figure 5.4 Representative 60, 75 and 70 years old PC patients with different tumor locations, namely, with a tumor on the right middle third and apex of the PZ (c), on the right middle third of the TZ (d) and on the anterior right middle third and apex of both PZ and TZ (e). These patients have a Gleason score of 3 + 4, a PIRADS of 5 and an index lesion of, respectively, 25, 25 and 20 mm. For each subject is shown an anatomical T2-weighted image, both an axial (1) and sagittal views (2), a DWI with a b-value of 1500 s/mm^2 (3), and an ADC (4). Tumors are marked by a yellow arrow and a cyst in (d) is marked by an orange arrow.

Additionally, in order to analyze subjects with a prostate tumor against the ones without tumor, the BPH and HC subjects were grouped together in a non-PC group with 24 subjects. Bar plots showing the number of subjects lying within each group, respectively, for disease group and cancer status, are shown on Figures 5.5 and 5.6. The age distribution of subjects within each group is plotted in Figure 5.7. Furthermore, ANOVA testing has shown no statistically significant differences on the patient age of diagnosed subjects between disease groups and cancer status groups, respectively, p-values of 0.789 and 0.565 were found.

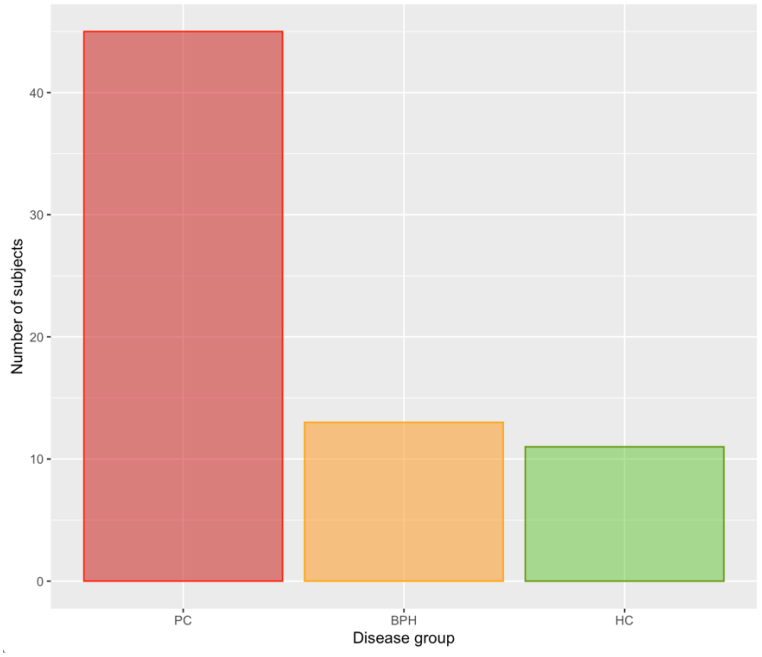

Figure 5.5 Subjects' distribution by disease group. Here the PC group is represented by the red bar, the BPH by the orange and the HC group by the green.

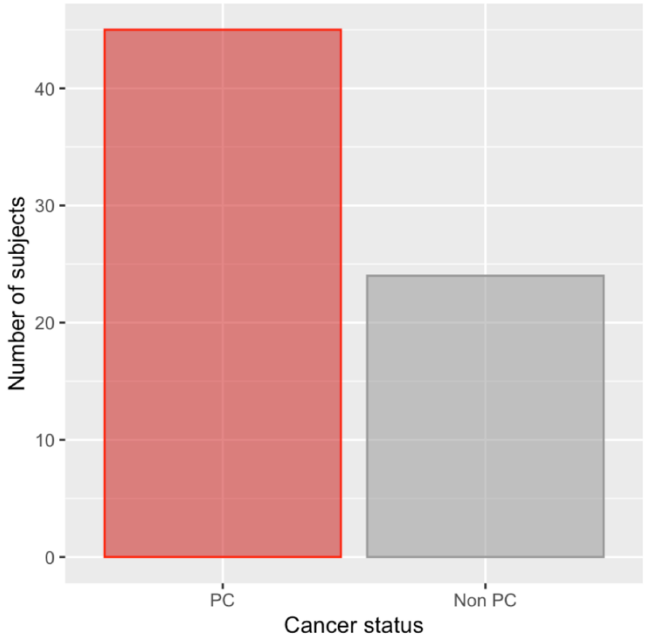

Figure 5.6 Subjects' distribution by cancer status. Here the PC group is represented by the red bar and the non-PC group is represented by the grey bar.

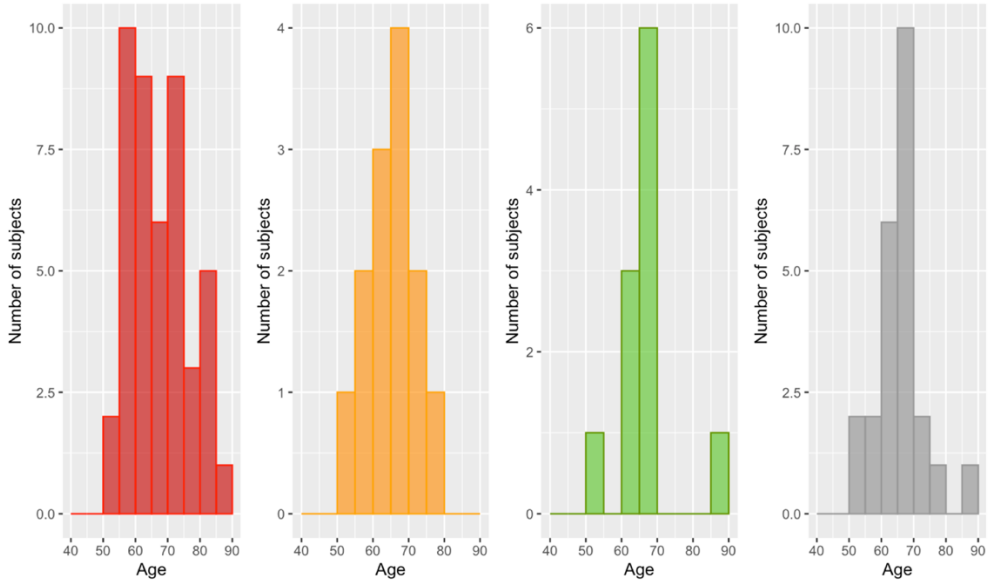

Figure 5.7 Age distribution of patients within each disease group, respectively the PC (red), the BPH (in orange) and the HC (in green) groups. The latter represents the age distribution of patients for the non-PC group (in grey).

Subjects' clinical variables

As described in the Methods, a set of clinical variables were collected for each of the subjects. Table 5.1 summarizes the median, interquartile range (IQR) and the range of values of each of the clinical numerical variables collected for the totality of the subjects in this study and for the diagnosed subjects within disease groups. ANOVA test results have shown no statistically significant differences on clinical variables mean value between disease groups, except for prostate volume. Particularly, a post-hoc Wilcoxon test has shown that the difference lied between the HC with the PC groups (p-value = 0.0246) and the PC with the BPH groups (p-value = 0.0005).

*Table 5.1 Numerical clinical variables for the total dataset (95 subjects) and for each of the individual disease groups of the 69 diagnosed subjects. Each numerical variable was presented as Median; IQR [min.-max.](N), where IQR stands for interquartile range and N for the number of subjects for which that variable information was available. ANOVA (or the non-parametric Kruskal-Wallis, marked by a *) test p-values for the comparison of each variable between disease groups, is shown on the last column. Statistically significant p-values are highlighted in orange.*

Clinical variable	Total dataset	PC patients	BPH patients	HC subjects	ANOVA (or kruskal-Wallis *) p-value
Patient age (years old)	66; 11 [45-89] (95)	67; 14 [51-87] (45)	67; 7.0 [52-80] (13)	66; 5.5 [52-89] (11)	0.789
Body mass index (BMI) (kg/m^2)	26.1; 3.62 [18.3-35.5] (90)	25.9; 3.53 [21.7-34.3] (43)	26.4; 3.13 [20.9-33.15] (11)	26.8; 4.17 [18.3-35.5] (11)	0.782*
Latest PSA (ng/mL)	6.6; 4.3 [0.2-94.2] (79)	7.0; 4.8 [0.2-94.2] (41)	6.3; 2.1 [2.5-9.0] (10)	6.7; 4.0 [2.5-20] (9)	0.445*
Prostate volume (PV) (cm^3)	54.0; 26.0 [14.0-188] (93)	48.5; 18.5 [14.0-108] (44)	67.0; 32.0 [40.0-135] (13)	59.0; 19.5 [23-92] (11)	0.0005*

For patients in the PC group, the categorical variables Gleason score from biopsy, tumor location and PI-RADS score are represented by the pie charts depicted in Figure 5.8. The majority of PC patients have a tumor located on the PZ (56%) and exhibit a Gleason score of 3+4 (53%). A PIRADS score of 4 and 5 has a similar representation (33% and 36%, respectively) among PC patients.

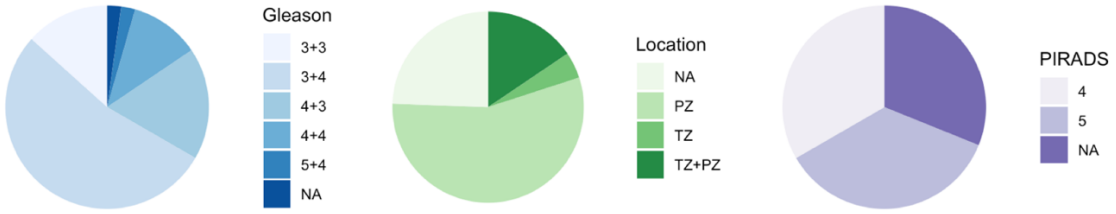

Figure 5.8 Pie charts representing the number of PC patients within each category of Gleason score, tumor location and PI-RADS score. The NA group present in the three categories represents the PC patients for each that information was not available.

Still for the PC patients' group, the distribution of the numerical variable index lesion, meaning the size (in mm) of the largest tumor lesion identified in the image, is represented by a histogram in Figure 5.9. Most subjects have an index lesion with a size of 10 to 15 mm.

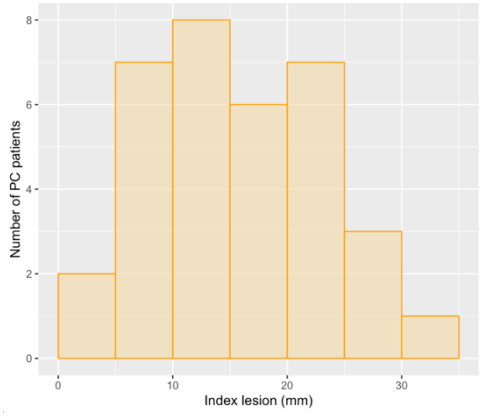

Figure 5.9 Tumor index lesion size (maximum length) distribution for PC patients.

5.2 Effect of the motion and eddy currents corrections on DTI metrics

In this section, results with and without motion and eddy currents corrections were compared. Firstly, let's start by presenting the results on the evaluation of motion correction on 17 subjects. The results of the t-test (or the Mann-Whitney test) for comparing the mean of DTI metrics with and without motion corrected is depicted on Table 5.2. One can see that no statistically significant difference was found between the means of each DTI metric between motion correction groups.

*Table 5.2 Statistical test results for motion correction. Non-parametric tests are marked by an *.*

	Variable without correction	Variable with correction	t / W (*) statistic	p-value
Proximal sphincter	Tract number	Tract number registered	1.521	0.140
	Tract length	Tract length registered	0.810	0.424
	FA	FA registered	0.013	0.990
	AD	AD registered	-0.998	0.326
	MD	MD registered	133*	0.708
	RD	RD registered	150*	0.865
Distal sphincter	Tract number	Tract number registered	1.235	0.226
	Tract length	Tract length registered	147*	0.946
	FA	FA registered	0.471	0.641
	AD	AD registered	-1.755	0.089
	MD	MD registered	-1.562	0.128
	RD	RD registered	-1.380	0.177
Membranous urethra	Tract number	Tract number registered	150*	0.865
	Tract length	Tract length registered	0.181	0.858
	FA	FA registered	0.747	0.461
	AD	AD registered	133*	0.708
	MD	MD registered	120*	0.413
	RD	RD registered	120*	0.413

Secondly, eddy currents correction was evaluated on the same 17 subjects. The results of the ANOVA (or the Kruskal-Wallis test) for comparing the mean of DTI metrics between the three groups – no eddy currents correction, correction with FSL TOPUP and eddy currents correction option on DSIStudio - is depicted on Table 5.3. Once again, no statistically significant differences were found on DTI metrics between groups.

*Table 5.3 Statistical test results for eddy currents correction. Non-parametric tests are marked by an *.*

	Variable without correction	Variable with eddy FSL correction	Variable with eddy DSI Studio correction	F value/ Kruskal-Wallis chi-squared (*)	p-value
Proximal sphincter	Tract number	Tract number (eddy FSL)	Tract number (eddy DSI)	2.200*	0.333
	Tract length	Tract length (eddy FSL)	Tract length (eddy DSI)	0.362	0.698
	FA	FA (eddy FSL)	FA (eddy DSI)	0.199	0.820
	AD	AD (eddy FSL)	AD (eddy DSI)	1.211*	0.546
	MD	MD (eddy FSL)	MD (eddy DSI)	0.465	0.793
	RD	RD (eddy FSL)	RD (eddy DSI)	0.405	0.669
Distal sphincter	Tract number	Tract number (eddy FSL)	Tract number (eddy DSI)	0.712	0.496
	Tract length	Tract length (eddy FSL)	Tract length (eddy DSI)	1.024*	0.599
	FA	FA (eddy FSL)	FA (eddy DSI)	0.355	0.703
	AD	AD (eddy FSL)	AD (eddy DSI)	0.035	0.965
	MD	MD (eddy FSL)	MD (eddy DSI)	0.221	0.802
	RD	RD (eddy FSL)	RD (eddy DSI)	0.348	0.708
Membranous urethra	Tract number	Tract number (eddy FSL)	Tract number (eddy DSI)	0.673*	0.714
	Tract length	Tract length (eddy FSL)	Tract length (eddy DSI)	1.331*	0.514
	FA	FA (eddy FSL)	FA (eddy DSI)	0.652	0.525
	AD	AD (eddy FSL)	AD (eddy DSI)	1.390*	0.499
	MD	MD (eddy FSL)	MD (eddy DSI)	0.979*	0.613
	RD	RD (eddy FSL)	RD (eddy DSI)	0.806*	0.668

5.3 Fiber tracking results on the original diffusion tensor imaging data

Before creating the .fib file with the fiber tracking information, a .src quality control file was obtained for each analyzed subject. It was observed that, for every single .src file obtained, there was a b-table match and a high neighboring DWI correlation – correlation values ranged from 0.53 and 0.95.

The fiber tracking results for each of the individual structures for the 95 subjects analyzed was concordant with the male urethral complex reported microarchitecture. The microstructure of the proximal and distal sphincters, as well as the membranous urethra is depicted in Figure 5.10 for one of the study subjects arbitrarily chosen. The color map, based on the orientation of the fibers, has the following convention – red for left-right (x), green for anterior-posterior (y) and blue for superior-inferior (z) directions. For the same subject, each of the studied structures of the male urethral complex is shown on three different views (axial, sagittal and coronal), and positioned relatively to the acquired slices, namely, the T2-weighted images (Figure 5.11). On the anatomical images, one can observe the proximal sphincter located between the inferior portion of the bladder (brighter on the image) and the base of the prostate. Moreover, the tracked distal sphincter can be seen between the apex of the prostate to the penile bulb, surrounding the membranous urethra that has the same extension.

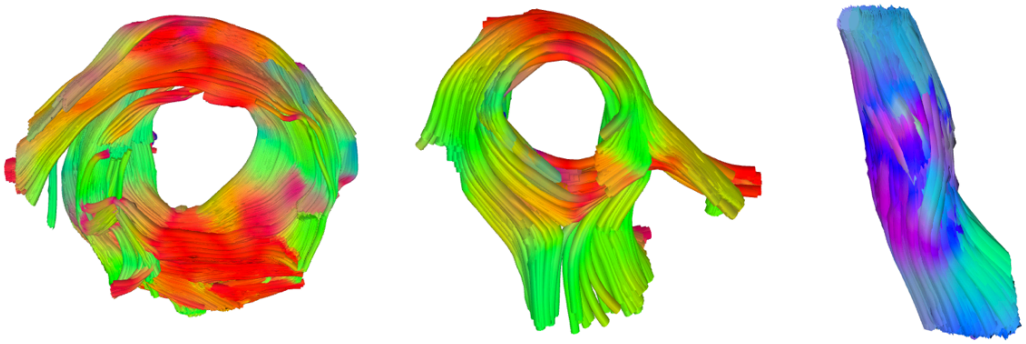

Figure 5.10 Fiber tracking results derived from the DTI images of an arbitrarily chosen study subject, a 61 years old PC patient with a tumor located on the PZ. This figure shows the microstructure of the proximal and distal sphincters and the membranous urethra, color-coded based on the direction of the fibers - red for left-right (x), green for anterior-posterior (y) and blue for superior-inferior (z) directions.

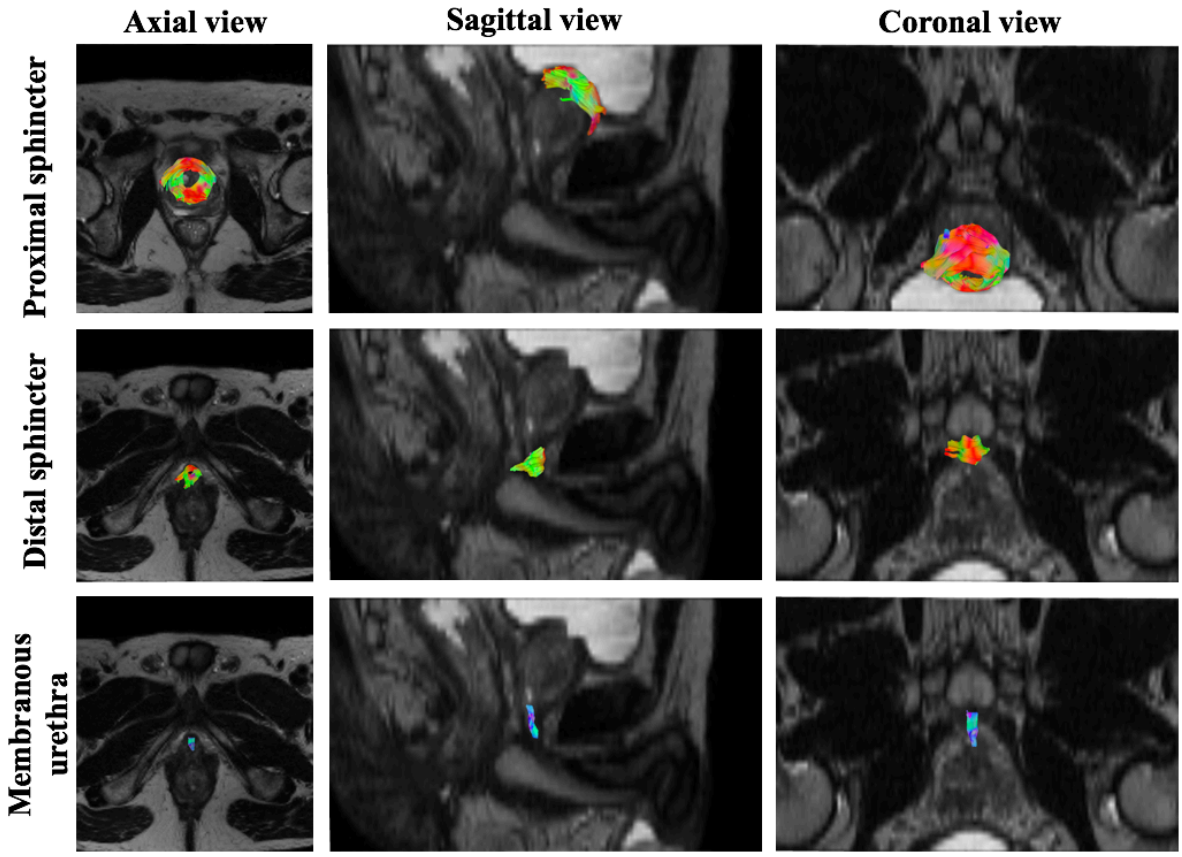

Figure 5.11 Fiber tracking results overlaid on the T2 maps, for one of the study subjects arbitrarily chosen. From top to bottom, respectively, it is represented the proximal sphincter, the distal sphincter and the membranous urethra for this subject. From left to right, respectively, each structure of interest is shown on the axial, sagittal and coronal views.

For each subject involved in this study, fiber tracking performed on the original DTI data allowed to extract a set of DTI metrics – FA, AD, MD, RD, fiber length and fiber density. One subject from each age and disease group was arbitrarily chosen to have their sphincters and membranous urethra represented through color-coded images for each of the DTI metrics analyzed (FA, AD, MD and RD) – Figures 5.12 to 5.17, respectively showing the proximal sphincter, the distal sphincter and the membranous urethra by age group and disease group. The color bar, on the right side of the figures, encodes the intensity of each DTI metric. Whereas regions of the structures with a higher DTI metrics' intensity (set to the maximum value of that metric among subjects) are represented in red, areas with a lower intensity (closer to zero) are represented in blue. In particular, the first row of each figure color-encodes the anisotropy changes within each structure.

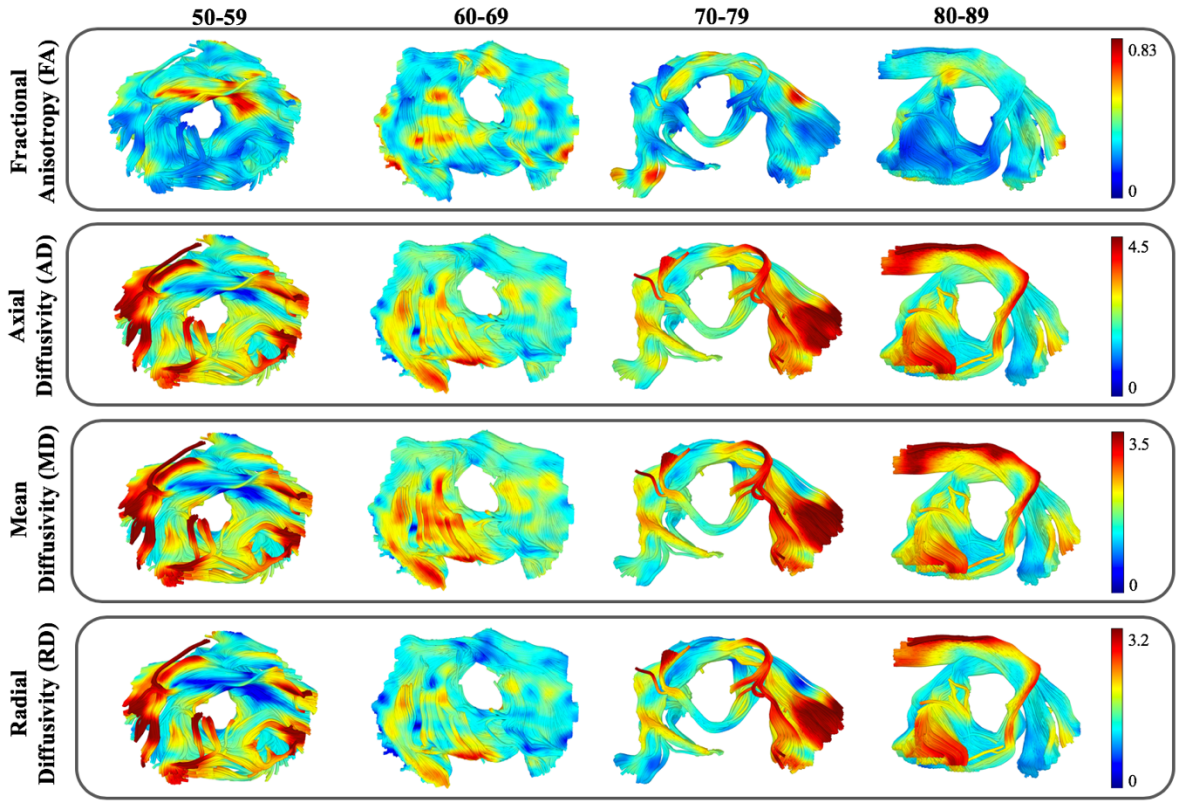

Figure 5.12 Color-encoded DTI metrics (from top to bottom, FA, AD, MD and RD) for the proximal sphincter of four study subjects representative of each age decade. Red depicts regions with a higher DTI metric value, while blue depicts regions with a DTI metric value closer to zero.

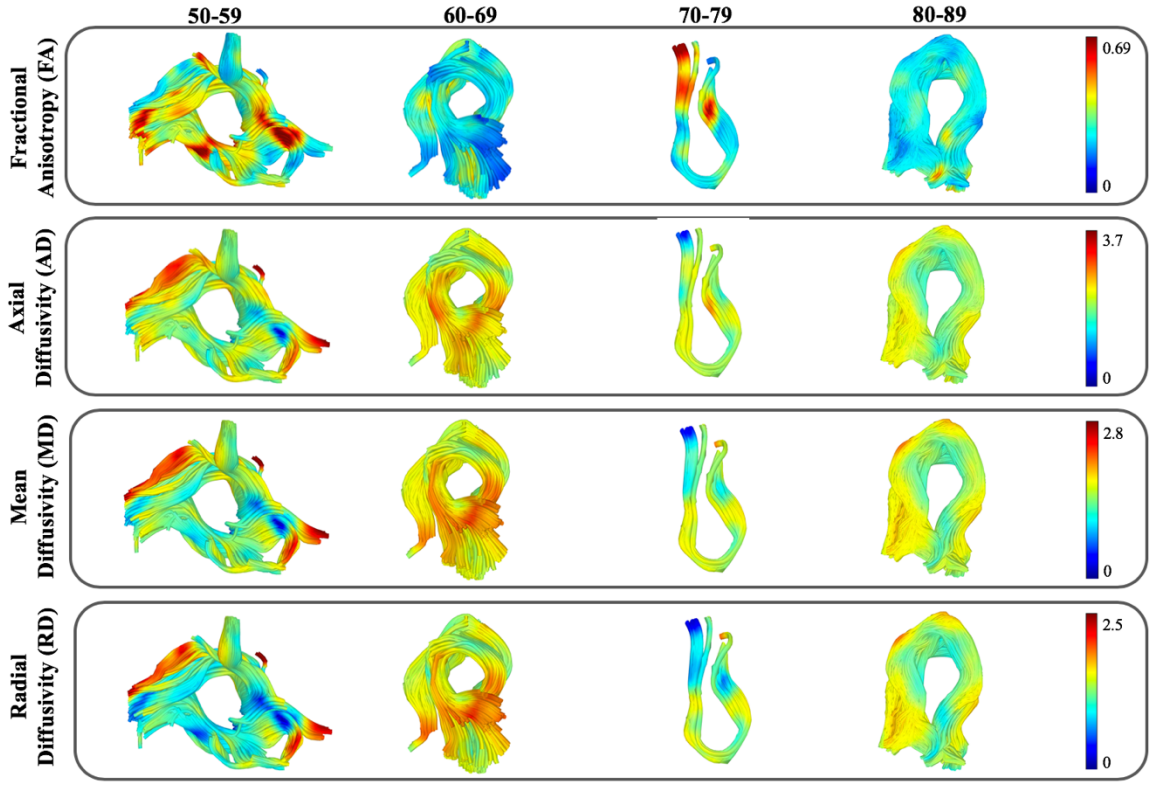

Figure 5.13 Color-encoded DTI metrics (from top to bottom, FA, AD, MD and RD) for the distal sphincter of the same four study subjects chosen for Figure 5.12. Red depicts regions with a higher DTI metric value, while blue depicts regions with a DTI metric value closer to zero.

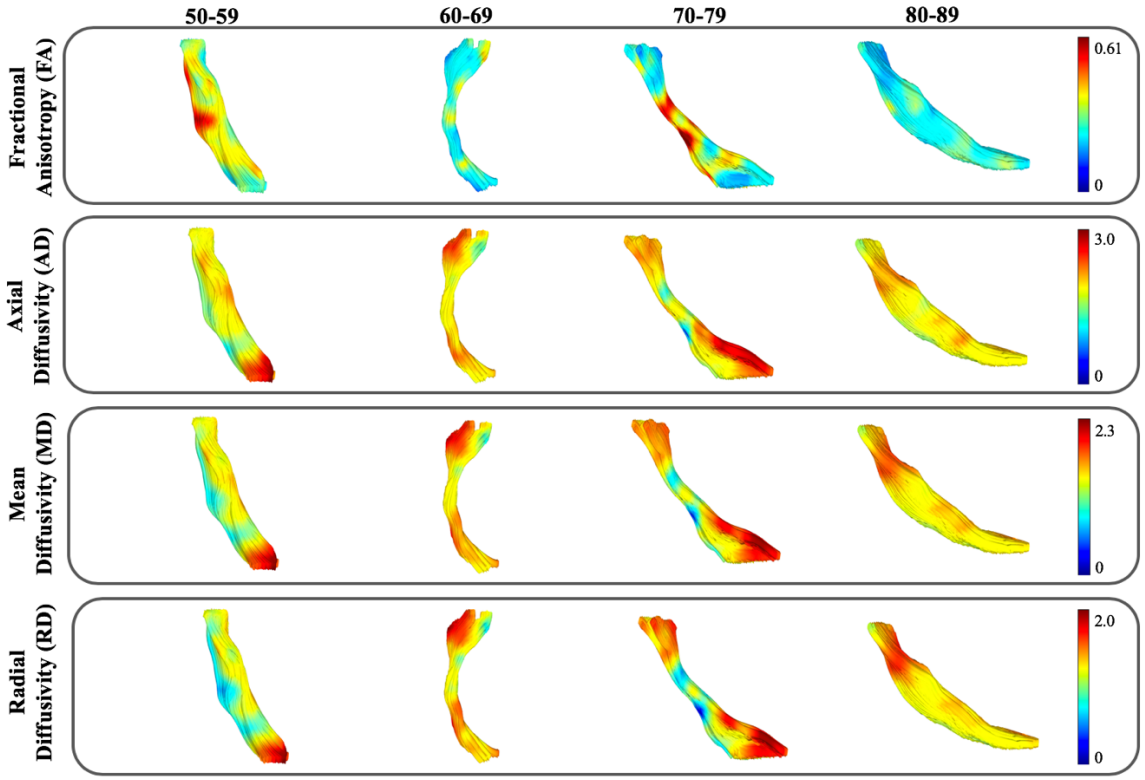

Figure 5.14 Color-encoded DTI metrics (from top to bottom, FA, AD, MD and RD) for the membranous urethra of the same four study subjects chosen for Figure 5.12. Red depicts regions with a higher DTI metric value, while blue depicts regions with a DTI metric value closer to zero.

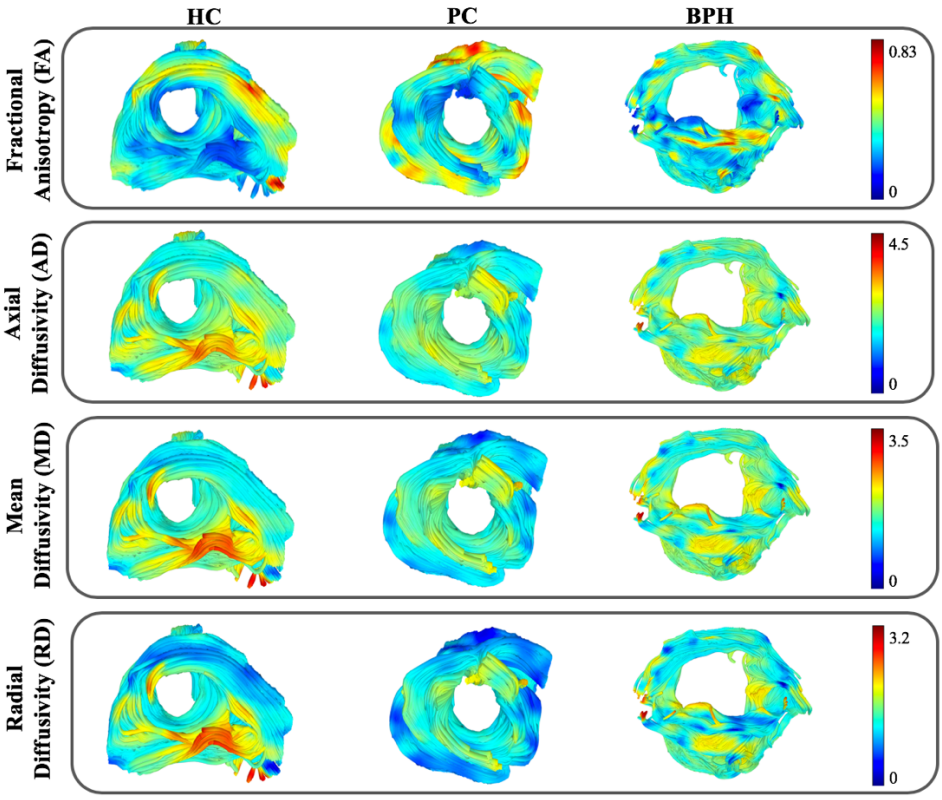

Figure 5.15 Color-encoded DTI metrics (from top to bottom, FA, AD, MD and RD) for the proximal sphincter of three study subjects representative of each disease group –HC, PC subjects and BPH subjects. Red depicts regions with a higher DTI metric value, while blue depicts regions with a DTI metric value closer to zero.

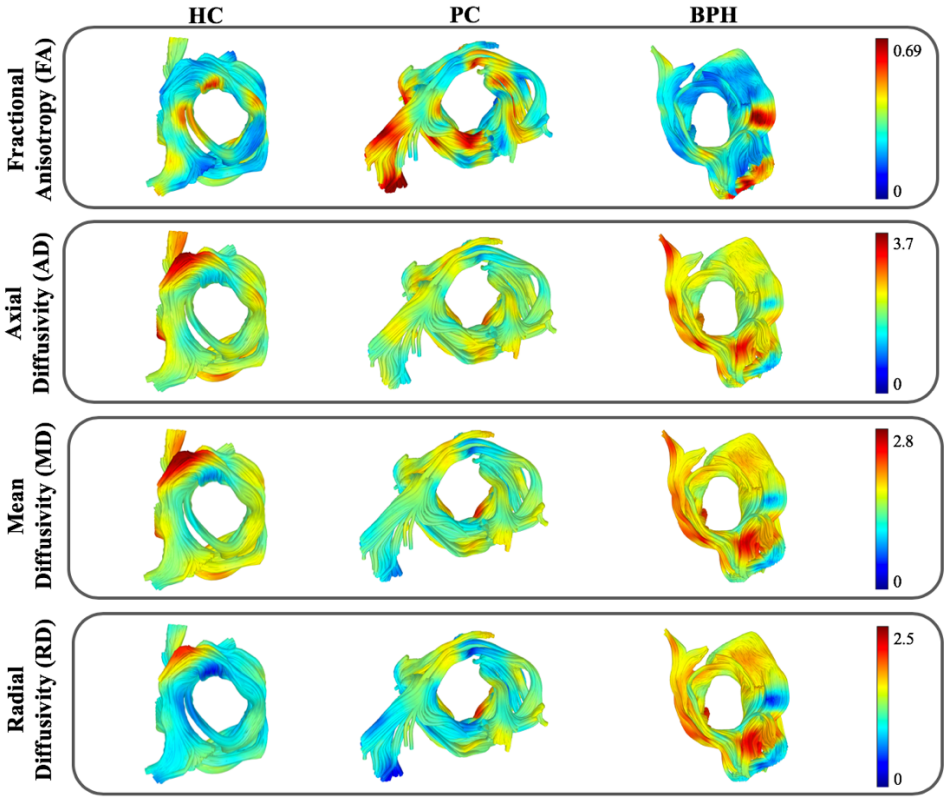

Figure 5.16 Color-encoded DTI metrics (from top to bottom, FA, AD, MD and RD) for the distal sphincter of the same three study subjects chosen for Figure 5.15. Red depicts regions with a higher DTI metric value, while blue depicts regions with a DTI metric value closer to zero.

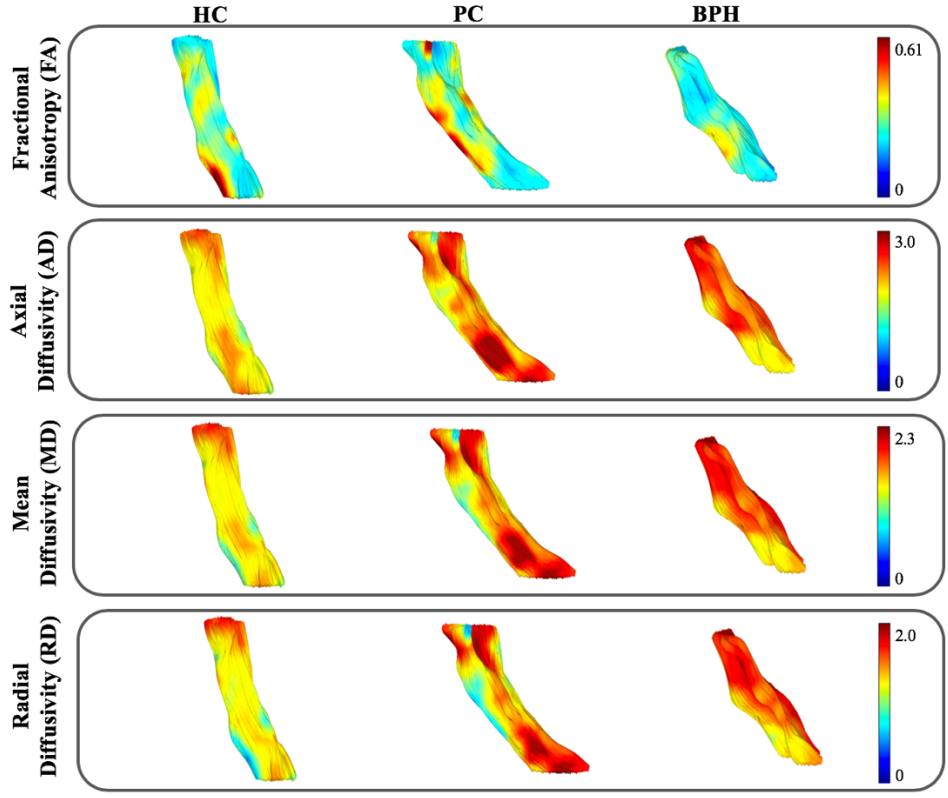

Figure 5.17 Color-encoded DTI metrics (from top to bottom, FA, AD, MD and RD) for the membranous urethra of the same three study subjects chosen for Figure 5.15. Red depicts regions with a higher DTI metric value, while blue depicts regions with a DTI metric value closer to zero.

The mean and standard deviation of the DTI metrics for the 95 study subjects, obtained both for the proximal and distal sphincters, as well as for the membranous urethra, are summarized in Table 5.4. The remaining 14 histogram metrics of each DTI index are shown in the Appendix Table A.

Table 5.4 Mean and standard deviation (mean ± sd) values on the DTI metrics of the 95 male study subjects, for each analyzed structure of the urethral complex. Tract density is expressed in tracts/mm^3; Tract length in millimeters (mm); Diffusivity measures - AD, MD and RD - in 10^{-3} mm^2/s; FA is dimensionless.

	Proximal sphincter	**Distal sphincter**	**Membranous urethra**
FA	0.36 ± 0.04	0.32 ± 0.04	0.33 ± 0.05
AD	2.18 ± 0.18	2.11 ± 0.21	2.13 ± 0.39
MD	1.59 ± 0.16	1.60 ± 0.19	1.58 ± 0.32
RD	1.30 ± 0.16	1.35 ± 0.18	1.30 ± 0.29
Tract density	1.25 ± 0.85	0.33 ± 0.30	9.98 ± 10.4
Tract length	85.4 ± 19.1	53.3 ± 8.89	26.2 ± 7.47

5.4 Inferential statistics on diffusion tensor imaging metrics with age

The statistical results on Pearson correlations (or Spearman correlations) between age and each of the DTI metrics analyzed, for the total dataset of 95 subjects, are presented in Table 5.5 and 5.6. Whereas the latter shows the results for the correlations between tract length and tract density with age, the former shows the results for the correlations between each DTI metric - FA, AD, MD and RD (mean values and the remaining 14 histogram metrics) - with age. These tables present the correlation coefficients (r for Pearson and r_S for Spearman) between each pair, where the statistically significant correlation p-values are highlighted in color (as described by the caption in Figure 5.18).

Similarly, Table 5.7 and 5.8 shows the linear regressions' adjusted R-squared of the relationship between age and each DTI metric, color-coded by the p-value on the linear regression statistical significance.

0.01 < p-value < 0.05	p-value < 0.01

Figure 5.18 Color scheme for the statistically significant p-values.

*Table 5.5 Pearson or Spearman (marked with an *) correlation coefficients (r or r_S) between age and each of the DTI metrics (FA, AD, MD and RD) mean, standard deviation (sd), median, trimmed mean, median absolute deviation (mad), minimum, maximum, range, skewness, kurtosis, standard error (se), and the 5th, 25th, 75th and 95th percentiles values, calculated for the male urethral complex structures studied. Statistically significant correlation p-values are color-coded, as shown by Figure 5.18.*

Age as independent variable	Proximal sphincter				Distal sphincter				Membranous urethra			
	FA	AD	MD	RD	FA	AD	MD	RD	FA	AD	MD	RD
Mean	-0.174	0.171	0.206	0.225	0.363	0.301*	0.301*	0.335*	0.506	0.165*	0.375*	0.966*
Standard deviation (sd)	0.009	0.172*	0.233	0.227	-0.091	-0.003*	0.007*	-0.023	0.041	0.238	0.283	0.269
Median	-0.211	0.091	0.149	0.168	-0.095	0.173*	0.169*	0.175*	0.052	0.116*	0.060*	0.069*
Trimmed mean	-0.189	0.144	0.198	0.216	-0.094	0.151*	0.146*	0.133*	0.071	0.135*	0.080*	0.069*
Median absolute deviation (mad)	-0.029	0.201*	0.256	0.225	-0.175	-0.010*	0.113*	0.062	0.036	0.226	0.275*	0.252
Minimum	-0.273*	-0.186*	-0.176*	-0.153*	0.097*	-0.004*	0.018*	0.033*	0.089*	0.088*	0.011*	-0.003
Maximum	0.108*	-0.041	-0.114	-0.130	-0.059*	-0.129	-0.211*	-0.197	-0.011*	0.173*	0.174*	0.128
Range	0.179*	0.044*	-0.040	-0.049*	-0.059*	-0.114	-0.201	-0.210	-0.020*	0.156	0.148	0.133
Skewness	0.148*	-0.076*	-0.181	-0.166	-0.034*	-0.100	-0.210*	-0.170	-0.052*	0.057*	0.063*	0.033*
Kurtosis	0.117*	-0.204*	-0.296*	-0.291*	-0.016*	-0.068*	-0.191*	-0.191*	-0.060*	-0.110*	-0.159*	-0.196*
Standard error (se)	-0.019*	0.066*	0.063*	0.056*	0.072*	0.098	0.100	0.102	0.180*	0.285*	0.289*	0.276*
5th percentile (Q0.05)	-0.237	-0.013*	0.023*	0.061*	-0.042*	0.168*	0.102	0.082	0.013	0.057*	-0.036*	-0.043
25th percentile (Q0.25)	-0.220	0.020	0.078	0.117	-0.063	0.212*	0.136	0.130	0.070	0.054*	0.034*	0.036*
75th percentile (Q0.75)	-0.148	0.226*	0.285	0.278*	-0.116	0.135*	0.150*	0.134*	0.081	0.186*	0.142*	0.116*
95th percentile (Q0.95)	-0.077	0.297*	0.268*	0.260*	-0.085	0.012*	0.007*	-0.011*	0.064	0.176*	0.219*	0.205*

*Table 5.6 Pearson or Spearman (marked with an *) correlation coefficients (r or r_S) between age and each of the DTI metrics tract length and tract density, calculated for the male urethral complex structures studied. Statistically significant correlation p-values are color-coded, as shown by Figure 5.18.*

Age as independent variable	Proximal sphincter		Distal sphincter		Membranous urethra	
	Tract length	Tract density	Tract length	Tract density	Tract length	Tract density
	-0.0008	-0.062*	-0.187	-0.121*	-0.139*	-0.142*

Table 5.7 Adjusted R-squared values on the linear regressions performed between age and each of the DTI metrics (FA, AD, MD and RD) mean, standard deviation (sd), median, trimmed mean, median absolute deviation (mad), minimum, maximum, range, skewness, kurtosis, standard error (se), and the 5th, 25th, 75th and 95th percentiles values, calculated for the male urethral complex structures studied. Statistically significant correlation linear regressions are color-coded, as shown by Figure 5.18.

Age as independent variable	Proximal sphincter				Distal sphincter				Membranous urethra			
	FA	AD	MD	RD	FA	AD	MD	RD	FA	AD	MD	RD
Mean	0.020	0.019	0.032	0.040	-0.002	0.001	0.003	0.004	-0.006	0.002	-0.001	-0.010
Standard deviation (sd)	-0.011	0.036	0.044	0.041	-0.002	-0.010	-0.010	-0.010	-0.009	0.047	0.070	0.063
Median	0.034	-0.002	0.012	0.018	-0.002	0.009	0.012	0.014	-0.008	-0.003	-0.004	-0.003
Trimmed mean	0.025	0.010	0.029	0.036	-0.002	0.006	0.010	0.010	-0.006	0.001	-0.001	-0.004
Median absolute deviation (mad)	-0.010	0.043	0.055	0.041	0.020	-0.011	-0.004	-0.007	-0.009	0.041	0.066	0.053
Minimum	0.065	0.017	0.012	0.000	-0.009	-0.011	-0.009	-0.007	-0.007	-0.010	-0.010	-0.011
Maximum	-0.008	-0.009	0.002	0.006	0.006	0.006	0.030	0.029	-0.011	0.012	0.011	0.006
Range	-0.002	-0.010	-0.009	-0.003	0.008	0.002	0.030	0.034	-0.011	0.014	0.011	0.007
Skewness	0.021	-0.001	0.023	0.017	-0.011	-0.001	0.020	0.018	-0.006	-0.005	-0.007	-0.010
Kurtosis	0.007	0.064	0.134	0.124	-0.008	-0.004	0.017	0.015	-0.005	-0.011	-0.008	-0.005
Standard error (se)	-0.011	-0.002	0.000	-0.002	-0.003	-0.001	-0.001	0.000	0.010	0.043	0.045	0.039
5th percentile (Q0.05)	0.046	-0.005	-0.006	-0.010	-0.006	0.009	-0.001	-0.004	-0.011	-0.010	-0.009	-0.009
25th percentile (Q0.25)	0.038	-0.010	-0.005	0.003	-0.007	0.014	0.008	0.006	-0.006	-0.007	-0.009	-0.010
75th percentile (Q0.75)	0.011	0.045	0.071	0.076	0.003	0.001	0.011	0.009	-0.004	0.012	0.010	0.005
95th percentile (Q0.95)	-0.005	0.082	0.083	0.081	-0.003	-0.011	-0.010	-0.010	-0.007	0.015	0.024	0.022

Table 5.8 Adjusted R-squared values on the linear regressions performed between age and each of the DTI metrics tract length and tract density, calculated for the male urethral complex structures studied. Statistically significant correlation p-values are color-coded, as shown by Figure 5.18.

Age as independent variable	Proximal sphincter		Distal sphincter		Membranous urethra	
	Tract length	Tract density	Tract length	Tract density	Tract length	Tract density
	-0.0107	-0.0061	0.0283	0.0004	0.0059	0.0063

5.5 Inferential statistics on diffusion tensor imaging metrics by group

ANOVA (or the non-parametric Kruskal-Wallis, marked with an *) statistical test results on the comparison of DTI metrics between the four age groups are presented in Appendix Table B. For each of the studied structures of the male urethral complex, DTI metrics that have shown statistically significant ANOVA test results were graphically represented using boxplots (Figures 5.19 to 5.21). On those boxplots is also shown the respective post-hoc t-test results to identify the age decades between which the difference has occurred.

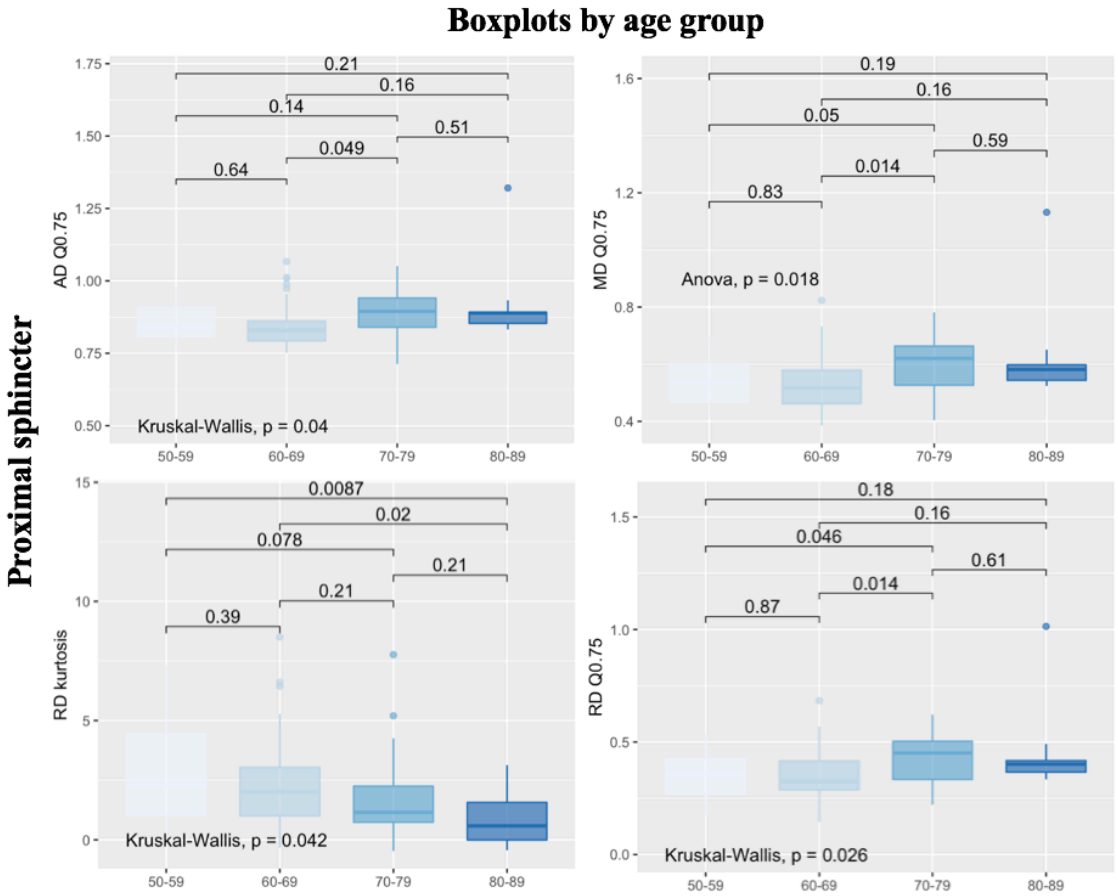

Figure 5.19 Boxplots representing statistically significant ANOVA (or the non-parametric Kruskal-Wallis) test results on DTI metrics of the proximal sphincter between age groups. Post-hoc t-test p-values for each pair of age decades is on the top of each figure.

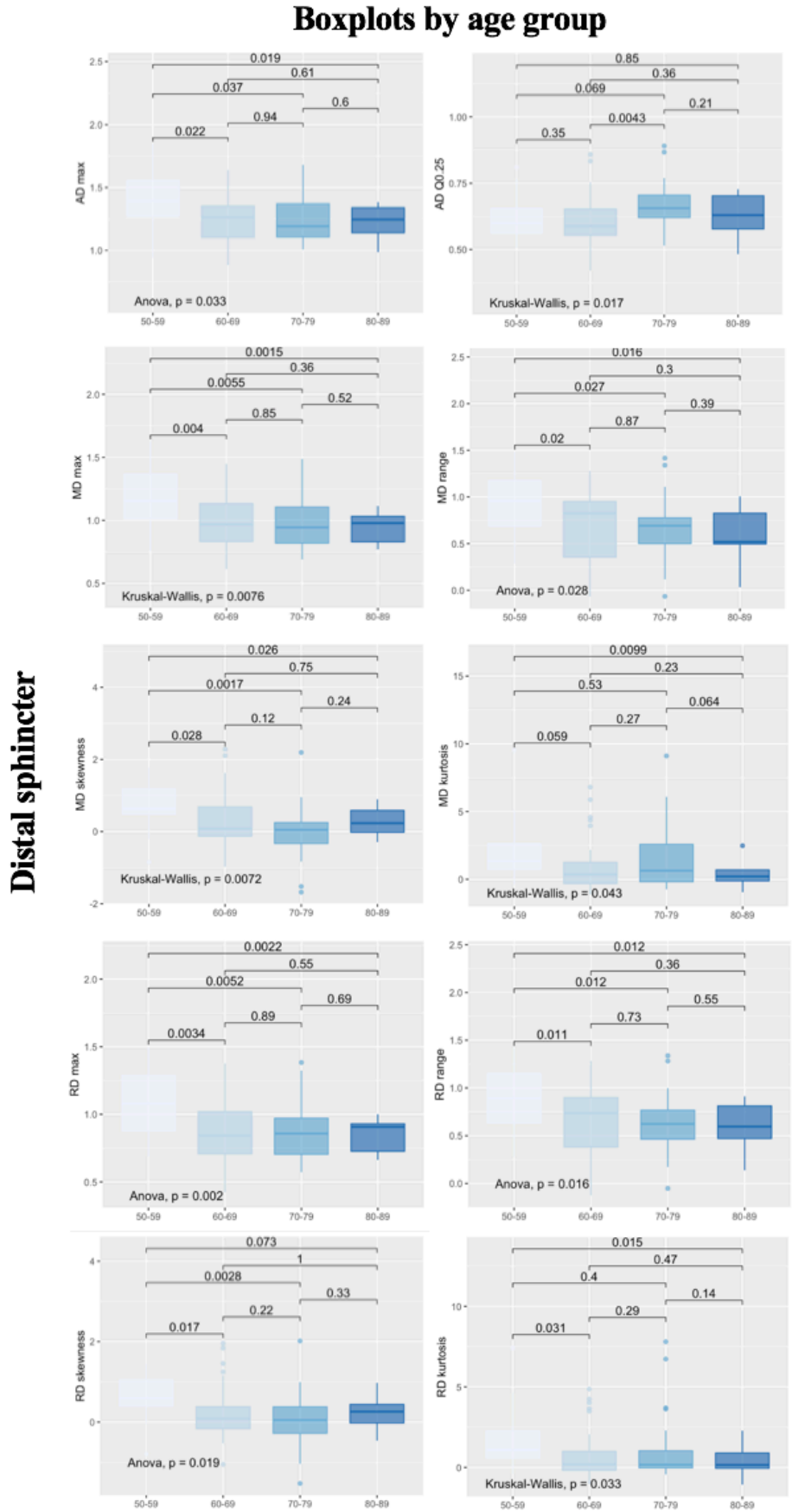

Figure 5.20 Boxplots representing statistically significant ANOVA (or the non-parametric Kruskal-Wallis) test results on DTI metrics of the distal sphincter between age groups. Post-hoc t-test p-values for each pair of age decades is on the top of each figure.

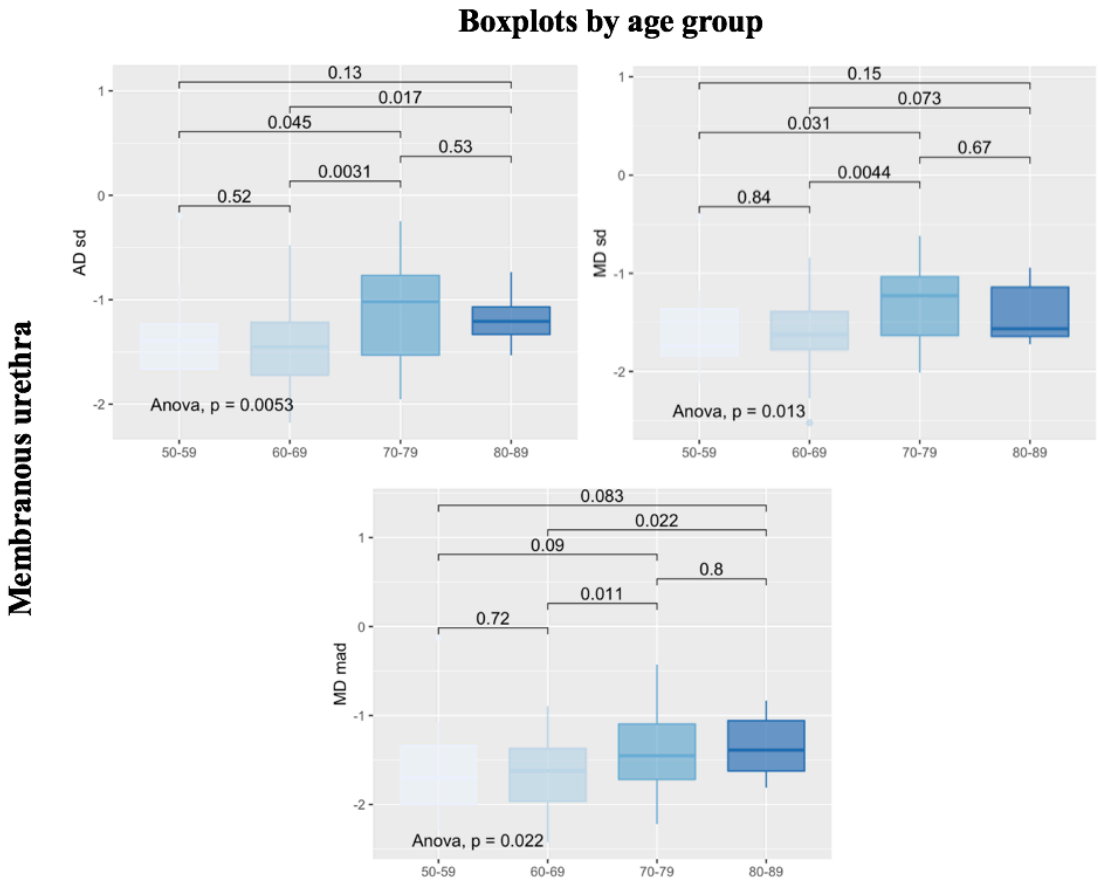

Figure 5.21 Boxplots representing statistically significant ANOVA (or the non-parametric Kruskal-Wallis) test results on DTI metrics of the membranous urethra between age groups. Post-hoc t-test p-values for each pair of age decades is on the top of each figure.

For the subset of the 69 diagnosed patients with PC, BPH or with a negative diagnosis for a prostate condition – the HC group –, ANOVA (or the non-parametric Kruskal-Wallis, marked with an *) statistical test results for the comparison between disease groups are represented in Appendix Table B. For visually describing how each DTI metric differed between disease groups, boxplots were presented in Figure 5.22. Those boxplots were created for the variables that significantly changed between groups, where ANOVA (or Kruskal-Wallis) and post-hoc t-test p-values were included.

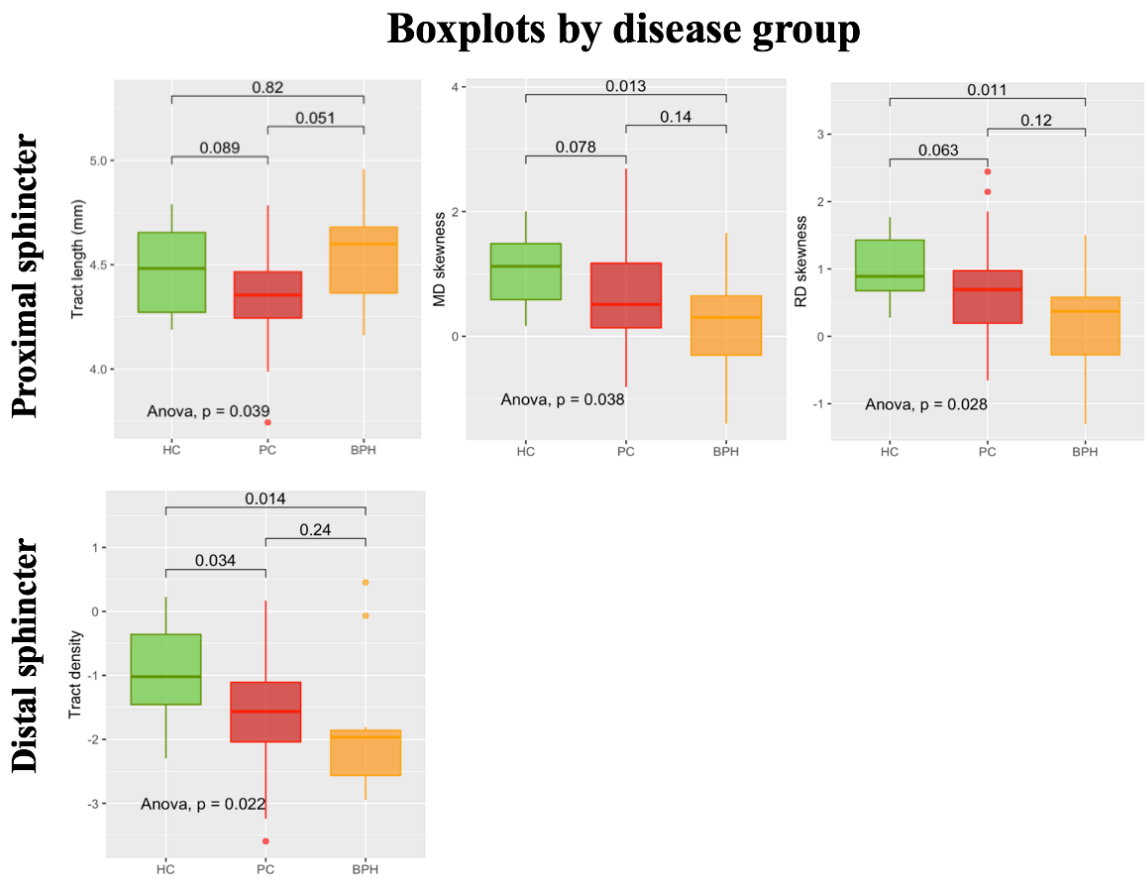

Figure 5.22 Boxplots of statistically significant ANOVA (or Kruskal-Wallis) comparisons of DTI metrics between disease groups. Here the PC group is represented in red, the BPH in orange and the HC group in green. Post-hoc t-test p-values for each pair of disease groups is on the top of each figure.

Afterwards, statistical t-test results (or the non-parametric Mann-Whitney, marked with an *) are presented in Appendix Table B, for identifying whether each of the DTI metrics varied with statistically significance with cancer status, meaning between patients with and without PC. Boxplots of statistically significant t-test comparisons are depicted in Figure 5.23.

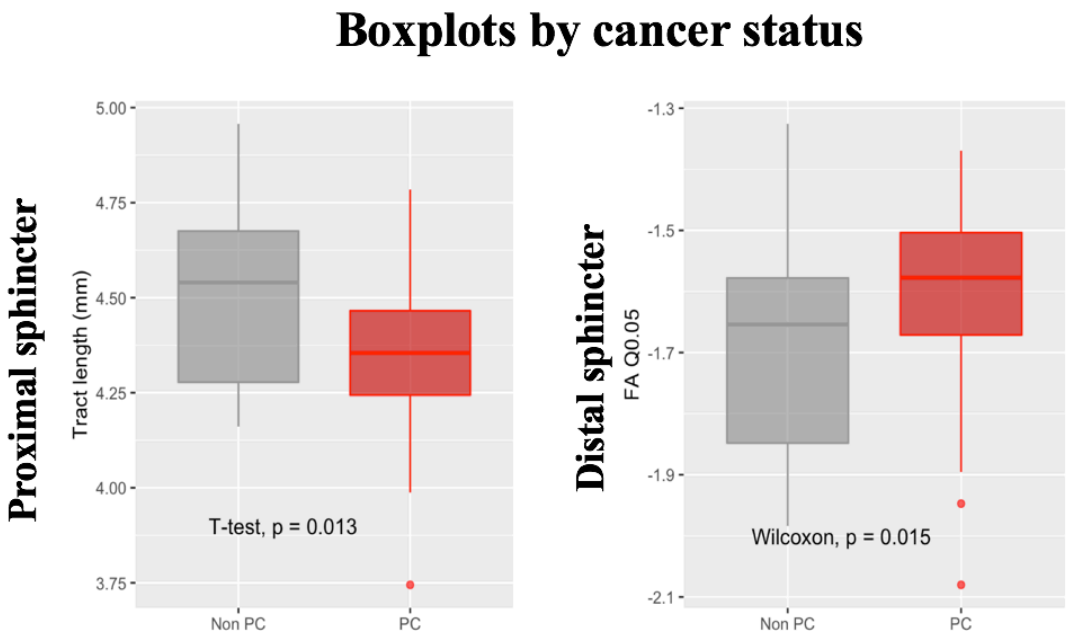

Figure 5.23 Boxplots of statistically significant t-test comparisons of DTI metrics between cancer status groups. Here the PC group is represented in red, whereas the non-PC group is shown in grey.

6 DISCUSSION

With an evolving ageing population, there is an increasing risk for several complications, including prostate conditions in men. These conditions comprise BPH and PC. PC is the most incident cancer among male subjects in developed countries [5], and different treatment options are available according to tumor stratification and individual patient preferences. For locally advanced tumors, the RP has proven to be the most accurate treatment option in tumor removal, with a longer life expectancy. Despite recent innovative advances in RP, including new robotic systems and sparing surgical techniques, the rate of post-surgical outcomes is still a major drawback that makes patients avoid surgery. Particularly, urinary incontinence is a limiting quality of life outcome that affects a significant proportion of patients that undergo surgery [1]. The male urethral complex has shown to play a determining role in maintaining urinary continence, and the post-surgical incontinence is mostly related with the removal of the proximal sphincter concomitant with prostate removal [41].

Using diffusion tensor imaging (DTI) – an MRI-based technique that studies the fiber arrangements based on the diffusivity of water molecules – to extract a set of metrics of the proximal and distal sphincters and of the membranous urethra, can reveal its microstructure [3]. Studying how DTI metrics – including FA, AD, MD, RD, tract length and tract density – of the male urethral sphincter complex change with increasing age, can reveal relevant information for a future prediction of the urinary incontinence recovery rate in operated older male.

To our knowledge, the current study was the first to investigate age-related differences in the male urethral sphincter. In this investigation, some acquisition and processing steps on DTI of the male urethral sphincter complex were optimized and different aspects were analyzed during this study, including the acquisition parameters, fiber tracking parameters and eddy currents and motion corrections.

Optimization of diffusion tensor imaging acquisition parameters for the male urethral sphincter

There is no stablished consensus on the optimal DTI acquisition parameters – it is dependable on several factors, including hardware configuration, field strength, vendor, scanning time compatible with the clinical practice, and the anatomic structure to be studied [14]. Additionally, it was the first time that a DTI sequence was included on the mpMRI of the prostate acquired at CCU. Firstly, a MRI scanner with a field strength of 3T was chosen over 1.5T, because the former represents a twofold increase in the SNR comparing with the latter, which results in a better spatial and temporal resolution [118]. Secondly, in order to define the acquisition parameters that yielded good fiber tracking results for the urethral sphincter, a set of different parameters – including the number of gradient directions, the number of slices and the b-value – have been tested. Specifically, from case 001' to case 002', the number of slices was decreased from 25 to 20 in order to minimize acquisition duration, because of time constraints imposed by the clinicians. Although in the brain, recommended b-values are in the order of 1000 s/mm^2 [47], reported b-values on DTI studies of the prostate are lower, and around 700 s/mm^2 [92]. In fact, since the prostate has a lower number of fibers comparing with the brain, a higher b-value may not allow an accurate definition of the sphincter structure. So, from case 002' to 001 we've made the decision to decrease the b-value from 800 to 600 s/mm^2, which allowed a better image resolution. And so, it was possible to increase the number of slices while maintaining acquisition duration. From case 001 to 002, all parameters were kept constant, but the acquisition extension has been displaced to a more distal region, since for this patient's tracking, it was only possible to delineate half of the distal sphincter.

Finally, it was found that a decrease on the number of diffusion encoding directions from 33 to 16 (Case 003) did not significantly decreased the accuracy on fiber tracking. So, it was simultaneously possible to increase the number of acquired slices, while maintaining the in-plane resolution and decreasing the acquisition duration. So, it was considered that a DTI sequence with a b-value of 600 s/mm^2, 16 diffusion gradient directions and 40 acquired slices represented the best compromise between acquisition duration and in-plane resolution.

Image quality control, regions of interest definition and the choice of fiber tracking parameters

Before fiber tracking, a manual inspection of the individual .src quality control files has shown high neighboring DWI correlation values – between 0.53 and 0.95 – which attests to the image quality. Since on the contrary, lower correlation values are suggestive of subject motion and other SNR issues [4]. Additionally, it was chosen a manual definition of the ROIs to track the sphincters and the membranous urethra, instead of an automated approach. For segmenting white-matter of the brain, "virtual dissection" – combinations of inclusion and exclusion regions of interest are manually defined on the images in order to obtain the fiber tracts – have been replaced by more reproducible and less time-consuming automatic approaches [119]. These are comprised by ROI-based, clustering-based and direct segmentations, that mostly rely on the comparison with a WM brain atlas. However, the creation of a prostate atlas that results on the alignment of all subjects' glands would present unfeasible anatomical results due to the high variability between subjects – namely, subjects under study have very different prostate volumes and different status of full/empty bladder –, and the ROIs to track the sphincters in this atlas would not match the correct position of the sphincter for each individual subject.

Regarding termination criteria, that includes FA threshold and angular threshold, these were chosen by following a trial-and-error approach using as starting point the values stablished by Sinha et al. 2018 [3]. A FA threshold of 0.15 was chosen, since lower values caused fibers to be tracked outside the structures of interest, whereas higher values restrained too much the tracked fibers. For some subjects, lower FA thresholds of 0.10 or 0.05 were used in order to include the fibers that are part of the structures. Angular threshold defines the maximum crossing angle between consecutive moving directions, above which the tracking is terminated. A higher angular threshold (75°) was chosen for the sphincters comparing with the membranous urethra (45°), because they represent ring-like structures, that have a higher angulation comparing with straight structures like the membranous urethra. Concerning the remaining fiber tracking parameters, the step size represents a moving distance of 0.69 mm in each tracking interval, and with a smoothing of 0.09, meaning that each moving direction remains 9% of the previous propagation vector, or "momentum" [4]. The length of the tracked streamlines was limited to the range of 50 to 200 mm, so that spurious shorter fibers as well as long irrelevant fibers are eliminated. An "all" seed orientation was chosen over a "primary" seed orientation to start the tracking for each fiber orientation within a voxel, and not only for the most prominent fiber. Furthermore, a "subvoxel" seed position was chosen over a "voxel" to place unlimited seeds within the voxel, and not only in its center. The default deterministic algorithm was chosen for the tracking, with a trilinear direction interpolation, since as shown to yield better results than a fourth order Runge-Kutta method. A multithread approach (4 threads) was used according to the available computation power, to optimize the tracking performance. For determining the tracking termination, seed number was redefined instead of tract number, because it was expected to give the tracts some freedom and to set their number based on seeds.

The effect of the subject motion and eddy currents corrections on fiber tracking results

Subject motion and eddy currents corrections of prostate diffusion tensor images were not performed in most existing studies [17], [92], [96], [99]. Despite the inexistence of indications on whether these corrections should be performed, the DTI study on the male urethral complex [3] has included some processing steps to perform them. In general, the combination of retrospective and prospective methods has proven to be the most reliable option to correct for patient movement – in combination with EPI distortion and eddy currents correction [68]. A prospective method alters the DTI sequence to include real-time motion correction. The real-time motion correction was performed on 17 of the study subjects, by an alignment of the diffusion volumes with the b0 using an affine transformation. On the other hand, a retrospective correction method is the one that implements several processing steps after the data was acquired. For the eddy currents correction, two different methods were used – the combination of "topup" with "eddy" from FSL and the DSI Studio eddy/motion correction. Since "topup" requires at least two b0 volumes with opposite PE directions it was only possible to calculate the susceptibility distortions for the subset of 17 subjects with a PA acquisition. Analyzing the DTI metrics of the sphincters and membranous urethra for this subset of patients, it was found no statistically significant differences with and without correction. The lack of statistical significance was found both for subject motion and eddy currents corrections, which leads to the conclusion that there is no need for correcting these images in order to get accurate fiber tracking results for the male urethral sphincter.

Investigating age-related differences on diffusion tensor imaging metrics of the male urethral complex

Answering the main research question of this thesis, it was found that for the 95 study subjects analyzed, some DTI metrics significantly changed with age. In particular, when correlating each one of the studied DTI metrics with age, MD and RD in the proximal sphincter seemed to be positively correlated with age. However, since the visual inspection of fiber tracking results has shown local variations in the DTI metrics, metrics that explain its distribution along the structure were included. In fact, when analyzing other histogram metrics apart from the standard mean DTI metric values, many of these have shown to be significantly correlated with age. In particular, for the proximal sphincter, FA minimum, MD and RD kurtosis, MD and RD 75^{th} percentiles and AD and MD 95^{th} percentiles, as well as MD and RD standard deviations, MD absolute deviation and AD, MD and RD standard errors, for the membranous urethra were statistically significant correlated with age. For the distal sphincter, fewer DTI metrics were correlated with age, including, for instance, MD maximum, MD skewness, RD range and AD 25^{th} percentile. The identified statistically significant linear regressions showed a high agreement with the significant correlations found. It is safe to assume that the DTI metrics MD and RD – including its mean value and other histogram metrics, specially standard error (se), median absolute deviation (mad), kurtosis, standard error (se) and 75^{th} and 95^{th} percentiles – are better correlated with age, and the analysis of these metrics distributions can lead to the understanding of the male urethral sphincter microstructure with age.

When dividing patients according to their age, it was found that, although DTI metrics' mean values did not significantly change between age groups, some histogram metrics – including maximum value, kurtosis and the 75^{th} percentile – have recurrently differed between age groups, particularly MD and RD. Specifically, most of the changes were identified between those aged 50-59 with 70-79, and 50-59 with 80-89 years old. For example, RD kurtosis in the distal sphincter is significantly decreased in the 80-year-olds when comparing with the 50-year-olds. This means that RD has a more flattened distribution in older subjects, with a similar distribution of diffusion among the distal sphincter.

In conclusion, MD and RD distributions significantly changed with age. For instance, with increasing age, the RD kurtosis in the proximal sphincter has a more flattened distribution, the MD maximum value in the distal sphincter is decreased, and the MD values are highly deviated from its median in the membranous urethra. Accordingly, some of these histogram metrics might be used as biomarkers of the male urethral complex to differentiate subjects by age.

The effect of a prostate condition on diffusion tensor imaging metrics of the male urethral complex

Moreover, hypothesizing that the presence of a prostate condition could affect the DTI metrics, it was studied how each of them changed in PC, BPH and HC subjects. Among PC patients, it was assumed that the location of the tumor does not compromise the DTI fiber tracking results. When dividing patients in two groups by cancer status (with and without PC), statistically significant differences were found, for the proximal sphincter, in tract length and in the 5% percentile of FA distribution. Moreover, when dividing patients in three disease groups it was found, for the proximal sphincter, that most differences in DTI metrics lied within the BPH group. More specifically, tract length was significantly increased in patients with BPH comparing with those with PC, and MD skewness and RD skewness were significantly decreased in subjects with BPH comparing with the HC. Also, HC could be differentiated from the other two groups for having a significantly increased tract density in the distal sphincter.

Limitations and future work

Although statistically significant differences were found in some DTI metrics of the proximal sphincter, distal sphincter and membranous urethra, further investigations are needed to prove if the presence of a prostate condition has influence in those metrics. In fact, one of the main limitations of this study was the heterogeneity of the population in terms of disease conditions – some patients have more aggressive cancers that others, most older males have some degree of prostatic hyperplasia (even when not diagnosed) and almost all HC have negative biopsies despite being in active surveillance for PC. Other limitation relies on the small structure size of the urethral sphincter, that may be corrupted by partial volume effects. Additionally, there were no subjects with a prostate MR for PC diagnosis with less than 45 years old during the study period.

However, the subjects analyzed in this study reflect the reality of everyday clinical practice. There is an increasing chance in developing any type prostate condition with increasing age. In fact, having more than 60 years old is a strong predictor for BPH [120], and represents an incidence of 77.6% of subjects that have PC [28]. So, more than using DTI for studying how the sphincter is structured in young healthy subjects, it is important to study its microstructure on real prospective patients.

Since the inclusion of an additional DTI sequence to the standard mpMRI, only 14 patients of the 45 study subjects with PC, were submitted to a RALRP using the newly approved TransDouglas surgical technique. Additionally, attending to the reduced time span from the initial acquisitions, most of these subjects haven't yet answered the 6-months, or even the 3-months, post-surgical questionnaires. As a consequence, it is not possible to make a prediction on the post-surgical urinary continence time recovery with such short number of patients. After having a larger dataset of operated patients, it is of interest to correlate the post-surgical test scores with the pre-operative T2-weighted MRI parameters and DTI metrics, that reflect the sphincters function and microstructure. In the future, we hope to be able to extract these biomarkers for each patient's urethral sphincter complex and use them as a predictor

on the rate of post-surgical incontinence. However, it is important that this model takes into account the changes in DTI metrics of the male urethral complex that are influenced by ageing. This predictive model may guide patients in an informed choice of the best personalized treatment option to treat their prostate tumor, and to simultaneously provide a satisfying quality of life.

REFERENCES

[1] K. D. Radadia, N. J. Farber, B. Shinder, C. F. Polotti, L. J. Milas, and H. S. G. R. Tunuguntla, "Management of Postradical Prostatectomy Urinary Incontinence: A Review," *Urology*, vol. 113, pp. 13–19, 2018.

[2] P. Hammerer, U. Michl, W.-H. Meyer-Moldenhauer, and H. Huland, "Urethral Closure Pressure Changes with Age in Men," *J. Urol.*, vol. 156, no. 5, pp. 1741–1743, Nov. 1996.

[3] S. Sinha, U. Sinha, V. Malis, V. Bhargava, K. Sakamoto, and M. Rajasekaran, "Exploration of male urethral sphincter complex using diffusion tensor imaging (DTI)-based fiber-tracking," *J. Magn. Reson. Imaging*, vol. 48, no. 4, pp. 1002–1011, Oct. 2018.

[4] F. C. Yeh, T. D. Verstynen, Y. Wang, J. C. Fernández-Miranda, and W. Y. I. Tseng, "Deterministic diffusion fiber tracking improved by quantitative anisotropy," *PLoS One*, vol. 8, no. 11, pp. 1–16, 2013.

[5] C. Fitzmaurice *et al.*, "Global, Regional, and National Cancer Incidence, Mortality, Years of Life Lost, Years Lived With Disability, and Disability-Adjusted Life-Years for 29 Cancer Groups, 1990 to 2016," *JAMA Oncol.*, vol. 4, no. 11, pp. 1553–1568, 2018.

[6] M. S. Litwin and H.-J. Tan, "The diagnosis and treatment of prostate cancer: A review," *JAMA - J. Am. Med. Assoc.*, vol. 317, no. 24, pp. 2532–2542, 2017.

[7] V. Di Paola, A. Cybulski, S. Belluardo, F. Cavicchioli, R. Manfredi, and R. Pozzi Mucelli, "Evaluation of periprostatic neurovascular fibers before and after radical prostatectomy by means of 1.5 T MRI diffusion tensor imaging," *Br. J. Radiol.*, vol. 91, no. 1085, p. 20170318, Feb. 2018.

[8] Ö. Aanestad, R. Flink, M. Häggman, and B. J. Norlén, "Interference pattern in the urethral sphincter: A quantitative electromyographic study in patients before and after radical retropubic prostatectomy," *Scand. J. Urol. Nephrol.*, vol. 32, no. 6, pp. 378–382, 1998.

[9] B. Müller *et al.*, "Morphology of urethral tissues," *Dev. X-Ray Tomogr. VII*, vol. 7804, pp. 1–12, 2010.

[10] D. D. T. Maglinte and C. Bartram, "Dynamic imaging of posterior compartment pelvic floor dysfunction by evacuation proctography: Techniques, indications, results and limitations," *Eur. J. Radiol.*, vol. 61, no. 3, pp. 454–461, 2007.

[11] R. E. Stafford, R. Aljuraifani, F. Hug, and P. W. Hodges, "Application of shear-wave elastography to estimate the stiffness of the male striated urethral sphincter during voluntary contractions," *BJU Int.*, vol. 119, no. 4, pp. 619–625, 2017.

[12] H. Strasser, F. Frauscher, G. Helweg, K. Colleselli, A. Reissigl, and G. Bartsch, "Transurethral ultrasound: Evaluation of anatomy and function of the rhabdosphincter of the male urethra," *J. Urol.*, vol. 159, no. 1, pp. 100–105, 1998.

[13] R. P. Myers, D. R. Cahill, R. M. Devine, and B. F. King, "Anatomy of radical prostatectomy as defined by magnetic resonance imaging," *J. Urol.*, vol. 159, no. 6, pp. 2148–2158, 1998.

[14] J. M. Soares, P. Marques, V. Alves, and N. Sousa, "A hitchhiker's guide to diffusion tensor imaging," *Front. Neurosci.*, vol. 7, pp. 1–14, 2013.

[15] C. Jaimes, K. Darge, D. Khrichenko, R. H. Carson, and J. I. Berman, "Diffusion tensor imaging and tractography of the kidney in children: Feasibility and preliminary experience," *Pediatr. Radiol.*, vol. 44, no. 1, pp. 30–41, 2014.

[16] H. Wei *et al.*, "Assessment of cardiac motion effects on the fiber architecture of the human heart in vivo," *IEEE Trans. Med. Imaging*, vol. 32, no. 10, pp. 1928–1938, 2013.

[17] S. Sinha and U. Sinha, "In vivo diffusion tensor imaging of the human prostate," *Magn. Reson. Med.*, vol. 52, no. 3, pp. 530–537, 2004.

[18] N. Gholizadeh *et al.*, "Characterization of prostate cancer using diffusion tensor imaging: A new perspective," *Eur. J. Radiol.*, vol. 110, no. 2019, pp. 112–120, Jan. 2019.

[19] F. M. Zijta *et al.*, "Feasibility of diffusion tensor imaging (DTI) with fibre tractography of the normal female pelvic floor," *Eur. Radiol.*, vol. 21, no. 6, pp. 1243–1249, Jun. 2011.

[20] R. Seeley, T. Stephens, and P. Tate, *Anatomy and Physiology, Sixth Edition*. Boston, MA: McGraw Hill, 2003.

[21] J. C. Weinreb *et al.*, "PI-RADS Prostate Imaging – Reporting and Data System: 2015, Version

2," *Eur. Urol.*, vol. 69, no. 1, pp. 16–40, 2016.
[22] J. E. McNeal, "The Zonal Anatomy of the Prostate," *Prostate*, vol. 2, no. 1, pp. 35–49, 1981.
[23] T. Barrett, B. Turkbey, and P. L. Choyke, "PI-RADS version 2: what you need to know," *Clin. Radiol.*, vol. 70, no. 11, pp. 1165–1176, 2015.
[24] M. M. Koraitim, "The Male Urethral Sphincter Complex Revisited: An Anatomical Concept and its Physiological Correlate," *J. Urol.*, vol. 179, no. 5, pp. 1683–1689, May 2008.
[25] G. Murakami, F. Nakajima, T. J. Sato, M. H. Tsugane, K. Taguchi, and T. Tsukamoto, "Individual Variations in Aging of the Male Urethral Rhabdosphincter in Japanese," *Clin. Anat.*, vol. 15, no. October 2001, pp. 241–252, 2002.
[26] A. Thorpe and D. Neal, "Benign prostatic hyperplasia," *Lancet*, vol. 361, no. 9366, pp. 1359–1367, 2003.
[27] C. H. Pernar, E. M. Ebot, K. M. Wilson, and L. A. Mucci, "The Epidemiology of Prostate Cancer," *Cold Spring Harb. Perspect. Med.*, vol. 23, no. 4, pp. 1–18, Jan. 2018.
[28] J. Li, J. A. Djenaba, A. Soman, S. H. Rim, and V. A. Master, "Recent Trends in Prostate Cancer Incidence by Age, Cancer Stage, and Grade, the United States, 2001–2007," *Prostate Cancer*, vol. 2012, pp. 1–8, 2012.
[29] R. A. Castillejos-Molina and F. B. Gabilondo-Navarro, "Prostate cancer," *Salud Publica Mex.*, vol. 58, no. 2, pp. 279–284, 2016.
[30] M. J. Barry and J. H. Hayes, "Evaluating an Elevated Screening PSA Test," *JAMA*, vol. 314, no. 19, p. 2073, Nov. 2015.
[31] J. E. McNeal, E. A. Redwine, F. S. Freiha, and T. A. Stamey, "Zonal Distribution of Prostatic Adenocarcinoma," *Am. J. Surg. Pathol.*, vol. 12, no. 12, pp. 897–906, 1988.
[32] R. van Loenhout, F. Zijta, R. Smithuis, and I. Schoots, "Prostate Cancer - PI-RADS v2," *Radiology Department of the Haaglanden MC, Alrijne Hospital and Erasmus MC, the Netherlands*. [Online]. Available: http://www.radiologyassistant.nl/en/p59987056acbb4/prostate-cancer-pi-rads-v2.html#in59987056c4e34.
[33] P. Mandel *et al.*, "The effect of age on functional outcomes after radical prostatectomy," *Urol. Oncol. Semin. Orig. Investig.*, vol. 33, no. 5, pp. 203-e11, 2015.
[34] Y. J. Lee *et al.*, "Contemporary trends in radical prostatectomy and predictors of recovery of urinary continence in men aged over 70 years: comparisons between cohorts aged over 70 and less than 70 years," *Asian J. Androl.*, vol. 21, no. September 2018, pp. 1–7, 2019.
[35] P. C. Walsh, P. Marschke, D. Ricker, and A. L. Burnett, "Patient-reported urinary continence and sexual function after anatomic radical prostatectomy," *Urology*, vol. 55, no. 1, pp. 58–61, 2000.
[36] W. J. Ko, M. D. Truesdale, G. W. Hruby, J. Landman, and K. K. Badani, "Impacting factors for recovery of erectile function within 1 year following robotic-assisted laparoscopic radical prostatectomy," *J. Sex. Med.*, vol. 8, no. 6, pp. 1805–1812, 2011.
[37] N. Altilia *et al.*, "Elderly patients are not at higher risk of urinary incontinence after radical prostatectomy," *Off. J. Ital. Soc. Gerontol. Geriatr.*, vol. 168, no. 66, pp. 168–172, 2018.
[38] E. Sacco *et al.*, "Urinary incontinence after radical prostatectomy: incidence by definition , risk factors and temporal trend in a large series with a long-term follow-up," *BJU Int.*, vol. 97, no. 6, pp. 1234–1241, 2006.
[39] F. Montorsi *et al.*, "Best Practices in Robot-assisted Radical Prostatectomy: Recommendations of the Pasadena Consensus Panel," *Eur. Urol.*, vol. 62, no. 3, pp. 368–381, Sep. 2012.
[40] I. Seckiner, C. Yesilli, N. A. Mungan, A. Aykanat, and B. Akduman, "Correlations between the ICIQ-SF score and urodynamic findings," *Neurourol. Urodyn.*, vol. 26, no. 4, pp. 492–494, Jul. 2007.
[41] K. Hoyland, N. Vasdev, A. Abrof, and G. Boustead, "Post-radical prostatectomy incontinence: etiology and prevention.," *Rev. Urol.*, vol. 16, no. 4, pp. 181–8, 2014.
[42] R. Sosnowski *et al.*, "Urinary incontinence after radical prostatectomy - experience of the last 100 cases," *Cent. Eur. J. Urol.*, vol. 64, no. 4, pp. 213–217, 2011.
[43] G. Gautam, B. Rocco, V. R. Patel, and K. C. Zorn, "Posterior rhabdosphincter reconstruction during robot-assisted radical prostatectomy: Critical analysis of techniques and outcomes," *Urology*, vol. 76, no. 3, pp. 734–741, 2010.

[44] A. Galfano, A. Ascione, S. Grimaldi, G. Petralia, E. Strada, and A. M. Bocciardi, “A new anatomic approach for robot-assisted laparoscopic prostatectomy: A feasibility study for completely intrafascial surgery,” *Eur. Urol.*, vol. 58, no. 3, pp. 457–461, 2010.
[45] A. Galfano *et al.*, “Beyond the learning curve of the Retzius-sparing approach for robot-assisted laparoscopic radical prostatectomy: Oncologic and functional results of the first 200 patients with ≥1 year of follow-up,” *Eur. Urol.*, vol. 64, no. 6, pp. 974–980, 2013.
[46] A. Einstein, *Investigations on the theory of the Brownian movement*. 1956.
[47] P. Mukherjee, J. I. Berman, S. W. Chung, C. P. Hess, and R. G. Henry, “Diffusion Tensor MR Imaging and Fiber Tractography: Theoretic Underpinnings,” *Am. J. Neuroradiol.*, vol. 29, no. 4, pp. 632–641, Apr. 2008.
[48] D. Le Bihan, “Looking into the functional architecture of the brain with diffusion MRI,” *Int. Congr. Ser.*, vol. 1290, pp. 1–24, Jun. 2006.
[49] S. Mori and J. Zhang, “Principles of Diffusion Tensor Imaging and Its Applications to Basic Neuroscience Research,” *Neuron*, vol. 51, no. 5, pp. 527–539, Sep. 2006.
[50] T. A. G. M. Huisman, “Diffusion-weighted and diffusion tensor imaging of the brain, made easy,” *Cancer Imaging*, vol. 10, no. 1A, pp. 163–171, 2010.
[51] E. O. Stejskal and J. E. Tanner, “Spin diffusion measurements: Spin echoes in the presence of a time-dependent field gradient,” *J. Chem. Phys.*, vol. 42, no. 1, pp. 288–292, 1965.
[52] C.-F. Westin, S. E. Maier, H. Mamata, A. Nabavi, F. A. Jolesz, and R. Kikinis, “Processing and visualization for diffusion tensor MRI,” *Med. Image Anal.*, vol. 6, no. 2, pp. 93–108, Jun. 2002.
[53] L. J. O’Donnell and C. F. Westin, “An introduction to diffusion tensor image analysis,” *Neurosurg. Clin. N. Am.*, vol. 22, no. 2, pp. 185–196, 2011.
[54] D. Le Bihan, “Molecular diffusion nuclear magnetic resonance imaging,” *Magn Reson Q.*, vol. 7, no. 1, pp. 1–30, 1991.
[55] W. Van Hecke, L. Emsell, and S. Sunaert, *Diffusion Tensor Imaging: A Practical Handbook*. 2016.
[56] D. Tromp, “The diffusion tensor, and its relation to FA, MD, AD and RD,” *The Winnower*. pp. 1–10, 2015.
[57] P. J. Basser and C. Pierpaoli, “Microstructural and Physiological Features of Tissues Elucidated by Quantitative-Diffusion-Tensor MRI,” *J. Magn. Reson. Ser. B*, vol. 111, no. 3, pp. 209–219, Jun. 1996.
[58] S. Pajevic and C. Pierpaoli, “Color schemes to represent the orientation of anisotropic tissues from diffusion tensor data: Application to White Matter Fiber Tract Mapping in the Human Brain,” *Magn. Reson. Med.*, vol. 42, no. 3, pp. 526–540, 1999.
[59] D. K. Jones, T. R. Knösche, and R. Turner, “White matter integrity, fiber count, and other fallacies: The do’s and don’ts of diffusion MRI,” *Neuroimage*, vol. 73, pp. 239–254, Jun. 2013.
[60] P. J. Basser, J. Mattiello, and D. LeBihan, “MR diffusion tensor spectroscopy and imaging,” *Biophys. J.*, vol. 66, no. 1, pp. 259–267, 1994.
[61] P. G. P. Nucifora, X. Wu, E. R. Melhem, R. E. Gur, R. C. Gur, and R. Verma, “Automated Diffusion Tensor Tractography: implementation and comparison to user-driven tractography,” *Acad. Radiol.*, vol. 19, no. 5, pp. 622–629, May 2012.
[62] S. Mori, B. J. Crain, V. P. Chacko, and P. C. van Zijl, “Three-dimensional tracking of axonal projections in the brain by magnetic resonance imaging.,” *Ann. Neurol.*, vol. 45, no. 2, pp. 265–9, Feb. 1999.
[63] M. A. Côté, G. Girard, A. Boré, E. Garyfallidis, J. C. Houde, and M. Descoteaux, “Tractometer: Towards validation of tractography pipelines,” *Med. Image Anal.*, vol. 17, no. 7, pp. 844–857, 2013.
[64] N. Rodrigues, K. Mithani, Y. Meng, N. Lipsman, and C. Hamani, “The Emerging Role of Tractography in Deep Brain Stimulation: Basic Principles and Current Applications,” *Brain Sci.*, vol. 8, no. 2, p. 23, Jan. 2018.
[65] T. JD, C. F, and C. A, “MRtrix: diffusion tractography in crossing fibre regions,” *Int. J. Imaging Syst. Technol.*, 2012.
[66] G. E *et al.*, “DIPY, a library for the analysis of diffusion MRI data.,” *Front. Neuroinform.*, vol. 8, no. 8, 2014.
[67] K. H. Maier-Hein *et al.*, “The challenge of mapping the human connectome based on diffusion

tractography," *Nat. Commun.*, vol. 8, no. 1, p. 1349, Dec. 2017.
[68] E. Meintjes, P. A. Taylor, A. Alhamud, A. van der Kouwe, M. G. Saleh, and B. Laughton, "Assessing the performance of different DTI motion correction strategies in the presence of EPI distortion correction," *Hum Brain Mapp*, vol. 37, no. 12, pp. 4405–4424, 2016.
[69] "EPI distortion correction: echo spacing and bandwidth," *Brain Innovation*, 2018. [Online]. Available: https://support.brainvoyager.com/brainvoyager/functional-analysis-preparation/29-pre-processing/78-epi-distortion-correction-echo-spacing-and-bandwidth.
[70] S. M. Smith *et al.*, "Advances in functional and structural MR image analysis and implementation as FSL," *Neuroimage*, vol. 23, no. SUPPL. 1, pp. S208–S219, Jan. 2004.
[71] J. L. R. Andersson and S. N. Sotiropoulos, "An integrated approach to correction for off-resonance effects and subject movement in diffusion MR imaging," *Neuroimage*, vol. 125, pp. 1063–1078, Jan. 2016.
[72] J. L. R. Andersson, S. Skare, and J. Ashburner, "How to correct susceptibility distortions in spin-echo echo-planar images: application to diffusion tensor imaging," *Neuroimage*, vol. 20, no. 2, pp. 870–888, Oct. 2003.
[73] D. Le Bihan and E. Breton, "Imagerie de diffusion in vivo par resonance magnetique nucleaire," *Comptes Rendus des Seances l'Academie des Sci.*, vol. 301, no. 15, pp. 1109–1112, 1985.
[74] L. T. Westlye *et al.*, "Life-Span Changes of the Human Brain White Matter: Diffusion Tensor Imaging (DTI) and Volumetry," *Cereb. Cortex*, vol. 20, no. 9, pp. 2055–2068, Sep. 2010.
[75] A. N. Voineskos *et al.*, "Age-related decline in white matter tract integrity and cognitive performance: A DTI tractography and structural equation modeling study," *Neurobiol. Aging*, vol. 33, no. 1, pp. 21–34, Jan. 2012.
[76] D. C. Van Essen *et al.*, "The Human Connectome Project: A data acquisition perspective," *Neuroimage*, vol. 62, no. 4, pp. 2222–2231, Oct. 2012.
[77] J. P. Owen *et al.*, "Aberrant White Matter Microstructure in Children with 16p11.2 Deletions," *J. Neurosci.*, vol. 34, no. 18, pp. 6214–6223, Apr. 2014.
[78] W. Van Hecke *et al.*, "A diffusion tensor imaging group study of the spinal cord in multiple sclerosis patients with and without T2 spinal cord lesions," *J. Magn. Reson. Imaging*, vol. 30, no. 1, pp. 25–34, 2009.
[79] A. Vedantam, M. B. Jirjis, B. D. Schmit, M. C. Wang, J. L. Ulmer, and S. N. Kurpad, "Diffusion tensor imaging of the spinal cord: Insights from animal and human studies," *Neurosurgery*, vol. 74, no. 1, pp. 1–8, 2014.
[80] Y. Zhou, P. A. Narayana, M. Kumaravel, P. Athar, V. S. Patel, and K. A. Sheikh, "High resolution diffusion tensor imaging of human nerves in forearm," *J. Magn. Reson. Imaging*, vol. 39, no. 6, pp. 1374–1383, 2014.
[81] C. Khalil, J. F. Budzik, E. Kermarrec, V. Balbi, V. Le Thuc, and A. Cotten, "Tractography of peripheral nerves and skeletal muscles," *Eur. J. Radiol.*, vol. 76, no. 3, pp. 391–397, 2010.
[82] E. Furman-Haran *et al.*, "Advantages and drawbacks of breast DTI," *Eur. J. Radiol.*, vol. 81, no. 1, pp. S45–S47, Sep. 2012.
[83] A. Tagliafico *et al.*, "Diffusion tensor magnetic resonance imaging of the normal breast: reproducibility of DTI-derived fractional anisotropy and apparent diffusion coefficient at 3.0 T," *Radiol. Med.*, vol. 117, no. 6, pp. 992–1003, Sep. 2012.
[84] M. Froeling, A. J. Nederveen, K. Nicolay, and G. J. Strijkers, "DTI of human skeletal muscle: The effects of diffusion encoding parameters, signal-to-noise ratio and T2 on tensor indices and fiber tracts," *NMR Biomed.*, vol. 26, no. 11, pp. 1339–1352, 2013.
[85] U. Sinha, R. Csapo, V. Malis, Y. Xue, and S. Sinha, "Age-related differences in diffusion tensor indices and fiber architecture in the medial and lateral gastrocnemius," *J. Magn. Reson. Imaging*, vol. 41, no. 4, pp. 941–953, 2015.
[86] Y.-T. Wang, Y.-C. Li, W.-F. Kong, L.-L. Yin, and H. Pu, "Diffusion tensor imaging beyond brains: Applications in abdominal and pelvic organs," *World J. Meta-Analysis*, vol. 5, no. 3, p. 71, 2017.
[87] R. Girometti, M. Maieron, G. Lissandrello, M. Bazzocchi, and C. Zuiani, "Test–retest reliability of diffusion tensor imaging of the liver at 3.0 T," *Radiol. Med.*, vol. 120, no. 6, pp. 489–497, Jun. 2015.
[88] X. Li *et al.*, "Preliminary Study of MR Diffusion Tensor Imaging of Pancreas for the Diagnosis

of Acute Pancreatitis," *PLoS One*, vol. 11, no. 9, p. e0160115, Sep. 2016.
[89] M. Notohamiprodjo *et al.*, "Diffusion Tensor Imaging (DTI) of the Kidney at 3 Tesla–Feasibility, Protocol Evaluation and Comparison to 1.5 Tesla," *Invest. Radiol.*, vol. 45, no. 5, pp. 245–254, May 2010.
[90] F. Fiocchi *et al.*, "In vivo 3T MR diffusion tensor imaging for detection of the fibre architecture of the human uterus: A feasibility and quantitative study," *Br. J. Radiol.*, vol. 85, no. 1019, pp. 1009–1017, 2012.
[91] C. K. Kim, S. M. Jang, and B. K. Park, "Diffusion tensor imaging of normal prostate at 3 T: effect of number of diffusion-encoding directions on quantitation and image quality," *Br. J. Radiol.*, vol. 85, no. 1015, pp. e279–e283, Jul. 2012.
[92] B. Gürses *et al.*, "Diffusion tensor imaging of the normal prostate at 3 Tesla," *Eur. Radiol.*, vol. 18, no. 4, pp. 716–721, 2008.
[93] D. Falkner, "BMC 'Research in progress' photo competition 2018: winning images," *BMC*, 2018. [Online]. Available: http://blogs.biomedcentral.com/bmcblog/2018/12/14/bmc-research-in-progress-photo-competition-2018-winning-images/.
[94] B. Issa, "In vivo measurement of the apparent diffusion coefficient in normal and malignant prostatic tissues using echo-planar imaging," *J. Magn. Reson. Imaging*, vol. 16, no. 2, pp. 196–200, 2002.
[95] P. Gibbs, D. J. Tozer, G. P. Liney, and L. W. Turnbull, "Comparison of quantitative T2 mapping and diffusion-weighted imaging in the normal and pathologic prostate," *Magn. Reson. Med.*, vol. 46, no. 6, pp. 1054–1058, 2001.
[96] P. Gibbs, M. D. Pickles, and L. W. Turnbull, "Diffusion imaging of the prostate at 3.0 Tesla," *Invest. Radiol.*, vol. 41, no. 2, pp. 185–188, 2006.
[97] G. Barrio-Arranz, R. de Luis-García, A. Tristán-Vega, M. Martín-Fernández, and S. Aja-Fernández, "Impact of MR Acquisition Parameters on DTI Scalar Indexes: A Tractography Based Approach," *PLoS One*, vol. 10, no. 10, p. e0137905, Oct. 2015.
[98] V. Colangelo *et al.*, "Diffusion tensor magnetic resonance imaging of prostate cancer," *Invest. Radiol.*, vol. 42, no. 6, pp. 412–419, 2007.
[99] C. Li *et al.*, "Diffusion tensor imaging of prostate at 3.0 Tesla," *Acta radiol.*, vol. 52, no. 7, pp. 813–817, Sep. 2011.
[100] W. Tian *et al.*, "Correlation of diffusion tensor imaging parameters and Gleason scores of prostate cancer," *Exp. Ther. Med.*, vol. 15, no. 1, pp. 351–356, Oct. 2017.
[101] J. Zhang, W. Z. Tian, C. H. Hu, T. L. Niu, X. L. Wang, and X. Y. Chen, "Age-related changes of normal prostate: Evaluation by MR diffusion tensor imaging," *Int. J. Clin. Exp. Med.*, vol. 8, no. 7, pp. 11220–11224, 2015.
[102] C. Shi *et al.*, "Ultrahigh b-values MRI in normal human prostate: Initial research on reproducibility and age-related differences," *J. Magn. Reson. Imaging*, vol. 46, no. 3, pp. 801–812, 2017.
[103] S. Y. Park, C. K. Kim, B. K. Park, S. Y. Ha, G. Y. Kwon, and B. Kim, "Diffusion-Tensor MRI at 3 T: Differentiation of Central Gland Prostate Cancer From Benign Prostatic Hyperplasia," *Am. J. Roentgenol.*, vol. 202, no. 3, pp. W254–W262, Mar. 2014.
[104] D. S. Finley *et al.*, "Diffusion tensor magnetic resonance tractography of the prostate: Feasibility for mapping periprostatic fibers," *Urology*, vol. 80, no. 1, pp. 219–223, 2012.
[105] V. Panebianco *et al.*, "In vivo 3D neuroanatomical evaluation of periprostatic nerve plexus with 3T-MR diffusion tensor imaging," *Eur. J. Radiol.*, vol. 82, no. 10, pp. 1677–1682, 2013.
[106] K. Kitajima, S. Takahashi, Y. Ueno, H. Miyake, M. Fujisawa, and K. Sugimura, "Visualization of periprostatic nerve fibers before and after radical prostatectomy using diffusion tensor magnetic resonance imaging with tractography," *Clin. Imaging*, vol. 38, no. 3, pp. 302–306, 2014.
[107] S. Siracusano *et al.*, "Visualization of peri-prostatic neurovascular fibers before and after radical prostatectomy by means of diffusion tensor imaging (DTI) with clinical correlations: preliminary report," *J. Robot. Surg.*, no. Jul 6, pp. 1–7, Jul. 2019.
[108] A. D. J. Baur *et al.*, "Influence of fractional anisotropy thresholds on diffusion tensor imaging tractography of the periprostatic neurovascular bundle and selected pelvic tissues: Do visualized tracts really represent nerves?," *Acta radiol.*, vol. 58, no. 4, pp. 472–480, 2017.

[109] W. Jomoto *et al.*, “Evaluation of local look diffusion tensor imaging for magnetic resonance tractography of the periprostatic neurovascular bundle,” *Radiol. Phys. Technol.*, vol. 11, no. 3, pp. 353–359, Sep. 2018.
[110] A. L. Burnett and J. L. Mostwin, “In situ anatomical study of the male urethral sphincteric complex: relevance to continence preservation following major pelvic surgery,” *J. Urol.*, vol. 160, no. 4, pp. 1301–1306, Oct. 1998.
[111] H. Strasser, M. Tiefenthaler, M. Steinlechner, I. Eder, G. Bartsch, and G. Konwalinka, “Age dependent apoptosis and loss of rhabdosphincter cells,” *J. Urol.*, vol. 164, no. November, pp. 1781–1785, 2000.
[112] A. Tienza, M. Hevia, A. Benito, J. I. Pascual, J. J. Zudaire, and J. E. Robles, “MRI factors to predict urinary incontinence after retropubic/laparoscopic radical prostatectomy,” *Int. Urol. Nephrol.*, vol. 47, no. 8, pp. 1343–1349, 2015.
[113] D. L. et al Mason, “Pydicom: An Open Source DICOM Library,” 2008. .
[114] “De-identification,” *Medical Physics Royal Surrey County Hospital*, 2011. [Online]. Available: https://medphys.royalsurrey.nhs.uk/omidb/about-prospects/de-identification/.
[115] B. C. Lowekamp, D. T. Chen, L. Ibáñez, and D. Blezek, “The Design of SimpleITK,” *Front. Neuroinform.*, vol. 7, pp. 1–14, 2013.
[116] RStudio Team, “RStudio: Integrated Development for R. RStudio,” *RStudio, Inc., Boston, MA*, 2015. [Online]. Available: http://www.rstudio.com/.
[117] W. Revelle, “psych: Procedures for Personality and Psychological Research,” *Northwestern University, Evanston, Illinois, USA*. 2008.
[118] C. K. Kim and B. K. Park, “Update of prostate magnetic resonance imaging at 3 T,” *J. Comput. Assist. Tomogr.*, vol. 32, no. 2, pp. 163–172, 2008.
[119] J. Wasserthal, P. Neher, and K. H. Maier-Hein, “TractSeg - Fast and accurate white matter tract segmentation,” *Neuroimage*, vol. 183, pp. 239–253, Aug. 2018.
[120] B. Chughtai *et al.*, “Benign prostatic hyperplasia,” *Nat. Rev. Dis. Prim.*, vol. 2, no. 1, p. 16031, Dec. 2016.

APPENDIX

Table A Mean and standard deviation (mean ± sd) values on the 14 histogram metrics for each of the DTI indices of the 95 male study subjects, for each analyzed structure of the urethral complex. Histogram metrics regarding diffusivity measures - AD, MD and RD – are expressed in 10^{-3} mm^2/s; Histogram metrics regarding FA are dimensionless.

		Proximal sphincter	Distal sphincter	Membranous urethra
FA	Standard deviation (sd)	0.0908 ± 0.0186	0.0870 ± 0.0196	0.0802 ± 0.0254
	Median	0.3525 ± 0.0404	0.3025 ± 0.0424	0.3252 ± 0.0494
	Trimmed mean	0.3553 ± 0.0399	0.3086 ± 0.0412	0.3290 ± 0.0475
	Median absolute deviation (mad)	0.0875 ± 0.0179	0.0804 ± 0.0195	0.0801 ± 0.0303
	Minimum	0.0903 ± 0.0295	0.1188 ± 0.0263	0.1438 ± 0.0352
	Maximum	0.8155 ± 0.1221	0.6859 ± 0.1123	0.6149 ± 0.1217
	Range	0.7252 ± 0.1372	0.5671 ± 0.1168	0.4711 ± 0.1191
	Skewness	0.4914 ± 0.3492	0.7618 ± 0.4527	0.3562 ± 0.4978
	Kurtosis	0.5346 ± 0.9719	0.9033 ± 1.7613	0.0106 ± 1.0735
	Standard error (se)	0.0001 ± 0.0001	0.0006 ± 0.0005	0.0004 ± 0.0007
	5th percentile (Q0.05)	0.2240 ± 0.0236	0.1968 ± 0.0280	0.2144 ± 0.0362
	25th percentile (Q0.25)	0.2956 ± 0.0322	0.2522 ± 0.0356	0.2729 ± 0.0420
	75th percentile (Q0.75)	0.4148 ± 0.0491	0.3652 ± 0.0500	0.3856 ± 0.0605
	95th percentile (Q0.95)	0.5211 ± 0.0736	0.4771 ± 0.0734	0.4735 ± 0.0868
AD	Standard deviation (sd)	0.3862 ± 0.1441	0.3764 ± 0.1473	0.2804 ± 0.1290
	Median	2.1496 ± 0.1623	2.0882 ± 0.2043	2.1221 ± 0.3793
	Trimmed mean	2.1596 ± 0.1664	2.1050 ± 0.2085	2.1260 ± 0.3757
	Median absolute deviation (mad)	0.3142 ± 0.0827	0.3274 ± 0.1277	0.2804 ± 0.1512
	Minimum	0.5012 ± 0.4862	0.9853 ± 0.4440	1.2981 ± 0.3534
	Maximum	4.4297 ± 0.9316	3.6830 ± 0.7929	2.9695 ± 0.6820
	Range	3.9286 ± 1.2136	2.6977 ± 0.9186	1.6714 ± 0.6791
	Skewness	0.5375 ± 0.7939	0.4250 ± 0.8026	0.0500 ± 0.5409
	Kurtosis	2.5848 ± 2.8041	1.3442 ± 2.2239	0.0615 ± 1.3894
	Standard error (se)	0.0005 ± 0.0005	0.0025 ± 0.0019	0.0014 ± 0.0033
	5th percentile (Q0.05)	1.6075 ± 0.2071	1.5822 ± 0.2234	1.6919 ± 0.2896
	25th percentile (Q0.25)	1.9416 ± 0.1562	1.8773 ± 0.1838	1.9293 ± 0.3100
	75th percentile (Q0.75)	2.3800 ± 0.2215	2.3304 ± 0.2655	2.3255 ± 0.4578
	95th percentile (Q0.95)	2.8338 ± 0.4139	2.8161 ± 0.5067	2.5952 ± 0.5641
MD	Standard deviation (sd)	0.3198 ± 0.1212	0.3125 ± 0.1190	0.2295 ± 0.0937
	Median	1.5685 ± 0.1479	1.5953 ± 0.1944	1.5739 ± 0.3080
	Trimmed mean	1.5796 ± 0.1530	1.6046 ± 0.1930	1.5738 ± 0.3080
	Median absolute deviation (mad)	0.2511 ± 0.0721	0.2740 ± 0.1068	0.2284 ± 0.1170
	Minimum	0.3332 ± 0.3407	0.6621 ± 0.3342	0.8890 ± 0.2976
	Maximum	3.4632 ± 0.6609	2.8690 ± 0.6722	2.2314 ± 0.4777

RD	Range	3.1300 ± 0.8488	2.2069 ± 0.7720	1.3424 ± 0.4782
	Skewness	0.6711 ± 0.7994	0.3311 ± 0.7493	-0.0528 ± 0.5785
	Kurtosis	2.8261 ± 2.6540	1.2507 ± 2.0875	0.0322 ± 1.4025
	Standard error (se)	0.0004 ± 0.0004	0.0021 ± 0.0016	0.0012 ± 0.0027
	5th percentile (Q0.05)	1.1352 ± 0.1852	1.1514 ± 0.2066	1.2064 ± 0.2697
	25th percentile (Q0.25)	1.4036 ± 0.1456	1.4149 ± 0.1774	1.4103 ± 0.2733
	75th percentile (Q0.75)	1.7590 ± 0.2069	1.7940 ± 0.2367	1.7369 ± 0.3593
	95th percentile (Q0.95)	2.1552 ± 0.3603	2.1790 ± 0.4094	1.9457 ± 0.4283
	Standard deviation (sd)	0.3137 ± 0.1070	0.3041 ± 0.1052	0.2305 ± 0.0812
	Median	1.2782 ± 0.1485	1.3485 ± 0.1908	1.2975 ± 0.2800
	Trimmed mean	1.2895 ± 0.1526	1.3539 ± 0.1902	1.2966 ± 0.2805
	Median absolute deviation (mad)	0.2575 ± 0.0713	0.2689 ± 0.0928	0.2281 ± 0.1008
	Minimum	0.2137 ± 0.2303	0.4509 ± 0.2635	0.6186 ± 0.2784
	Maximum	3.1345 ± 0.5802	2.5737 ± 0.6093	1.9713 ± 0.4141
	Range	2.9208 ± 0.7023	2.1228 ± 0.6817	1.3527 ± 0.4078
	Skewness	0.6714 ± 0.6797	0.2801 ± 0.6584	-0.0725 ± 0.5717
	Kurtosis	2.2595 ± 2.0937	1.0245 ± 1.7486	0.0170 ± 1.3078
	Standard error (se)	0.0004 ± 0.0004	0.0021 ± 0.0015	0.0012 ± 0.0026
	5th percentile (Q0.05)	0.8526 ± 0.1745	0.8959 ± 0.2017	0.9230 ± 0.2651
	25th percentile (Q0.25)	1.1100 ± 0.1466	1.1673 ± 0.1811	1.1331 ± 0.2645
	75th percentile (Q0.75)	1.4717 ± 0.2003	1.5396 ± 0.2234	1.4586 ± 0.3152
	95th percentile (Q0.95)	1.8600 ± 0.3283	1.8984 ± 0.3676	1.6692 ± 0.3668

Table B Analysis of variance (ANOVA) test result on the comparison of each DTI metric for the male urethral complex structures studied, between age and disease. Additionally, t-test results on the comparison of DTI metrics between cancer status groups. Non-parametric test results are highlighted in light blue, and statistically significant test p-values are color-coded, as shown by Figure 5.18.

COMPARISON OF EACH VARIABLE BY GROUP

Variable	For **94 subjects**		For **69 subjects**			
	AGE GROUP		**DISEASE GROUP**		**CANCER STATUS**	
	F value /chi-squared	**p-value**	**F value /chi-squared**	**p-value**	**t test/ W**	**p-value**
PROX_FA	0.712	0.547	1.032	0.362	1.121	0.269
PROX_FA_SD	0.344	0.794	0.141	0.869	521	0.817
PROX_FA_MEDIAN	1.021	0.387	1.648	0.200	1.501	0.141
PROX_FA_TRIMMED	0.816	0.488	1.216	0.303	1.213	0.232
PROX_FA_MAD	0.316	0.813	0.194	0.824	523	0.837
PROX_FA_MIN	6.591	0.086	0.126	0.939	556	0.845
PROX_FA_MAX	2.759	0.430	2.801	0.246	631	0.256
PROX_FA_RANGE	3.539	0.316	2.409	0.300	626	0.284
PROX_FA_SKEW	4.193	0.241	4.896	0.086	419	0.130
PROX_FA_KURTOSIS	2.567	0.463	0.679	0.712	554	0.866
PROX_FA_SE	0.828	0.843	0.956	0.620	485	0.495
PROX_FA_Q0.05	1.029	0.384	1.101	0.339	607	0.405
PROX_FA_Q0.25	0.872	0.459	1.533	0.224	1.391	0.171
PROX_FA_Q0.75	0.624	0.601	0.892	0.415	1.003	0.322
PROX_FA_Q0.95	0.497	0.685	0.191	0.826	0.537	0.595
PROX_AD	1.730	0.167	0.674	0.513	0.977	0.334
PROX_AD_SD	2.042	0.564	1.054	0.590	570	0.712
PROX_AD_MEDIAN	1.154	0.332	1.405	0.253	1.261	0.214
PROX_AD_TRIMMED	1.604	0.194	1.080	0.346	1.161	0.252
PROX_AD_MAD	3.494	0.322	0.724	0.489	-0.162	0.872
PROX_AD_MIN	4.010	0.260	3.005	0.223	470	0.381
PROX_AD_MAX	1.517	0.215	0.849	0.654	0.864	0.391
PROX_AD_RANGE	5.763	0.124	0.824	0.443	625	0.289
PROX_AD_SKEW	0.990	0.804	2.860	0.239	575	0.666
PROX_AD_KURTOSIS	3.458	0.326	1.254	0.534	625	0.289
PROX_AD_SE	0.254	0.968	1.297	0.523	478	0.441
PROX_AD_Q0.05	2.609	0.456	1.549	0.461	621	0.313
PROX_AD_Q0.25	0.571	0.636	1.178	0.314	1.314	0.197
PROX_AD_Q0.75	8.310	0.040	2.126	0.345	642	0.203
PROX_AD_Q0.95	6.231	0.101	0.750	0.687	605	0.419
PROX_MD	1.898	0.136	0.561	0.573	586	0.569
PROX_MD_SD	1.160	0.329	0.416	0.661	0.068	0.946
PROX_MD_MEDIAN	1.240	0.300	1.164	0.319	0.828	0.413
PROX_MD_TRIMMED	1.888	0.137	0.914	0.406	0.675	0.503
PROX_MD_MAD	2.251	0.088	4.891	0.087	557	0.837
PROX_MD_MIN	3.150	0.369	3.120	0.210	463	0.335
PROX_MD_MAX	1.904	0.135	0.291	0.748	0.757	0.452
PROX_MD_RANGE	1.635	0.187	1.721	0.423	622	0.307
PROX_MD_SKEW	0.683	0.565	3.424	0.038	-0.132	0.896
PROX_MD_KURTOSIS	7.631	0.054	1.728	0.421	608	0.398
PROX_MD_SE	0.104	0.991	1.542	0.462	493	0.561
PROX_MD_Q0.05	1.725	0.631	1.425	0.490	612	0.370
PROX_MD_Q0.25	0.485	0.693	0.483	0.619	621	0.313
PROX_MD_Q0.75	3.532	0.018	2.042	0.360	595	0.495

PROX_MD_Q0.95	4.595	0.204	0.890	0.641	596	0.487
PROX_RD	1.922	0.132	0.565	0.571	0.323	0.748
PROX_RD_SD	1.175	0.324	0.397	0.674	0.126	0.901
PROX_RD_MEDIAN	1.295	0.281	0.920	0.403	0.447	0.657
PROX_RD_TRIMMED	1.895	0.136	0.847	0.433	0.393	0.696
PROX_RD_MAD	2.335	0.079	3.979	0.137	565	0.759
PROX_RD_MIN	2.608	0.456	3.367	0.186	455	0.287
PROX_RD_MAX	1.855	0.143	0.344	0.710	0.855	0.396
PROX_RD_RANGE	5.347	0.148	0.475	0.624	632	0.251
PROX_RD_SKEW	0.854	0.468	3.777	0.028	-0.275	0.785
PROX_RD_KURTOSIS	8.177	0.042	2.383	0.304	607	0.405
PROX_RD_SE	0.128	0.988	1.355	0.508	504	0.657
PROX_RD_Q0.05	1.685	0.640	0.871	0.647	598	0.472
PROX_RD_Q0.25	0.598	0.301	0.374	0.689	604	0.426
PROX_RD_Q0.75	9.299	0.026	1.817	0.403	574	0.673
PROX_RD_Q0.95	4.625	0.201	1.173	0.556	588	0.552
DIST_FA	0.902	0.443	1.615	0.446	-1.308	0.199
DIST_FA_SD	1.434	0.238	0.095	0.909	0.397	0.693
DIST_FA_MEDIAN	0.419	0.740	2.099	0.350	-1.392	0.172
DIST_FA_TRIMMED	0.741	0.530	1.685	0.431	-1.374	0.178
DIST_FA_MAD	1.103	0.352	0.761	0.684	586	0.569
DIST_FA_MIN	2.316	0.509	0.180	0.835	-0.483	0.631
DIST_FA_MAX	1.145	0.766	0.867	0.648	608	0.398
DIST_FA_RANGE	1.242	0.743	0.752	0.687	603	0.434
DIST_FA_SKEW	0.183	0.980	1.204	0.306	582	0.604
DIST_FA_KURTOSIS	0.247	0.970	0.210	0.900	575	0.666
DIST_FA_SE	1.896	0.594	2.282	0.110	-0.195	0.846
DIST_FA_Q0.05	2.004	0.572	5.918	0.052	347	0.015
DIST_FA_Q0.25	0.306	0.821	3.765	0.152	388	0.056
DIST_FA_Q0.75	1.130	0.341	0.336	0.845	494	0.569
DIST_FA_Q0.95	1.636	0.187	0.040	0.980	-0.533	0.597
DIST_AD	3.704	0.295	1.425	0.491	630	0.262
DIST_AD_SD	1.486	0.685	0.132	0.936	526	0.866
DIST_AD_MEDIAN	7.606	0.055	1.005	0.605	615	0.351
DIST_AD_TRIMMED	5.490	0.139	1.297	0.523	625	0.289
DIST_AD_MAD	1.699	0.637	0.649	0.723	547	0.935
DIST_AD_MIN	0.306	0.959	0.117	0.890	556	0.846
DIST_AD_MAX	3.046	0.033	0.496	0.780	595	0.495
DIST_AD_RANGE	1.442	0.236	0.126	0.939	556	0.846
DIST_AD_SKEW	2.139	0.101	0.580	0.748	599	0.464
DIST_AD_KURTOSIS	2.370	0.499	0.881	0.644	585	0.578
DIST_AD_SE	0.136	0.939	2.215	0.117	-0.478	0.635
DIST_AD_Q0.05	6.036	0.110	2.136	0.344	654	0.154
DIST_AD_Q0.25	10.238	0.017	0.788	0.674	610	0.384
DIST_AD_Q0.75	2.641	0.450	2.365	0.307	641	0.207
DIST_AD_Q0.95	1.439	0.696	0.890	0.641	596	0.487
DIST_MD	3.904	0.272	1.403	0.496	634	0.241
DIST_MD_SD	1.176	0.759	1.017	0.602	460	0.319
DIST_MD_MEDIAN	6.558	0.087	0.966	0.617	618	0.331
DIST_MD_TRIMMED	4.595	0.204	1.257	0.533	629	0.267
DIST_MD_MAD	0.807	0.848	0.462	0.794	495	0.578
DIST_MD_MIN	0.782	0.854	0.034	0.967	0.174	0.863
DIST_MD_MAX	11.943	0.008	0.665	0.717	586	0.569
DIST_MD_RANGE	3.175	0.028	0.014	0.986	0.034	0.973
DIST_MD_SKEW	12.067	0.007	0.379	0.827	518	0.788

DIST_MD_KURTOSIS	8.155	0.043	0.566	0.753	581	0.612
DIST_MD_SE	0.210	0.889	2.176	0.122	-0.561	0.578
DIST_MD_Q0.05	4.317	0.229	1.997	0.368	652	0.161
DIST_MD_Q0.25	2.065	0.110	0.259	0.773	627	0.278
DIST_MD_Q0.75	2.660	0.447	1.367	0.505	625	0.289
DIST_MD_Q0.95	2.775	0.428	0.626	0.731	574	0.675
DIST_RD	3.278	0.351	1.238	0.538	628	0.272
DIST_RD_SD	0.871	0.459	0.606	0.739	479	0.449
DIST_RD_MEDIAN	5.636	0.131	0.805	0.669	611	0.377
DIST_RD_TRIMMED	3.781	0.286	1.154	0.562	625	0.289
DIST_RD_MAD	0.401	0.753	0.067	0.967	520	0.807
DIST_RD_MIN	0.662	0.882	0.024	0.988	549	0.915
DIST_RD_MAX	5.342	0.002	0.386	0.824	578	0.639
DIST_RD_RANGE	3.638	0.016	0.003	0.997	0	0.936
DIST_RD_SKEW	3.473	0.019	0.038	0.963	0	0.780
DIST_RD_KURTOSIS	8.761	0.033	0.666	0.717	555	0.856
DIST_RD_SE	0.233	0.873	2.113	0.129	0	0.653
DIST_RD_Q0.05	1.423	0.241	0.566	0.570	1	0.296
DIST_RD_Q0.25	1.547	0.208	0.226	0.799	604	0.426
DIST_RD_Q0.75	2.440	0.254	0.922	0.631	615	0.351
DIST_RD_Q0.95	3.231	0.486	0.985	0.611	600	0.456
MU_FA	0.109	0.955	0.033	0.968	-0.253	0.801
MU_FA_SD	0.186	0.906	0.473	0.625	-0.405	0.687
MU_FA_MEDIAN	0.184	0.907	0.026	0.974	0.044	0.965
MU_FA_TRIMMED	0.127	0.944	0.023	0.977	-0.211	0.834
MU_FA_MAD	0.002	1.000	0.149	0.862	-0.573	0.569
MU_FA_MIN	1.615	0.656	0.571	0.751	485	0.495
MU_FA_MAX	1.255	0.740	0.503	0.607	0.221	0.826
MU_FA_RANGE	0.507	0.917	0.732	0.485	0.576	0.567
MU_FA_SKEW	2.915	0.405	0.212	0.810	-0.019	0.985
MU_FA_KURTOSIS	0.255	0.968	2.513	0.285	664	0.120
MU_FA_SE	2.668	0.446	1.331	0.514	449	0.256
MU_FA_Q0.05	0.107	0.956	0.322	0.726	0.140	0.889
MU_FA_Q0.25	0.136	0.938	0.055	0.947	0.320	0.751
MU_FA_Q0.75	0.115	0.951	0.207	0.813	-0.618	0.539
MU_FA_Q0.95	0.212	0.888	0.233	0.793	-0.407	0.686
MU_AD	3.412	0.332	1.784	0.410	639	0.216
MU_AD_SD	4.526	0.005	1.838	0.167	1.639	0.109
MU_AD_MEDIAN	2.540	0.468	1.176	0.556	623	0.301
MU_AD_TRIMMED	3.097	0.377	1.539	0.463	634	0.241
MU_AD_MAD	2.375	0.075	0.683	0.509	0.979	0.333
MU_AD_MIN	1.006	0.800	0.384	0.825	583	0.595
MU_AD_MAX	5.942	0.114	3.647	0.161	671	0.100
MU_AD_RANGE	1.869	0.140	1.727	0.186	1.799	0.078
MU_AD_SKEW	0.925	0.819	0.685	0.710	597	0.479
MU_AD_KURTOSIS	2.178	0.536	0.260	0.878	578	0.639
MU_AD_SE	7.349	0.062	0.824	0.662	523	0.837
MU_AD_Q0.05	0.569	0.903	0.936	0.626	616	0.344
MU_AD_Q0.25	1.127	0.771	1.211	0.546	622	0.307
MU_AD_Q0.75	4.667	0.198	1.854	0.396	648	0.177
MU_AD_Q0.95	6.056	0.109	3.179	0.204	672	0.098
MU_MD	3.128	0.372	1.963	0.375	633	0.246
MU_MD_SD	3.803	0.013	0.403	0.670	0.803	0.427
MU_MD_MEDIAN	2.376	0.498	1.398	0.497	623	0.301
MU_MD_TRIMMED	2.751	0.432	1.628	0.443	625	0.289

MU_MD_MAD	3.375	0.022	0.192	0.826	0.215	0.831
MU_MD_MIN	0.678	0.878	0.322	0.726	579	0.630
MU_MD_MAX	4.610	0.203	1.433	0.246	1.601	0.116
MU_MD_RANGE	1.148	0.334	0.901	0.411	1.321	0.193
MU_MD_SKEW	0.855	0.836	0.972	0.384	0.793	0.432
MU_MD_KURTOSIS	2.488	0.477	1.619	0.445	638	0.221
MU_MD_SE	6.371	0.095	0.727	0.695	499	0.612
MU_MD_Q0.05	0.156	0.926	0.635	0.533	0.876	0.385
MU_MD_Q0.25	1.528	0.676	1.299	0.522	619	0.325
MU_MD_Q0.75	3.803	0.284	0.678	0.712	598	0.472
MU_MD_Q0.95	7.591	0.055	1.827	0.401	638	0.221
MU_RD	0.161	0.984	0.511	0.774	489	0.527
MU_RD_SD	2.228	0.090	0.073	0.930	564	0.769
MU_RD_MEDIAN	2.285	0.515	0.720	0.698	597	0.479
MU_RD_TRIMMED	2.500	0.475	1.002	0.606	603	0.434
MU_RD_MAD	2.430	0.070	0.056	0.946	0.089	0.929
MU_RD_MIN	0.354	0.786	0.630	0.536	0.442	0.661
MU_RD_MAX	0.831	0.480	1.538	0.222	1.739	0.089
MU_RD_RANGE	0.611	0.609	0.890	0.416	1.161	0.252
MU_RD_SKEW	2.159	0.540	1.050	0.356	0.813	0.420
MU_RD_KURTOSIS	3.918	0.270	2.018	0.365	647	0.181
MU_RD_SE	5.493	0.139	0.575	0.750	491	0.544
MU_RD_Q0.05	0.249	0.862	0.811	0.449	0.968	0.338
MU_RD_Q0.25	1.751	0.626	1.511	0.470	626	0.284
MU_RD_Q0.75	3.150	0.626	0.512	0.774	565	0.759
MU_RD_Q0.95	5.809	0.369	1.095	0.578	613	0.364
PROX_LEN	1.203	0.313	3.415	0.039	2.582	0.013
PROX_DEN	0.050	0.997	3.501	0.174	497	0.595
DIST_LEN	4.281	0.233	2.314	0.315	564	0.769
DIST_DEN	0.346	0.792	4.051	0.021	0.311	0.758
MU_LEN	2.932	0.402	1.306	0.521	629	0.267
MU_DEN	1.454	0.693	1.227	0.541	567	0.740